NEW MEXICO BUREAU OF GEOLOGY AND MINERAL RESOURCES

Hydrogeology and Geochemistry of the Animas River Alluvial Aquifer, San Juan County, New Mexico: Assessing Groundwater Recharge, Flow Paths, and Solute Sources

B. Talon Newton
Ethan Mamer

Open-File Report 612
September 2020

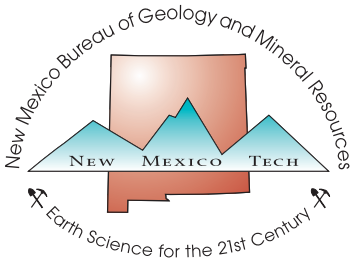

New Mexico Bureau of Geology and Mineral Resources

A Research Division of New Mexico Institute of Mining and Technology

Socorro, NM 87801
(575) 835 5490
www.geoinfo.nmt.edu

Hydrogeology and Geochemistry of the Animas River Alluvial Aquifer, San Juan County, New Mexico: Assessing Groundwater Recharge, Flow Paths, and Solute Sources

B. Talon Newton
Ethan Mamer

Open-File Report 612
September 2020

New Mexico Bureau of Geology and Mineral Resources

PROJECT FUNDING

Funding for this project is provided by the New Mexico Environment Department under
MOA 18 667 1210 0006, Amendment 1.

ACKNOWLEDGWMENTS

This project was successful only because of the generosity and gracious cooperation of well and land owners along the Animas Valley who allow us to access their wells to collect these essential data. As the authors, we thank our colleagues and collaborators at the New Mexico Environment Department including Dennis McQuillan and Kristine Yurdin for feedback and support on this project. We wish to acknowledge staff of the New Mexico Bureau of Geology and Mineral Resources who helped on this project including Scott Christenson (field data collection), Trevor Kludt (field data collection), Cathryn Pokorny (data management), Stacy Timmons (General guidance), Brigitte Felix and Belinda Harrison (mapping and graphic support), and Bonnie Frey and Dustin Baca (chemistry lab analysis). Finally, we thank Scott Christenson (NMBGMR), Laila Sturgis (NMBGMR), Kristine Yurdin (NMED), Dr. Laura Crossey (UNM), and Dr. Johanna Blake (USGS) for their reviews and constructive feedback that greatly improved this report.

Cover: Near Cedar Hill, NM, looking towards the Animas River from an agricultural field, where the water level of the river was surveyed to compare to the water table elevation in the area.

CONTENTS

Figures

1. The study focused on the reach of the Animas River, from the Colorado–New Mexico state line to Farmington 5
2. Geologic cross-section of the San Juan Basin 8
3. Geologic map and cross-section along the Animas River 9
4. Average daily discharge for 2018/2019, and historic average daily discharge between 2003 and 2019 10
5. Seasonal fluctuations in wells completed in the shallow alluvial aquifer in the Animas Valley observed in 2016 10
6. Examples of Irrigation controlled well and river stage controlled well 11
7. Wells that were sampled between January 2016 and June 2017 12
8. Piper diagram showing the relative major ion concentrations for river water and groundwater 13
9. Conceptual model showing the upwelling of regional high-sulfate groundwater into the shallow aquifer 14
10. Continuous water level and specific conductance data in four wells and an irrigation ditch 14

Tables

EXECUTIVE SUMMARY

This report describes and discusses data and results for a geochemical study of groundwater in the Animas River Valley in New Mexico, which was conducted by the New Mexico Bureau of Geology and Mineral Resources (NMBGMR). This study is a continuation of previous work done by NMBGMR (Newton et al., 2017). After the Gold King Mine (GKM) released metal and sludge-laden water into Cement Creek and the Animas River on August 5, 2015, the NMBGMR, along with other federal and state agencies and tribes, responded with a collaborative research effort to assess potential environmental and economic impacts to New Mexico communities along the Animas River. Collaborative agencies included the U.S. Environmental Protection Agency (EPA), the New Mexico Environment Department (NMED), the Arizona Department of Environmental Quality, the Colorado Department of Public Health and the Environment, Navajo Nation EPA, the Southern Ute Indian Tribe, the Utah Department of Environmental Quality, the Ute Mountain Ute Tribe, and the United States Geological Survey (USGS). Newton et al., (2017) using groundwater level and water chemistry data collected between January 2016 and June 2017, characterized the local hydrogeology and looked for evidence of potential impacts from the GKM spill on local groundwater quality. While Newton et al., (2017) found no evidence of groundwater contamination that was directly associated with the GKM spill, a subsequent study phase was recommended to continue groundwater quality monitoring in the Animas River valley alluvial aquifer and to answer important questions about geochemical processes with implications for potential impacts to groundwater quality by the GKM spill and mitigation of possible future mine waste spills. The dynamic groundwater/surface water interactions in the Animas River valley in New Mexico and potential changes to groundwater quality are important to the communities in the region that face potential contamination of domestic wells from historic mining sources and the GKM spill.

This report presents results and conclusions for the second phase of the groundwater study, which focuses on geochemical data for samples collected in fall of 2018 and the spring of 2019. The objectives of this study were:

1. To continue monitoring of groundwater quality and confirm or refute general findings of Newton et al., (2017) specifically related to the hydrogeologic conceptual model;
2. To assess sources of dissolved constituents in shallow groundwater along the Animas River in New Mexico;
3. To assess the occurrence of high manganese and iron concentrations in shallow groundwater;
4. To evaluate redox conditions and processes within the shallow aquifer that affect the solubility of metals associated with the GKM spill;
5. To identify areas in the Animas Valley where surface water, including the river and irrigation canals, actively recharges the shallow groundwater system to potentially contaminate the shallow aquifer.

Water samples were collected during two time periods, fall of 2018 and spring of 2019. These periods were chosen because they typically capture the extremes of the annual hydrologic regime in this region according to Newton et al., (2017). Over most of the study area, groundwater levels are highest in early fall (September and October) due to irrigation water recharging the aquifer over the previous seven months. Groundwater levels during March and April, just before snowmelt reaches the river, are at their lowest, which correlates to base-flow conditions. All groundwater samples were analyzed for major cations and anions, trace metals, and the stable isotopes of oxygen ($\delta^{18}O$) and hydrogen (δD). For a subset of wells, extra samples were collected for the analysis of sulfur and oxygen isotopes in sulfate and carbon isotopes in dissolved inorganic carbon (DIC).

Water level data and geochemical results from this study were very similar to those of Newton et al., (2017). Water level data showed groundwater flowing to the southwest and towards the river, resulting in the river gaining water from the aquifer over the entire reach in New Mexico most of the time. In some localized areas, such as the area near Cedar Hill, some water levels in wells appeared to be below river stage in winter months, indicating a change to losing conditions in these specific locations. Historically low discharge rates in the Animas River in 2018 caused water levels in some wells close to the river to drop below water levels observed in past years and in 2019. However, water levels over most of the study area did not appear to be affected, mainly because groundwater levels in the Animas Valley are largely controlled by irrigation. Irrigation water recharges the shallow aquifer by infiltration through fields and irrigation canals, causing water levels to rise. Water then drains back into the river during the winter months, causing water levels to decrease.

Similar to previous conclusions of Newton et al., (2017) sulfate and total dissolved solids (TDS) concentrations increase down-gradient (to the southwest), reflecting the apparent mixing of fresh river water (irrigation recharge) and at least one high-sulfate, high-TDS regional groundwater component. Stable isotope data for dissolved sulfate was compared to data presented by Nordstrom et al., (2007) which included stable isotopic compositions of sulfate for springs, streams, and rocks in the Upper Animas watershed in Colorado. For groundwater that is chemically similar to river water (fresh water endmember observed in the northern portion of the study area), it appears that sulfate and likely most other dissolved constituents originate from volcanic rocks and alteration minerals in the Animas headwaters in the San Juan Mountains.

The conceptual model that describes geologic controlled upwelling of high-sulfate regional groundwater suggested by Newton et al., (2017) was largely confirmed as the primary factor contributing to the spatial distribution of TDS concentrations, sulfate concentrations, and other dissolved constituents. However, this study highlighted some complexities:

- There are likely at least two high-sulfate mixing endmembers characterized as different water types (sodium-sulfate and calcium-sulfate).
- In addition to mixing processes, evaporation, which is an important process in this system, can also increase relative sulfate concentrations as is observed south of Aztec.
- Water chemistry data and the stable isotopic composition of water indicate that although the additional sulfate observed in the southern portion of the study area appears to

originate from the same geologic source(s), the water sources and flow paths of this high-sulfate water may vary significantly.

- While simple stoichiometric analyses indicates that the minerals gypsum or anhydrite (common minerals in evaporites) are the geologic sources of sulfate for the high-sulfate mixing endmember, paleogene and underlying Cretaceous rocks in the area do not contain significant amounts of gypsum according to geologic literature.
- While stable isotopic compositions of sulfate and DIC appears to show a distinct signature for high-sulfate waters that are upwelling into the shallow system, these data did not conclusively identify the solute source of sulfate in the high-sulfate endmember(s).

While the actual sulfate source for the high-sulfate endmember(s) is unknown, other researchers have described groundwater from underlying Paleogene and Cretaceous rocks with water chemistry similar to that for groundwater samples that we considered to be mixing endmembers in this study. Therefore, the upwelling of regional groundwater from underlying Paleogene rocks as described by Newton et al., (2017) is probably the main mechanism by which the high-sulfate endmember enters the shallow system.

Many dissolved metals of concern (both natural and anthropogenic) are present in surface water in the Upper Animas River watershed, which ultimately defines groundwater chemistry in the northern part of the study area. Fortunately, geochemical conditions (pH and redox) result in the precipitation of most of these metals before entering the groundwater system in New Mexico. We detected no evidence of groundwater contamination related to the Gold King Mine spill or legacy acid mine drainage in the San Juan Mountains. Dissolved manganese and iron that is observed to exceed secondary maximum contaminant levels (MCLs) in some areas is likely due to manganese oxides and iron (hydr)oxides that were deposited as sediments that make up the shallow aquifer.

Dissolved oxygen (DO), which was measured in each well in the field during sample collection, was analyzed for the purpose of identifying areas where the input of contaminated surface water (river and irrigation water) poses potential risk of contaminating the shallow aquifer. The previous phase of this study demonstrated that large increases in DO in groundwater in some wells was due to the input of oxygenated river water, primarily via irrigation. Subsequent decomposition of organic matter causes DO concentrations to decrease, sometimes completely depleting DO. Therefore, the range of observed DO values in groundwater over time can help to identify areas of temporally discrete recharge events related to irrigation and interactions between the river and the shallow groundwater system. We demonstrate the concept of using multiple DO measurements in wells over time to identify these areas of concern. The DOrange/DOmax ratio can be a useful tool for assessing the variability of DO concentrations in wells over time. Larger ratios may be indicative of an area where surface water is recharging the aquifer intermittently, mostly related to irrigation practices. By monitoring wells close to the river, ditches, or agricultural fields on a biweekly or monthly timescale, areas of potential risk of contamination by the input of surface water can likely be identified.

Bridge crossing the Animas River a few miles south of the New Mexico–Colorado border.

I. INTRODUCTION

After the Gold King Mine (GKM) released metal and sludge-laden water into Cement Creek and the Animas River on August 5, 2015, the New Mexico Bureau of Geology and Mineral Resources (NMBGMR) along with other federal and state agencies and tribes, including the U.S. Environmental Protection Agency (EPA), the New Mexico Environment Department (NMED), the United States Geological Survey (USGS), Arizona Department of Environmental Quality, the Colorado Department of Public Health and the Environment, Navajo Nation EPA, the Southern Ute Indian Tribe, the Utah Department of Environmental Quality, and the Ute Mountain Ute Tribe responded with a collaborative research effort to assess potential environmental and economic impacts to New Mexico communities along the Animas River (Figure 1). Researchers at the NMBGMR collected groundwater level and water chemistry data (up to 26 wells) several times between January 2016 and June 2017 (Newton et al., 2017). These data were used to characterize the local hydrogeology and to identify potential impacts from the GKM spill on local groundwater quality. Hydrogeologic characterization included the evaluation of recharge sources, groundwater flow directions, and groundwater/surface water interactions. The resulting hydrogeologic conceptual model provided a framework, under which general water chemistry and trace metal data were interpreted to assess contamination associated with the GKM spill.

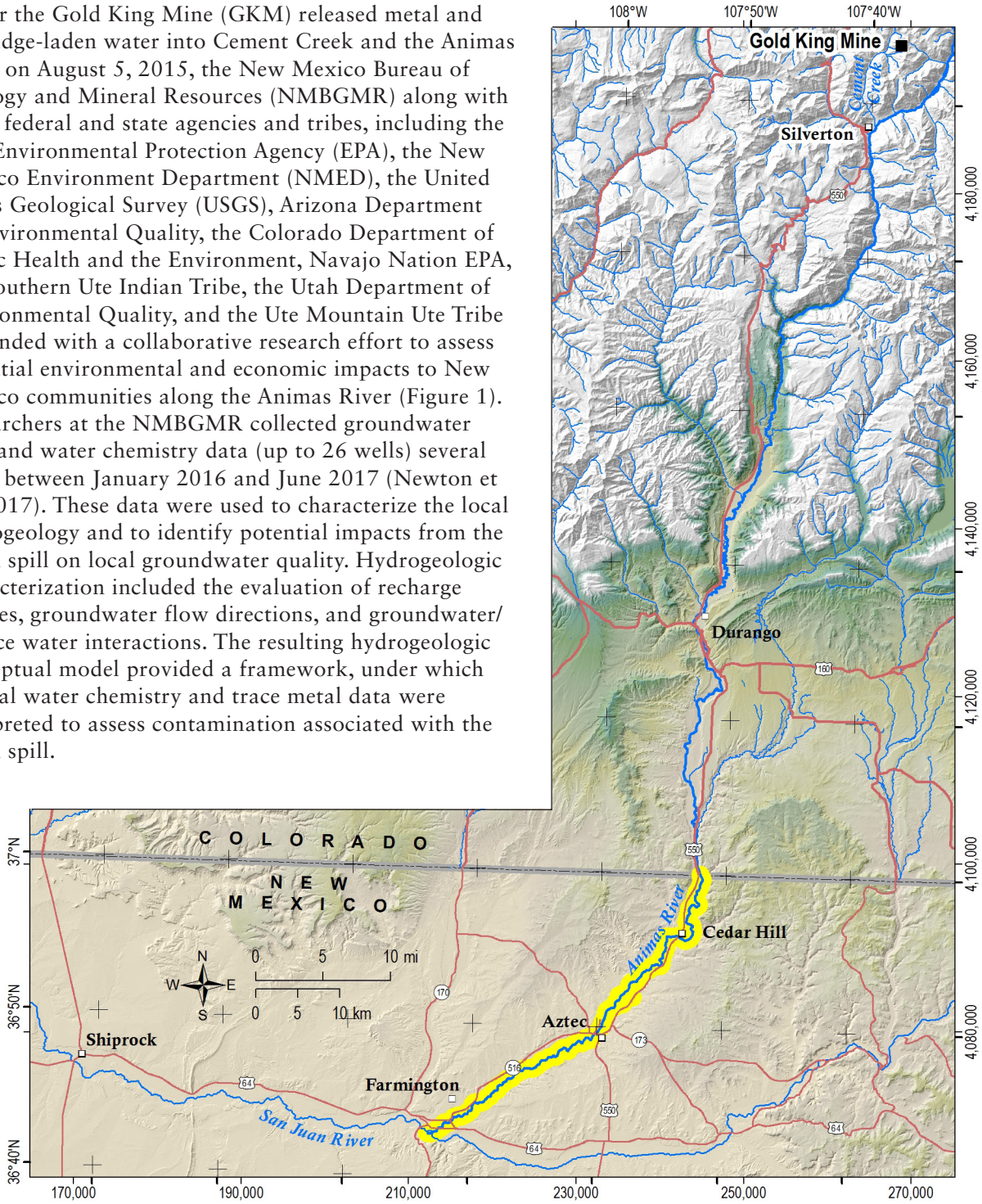

Figure 1. The study focused on the reach of the Animas River outlined in yellow, from the Colorado–New Mexico state line to Farmington.

While Newton et al., (2017) found no evidence of groundwater contamination that was directly associated with the GKM spill, it was determined that there may still be potential risk related to the possible deposition of contaminated sediments from river water diverted for use in local irrigation ditches and subsequent mobilization of these contaminants into the shallow aquifer. Furthermore, it was determined that although the New Mexico reach of Animas River usually gains water from the aquifer there is still potential for wells close to the river in some localized areas to capture river water under certain conditions. The 2017 NMBGMR study also generated questions about redox conditions, specifically related to the spatial distribution and source(s) of iron and manganese, the only two metals observed at several locations to exceed the EPA secondary maximum contaminant levels (SMCLs) for drinking water.

The lack of evidence of harmful effects of the GKM spill on groundwater quality may have been due to the timing of the 2017 study and the small sample size. Future work suggested from the study included continued monitoring of groundwater quality to assess impacts from the GKM spill and the evaluation of areas that are at risk for potential contamination from the direct input of surface water. Newton et al., (2017) also recommended additional geochemical analyses to assess the occurrence of high manganese and iron concentrations, including the evaluation of redox conditions and solute source identification.

This report describes the results of a subsequent NMBGMR study with the following objectives:

1. To continue monitoring groundwater quality in the shallow alluvial aquifer in the Animas Valley of New Mexico for the purpose of identifying groundwater quality impacts due to the GKM spill or legacy acid mine drainage occurring in the Animas headwaters in Colorado.To confirm or refute general findings of Newton et al., (2017), specifically related to the hydrogeologic conceptual model.
2. To confirm or refute general findings of Newton et al., (2017), specifically related to the hydrogeologic conceptual model.
3. To assess the source of dissolved constituents, such as sulfate, sodium, bicarbonate, manganese, and iron in shallow groundwater along the Animas River in New Mexico.
4. To evaluate redox conditions and processes within the shallow aquifer that affect the solubility of metals associated with the GKM spill, including manganese and iron.
5. To identify areas in the Animas Valley where surface water, including the river and irrigation canals, actively recharges the shallow groundwater system, posing a potential risk of contaminating the shallow aquifer.

For this study, we collected 74 groundwater samples in the fall of 2018 and 57 samples in the spring of 2019, resulting in a much denser well coverage throughout the study area compared to Newton et al.,(2017). All samples were analyzed for major ions, trace metals and the stable isotopes of oxygen and hydrogen. Additional isotopic analyses [$\delta^{34}S$ and $\delta^{18}O$ in sulfate, $\delta^{13}C$ in dissolved inorganic carbon (DIC)] for a subset of samples greatly helped to assess geologic solute sources and hydrogeochemical processes that control groundwater chemistry in the study area. We also used the relationship between dissolved oxygen concentrations and total dissolved solids (TDS), observed by Newton et al., (2017) to identify areas where there is active infiltration of irrigation water recharging the shallow aquifer, posing a potential risk of contamination.

While our previous conclusions (Newton et al., 2017) were largely confirmed, the additional data increased our understanding of the system and added many details with respect to identifying actual solute sources and complexities related to local, intermediate, and regional flow paths. Most shallow groundwater at the northern part of the study area chemically resembles river water (calcium-bicarbonate water type) due to the dissolution of volcanic rocks and hydrothermal minerals in the Upper Animas watershed in Colorado. Increased sulfate concentrations in groundwater in the down-gradient direction (southwest) is due to the input of water that has resided in underlying sedimentary rocks that lie below the shallow alluvial aquifer. The mixing of these two end-members (river water and high-sulfate regional groundwater) shows a spatial trend indicative of more high-sulfate water entering the shallow system to the southwest. Wells that produce water that is high in iron and manganese do not show a spatial trend due to this mixing process. Therefore it is likely that these high manganese and iron waters are a result of more local processes. We also demonstrate the concept of using multiple dissolved oxygen (DO) measurements in wells over time to identify areas where the input of contaminated surface water (river and irrigation water) poses potential risk of contaminating the shallow aquifer.

II. PREVIOUS WORK

Newton et al., (2017) analyzed water level and geochemical data from numerous wells for different seasonal river flow regimes between January 2016 and June 2017. These data, along with previous geologic and hydrologic studies, were utilized to construct a hydrologic conceptual model that describes groundwater flow paths at different scales, groundwater/surface water interactions, and how these processes change over time. Geochemical data also provided information about potential groundwater contamination related to the GKM spill, legacy acid mine drainage, and other sources. This section briefly describes the conceptual model and data interpretations by Newton et al., (2017).

Geology

The Animas River is located on the northwestern margin of the San Juan Basin, which is an asymmetric structural depression in the Colorado Plateau province. The geology of the area as described by Craigg (2001), consists of terrestrial and marine sedimentary rocks of late Cretaceous to Paleogene age (Figure 2). The Upper Cretaceous rocks include the Dakota Sandstone, Mancos Shale, Lewis Shale, Pictured Cliffs Sandstone, the Fruitland Formation and the Kirtland Shale. While these units are not an important water source in the Animas Valley, many of them serve as aquifers in other areas in the basin (Kelley et al., 2014). Cretaceous sandstone beds and silty to sandy mudstone beds, such as the Dakota, Point Lookout, and Pictured Cliffs Sandstones, are the primary producers of oil and gas in the San Juan Basin (Fassett, 2010). The depth of the Cretaceous rocks along the Animas River varies from several hundreds of feet below the surface Near Durango to zero feet near Farmington, where outcrops of late Cretaceous (~75 Ma) Kirtland Shale are found.

Paleogene rocks, including the San Jose and Nacimiento Formations, form the cliffs that bound the Animas Valley and lie directly below the valley-fill that that makes up the shallow alluvial aquifer. Near Durango, along the Animas River (Figure 3), outcrops of the Animas Formation are observed, which is made up of interbedded tuffaceous sandstone, conglomerate and shale. In the Cedar Hill region, the nearby surrounding hills/mesas are composed primarily of Eocene (~50–55 Ma) San Jose Formation and Paleocene (~60–65 Ma) Nacimiento Formation. The San Jose is an interbedded, very fine to coarse-grained arkosic sandstone. The Nacimiento Formation consists of interbedded gray shale, and discontinuous lenses of sandstone and interfingers with the Paleocene Ojo Alamo Sandstone, which consists of arkosic sandstone and conglomerate. The Ojo Alamo Formation outcrops just north of Farmington, New Mexico. While these Cenozoic rocks are important aquifers in other parts of the San Juan Basin in Colorado and New Mexico (Kelley et al., 2014; Robson and Winfield, 1995) there are very few water wells in the Animas Valley that are completed in these units. There are no known major structural features (i.e. faults or folds) along the river corridor.

The Animas River from the Colorado–New Mexico border flows through Quaternary alluvial deposits, which make up the shallow alluvial aquifer. The Quaternary alluvium is largely made up of sediment eroded from Paleogene rocks into which the Animas River has incised. While municipal or regional drinking water is largely sourced from the Animas River, most private domestic wells in the valley rely on the alluvial aquifer, with well depths of about 30 to 60 feet.

Hydrology

Animas River

The headwaters of the Animas River originate high in the San Juan Mountains, in the Silverton Mining District. The main tributaries that contribute to the Animas in Colorado include Cement Creek and Mineral Creek near the headwaters, numerous small streams in Animas Canyon between Silverton and Durango, and the Florida River just north of the New Mexico–Colorado border. The Animas River

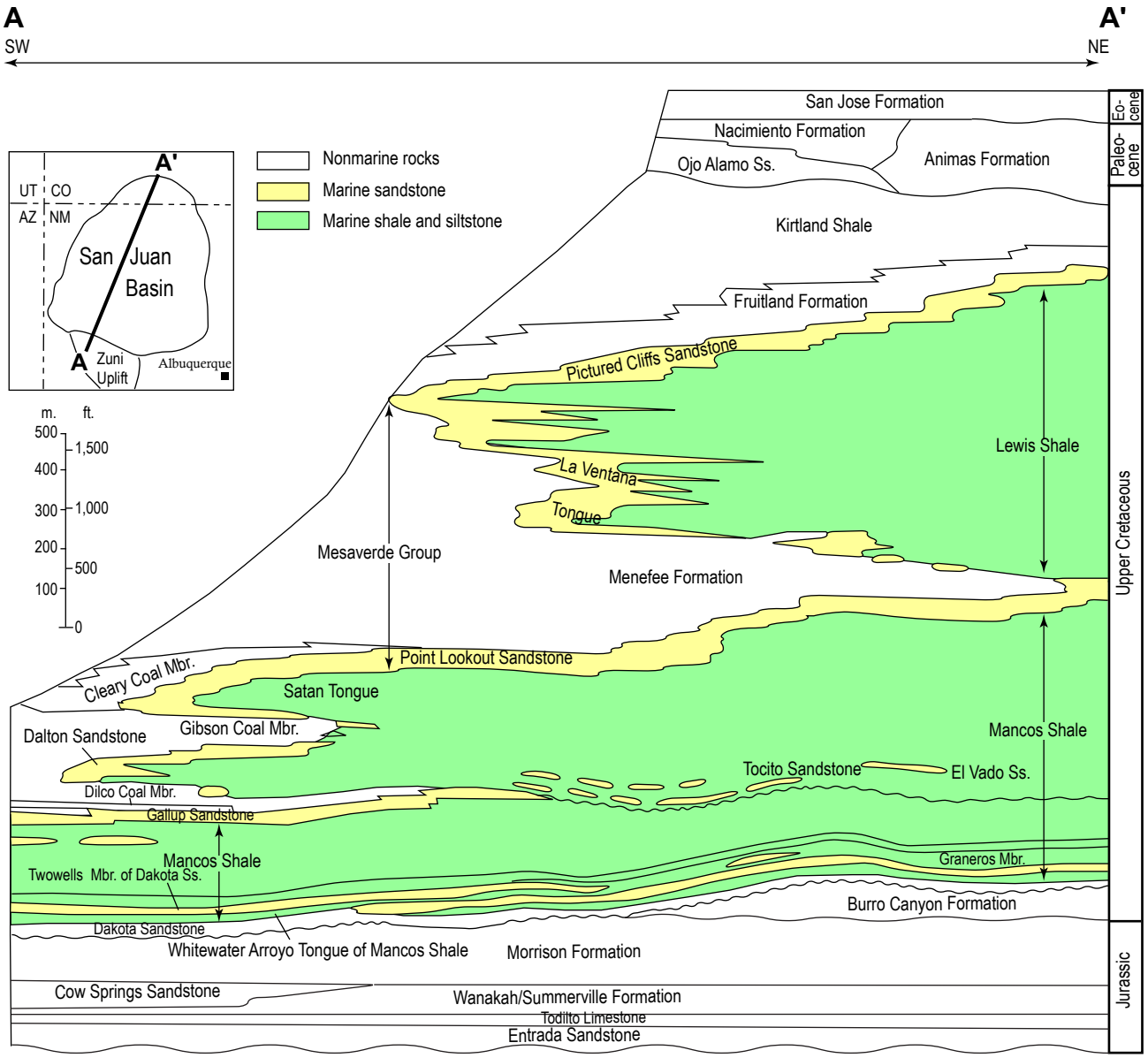

Figure 2. Geologic cross-section of the San Juan Basin (Kelley et al., 2014).

meanders roughly 40 miles from the New Mexico border, to Farmington, where it joins the San Juan River. The San Juan River flows an additional ~180 miles through New Mexico and Utah before discharging into Lake Powell.

The discharge of the Animas River fluctuates seasonally. The river is often lowest during early fall as result of diversions for irrigation and higher evapotranspiration rates. Moving into fall and winter the river remains relatively steady at roughly 300 cubic feet per second (cfs). Discharge begins to rise slowly in April as early snowmelt enters the river. Discharge continues to increase throughout May and typically reaches peak discharge between late May and mid-June as the main pulse of snowmelt moves through the river. The discharge declines through late summer as the snowpack diminishes. Throughout the late summer, river discharge often rises rapidly as result of monsoon storms, before ebbing back to previous levels. By late August the river returns to a baseflow.

For this study, we sampled groundwater during September and October 2018 and April 2019. Figure 4 shows average daily discharge for 2018 and 2019 compared to historic average daily discharge on the Animas River below Aztec, NM between 2003 and 2019. Average daily discharge on the Animas during 2018 was observed to be extremely low compared

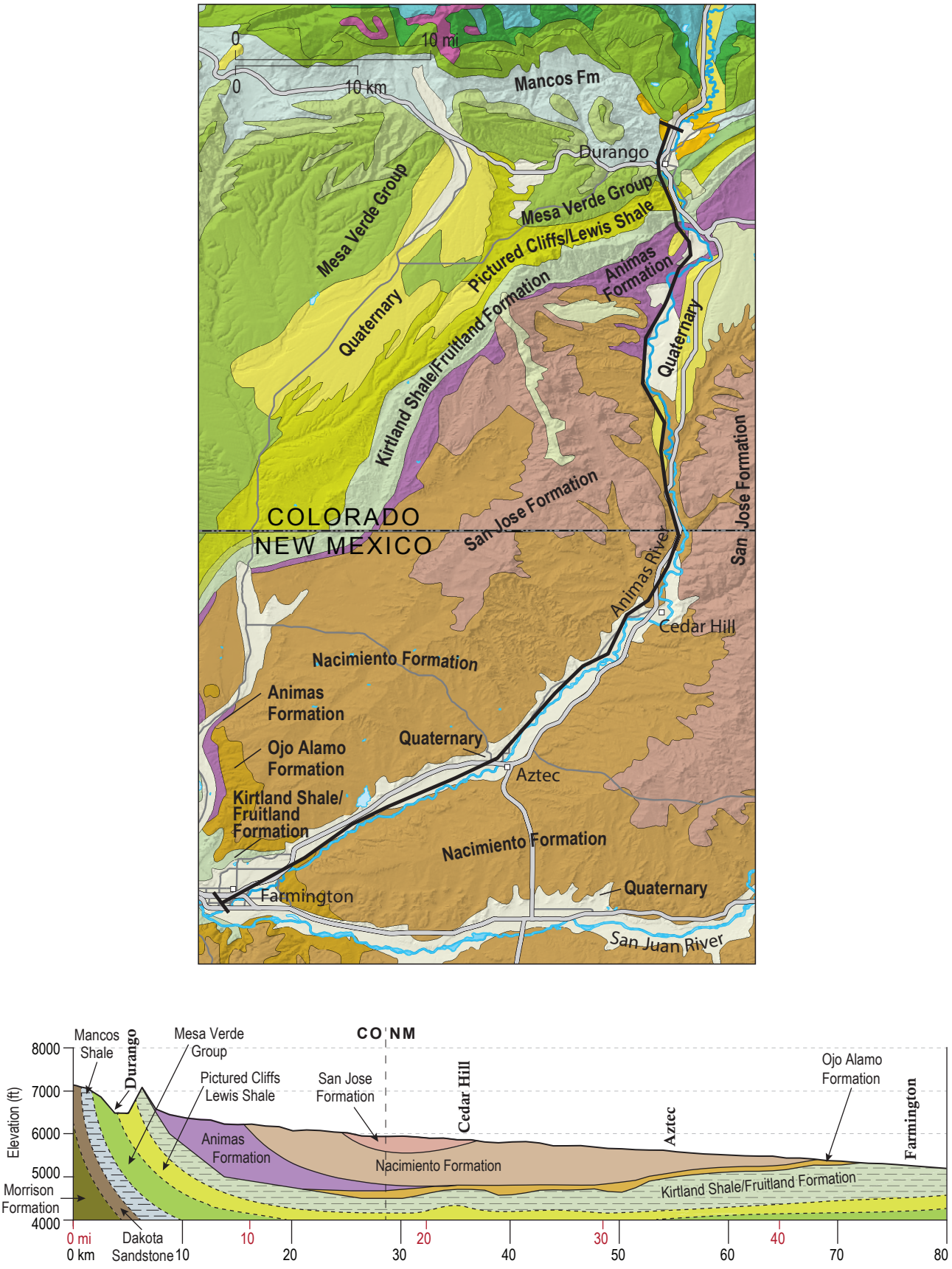

Figure 3. Geologic map and cross-section along the Animas River (Newton et al., 2017).

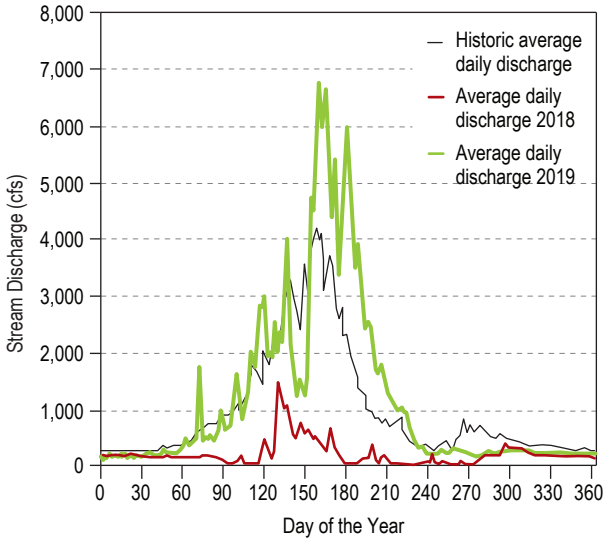

Figure 4. Average daily discharge for 2018 (red line), 2019 (green line), and historic average daily discharge between 2003 and 2019 (black line) on the Animas River below Aztec, NM (USGS 09364010).

to historic average flows. The spring runoff peak shown in Figure 4 for 2018 occurred in early May with discharge rates less than 2000 cfs. The Center for Snow and Avalanche Studies (CSAS) reported that cumulative flow in the Animas River during the 2018 snowmelt season (March 1 through June 30) was 33% of the median (CSAS, 2018). Average daily discharge in 2019 was much higher, with a more typical spring runoff peak discharge and timing.

Groundwater Levels—In general, groundwater flows parallel to the river (northeast to southwest) and discharges into the river. Groundwater levels in the shallow alluvial aquifer throughout much of the Animas Valley in New Mexico are strongly linked to irrigation practices and seasonal river stage fluctuations (Newton et al., 2017). Figure 5 shows the range of seasonal fluctuations observed in different wells in 2016. To better understand the hydrodynamics of the alluvial aquifer, Newton et al. (2017) classified the wells with sufficient temporal measurement density (three or more water level measurements per

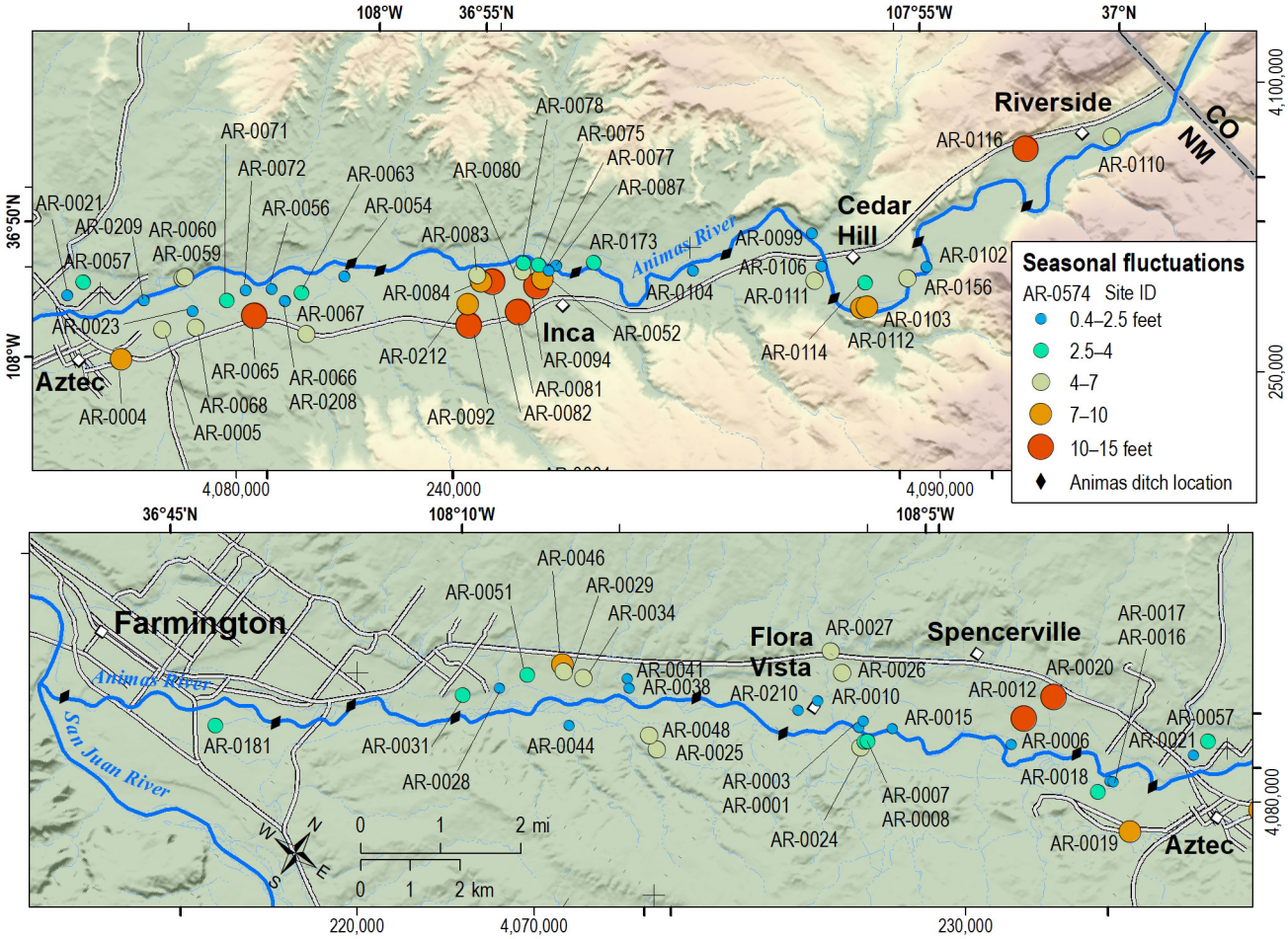

Figure 5. Seasonal groundwater level fluctuations in wells completed in the shallow alluvial aquifer in the Animas Valley observed in 2016 (Newton et al., 2017).

year) into three hydrograph trend types. The trends were characterized by the magnitude of the seasonal fluctuations, and the timing of the peak in groundwater level. Three main hydrograph trends were identified; irrigation-controlled, river stage-controlled, and winter-recharge/ summer-evapotranspiration. The irrigation-controlled and river stage-controlled trends, which were observed for the majority of wells, are described below.

An irrigation-controlled hydrograph trend (Figure 6A) was observed in 38 of 70 wells. When the ditches are first filled in late March, the groundwater level begins to rapidly rise and continues to increase through June, and generally doesn't reach its maximum until late July. Water levels typically remain elevated in these wells until the end of the irrigation season, when the ditches are shut off. At this point, there is a sharp drop in water levels as the ditches are no longer supplying water to the alluvial aquifer, and groundwater discharges to the river. The declining leg of these hydrographs begins flattening as the water level appears to approach equilibrium before the irrigation season begins again. The irrigation season is important both for the economy of the area and the recharge of the alluvial aquifer. The return groundwater flow from irrigated land and the water lost through the base of the irrigation ditches supports the water table. This in turn contributes to gaining river conditions seen throughout the valley.

Water levels in several wells (22 of 70) in close proximity to the river (<350 ft) more closely correlate with river stage (Figure 6B), reflecting the hydraulic connection between the aquifer and the river. Water levels begin increasing in early May, correlating with river flows being fed by snowmelt in the mountains. Peak water levels in these wells are usually reached by the end of May or early June.

As mentioned above, the Animas River, within New Mexico, is generally characterized as a gaining river, where groundwater discharges to the river. The river certainly gains water from the aquifer along the NM reach during irrigation season while groundwater levels are high. However, during base-flow conditions (January—March), when river stage and groundwater levels are at their lowest, Newton et al. (2017) observed localized areas where the hydraulic gradient between the river and the aquifer decreased significantly and sometimes reversed to where the river was likely losing water to the groundwater system. The two areas where this apparent gradient reversal was observed were near Cedar Hill and the area labeled Inca in Figure 5. These apparent gradient reversals have implications for potential contamination of the groundwater.

Groundwater Chemistry—Newton et al. (2017) sampled thirty-one wells in the study area (Figure 7), most of them being sampled multiple times during different river flow regimes between January 2016 and June 2017. All samples were analyzed for major cations and anions, trace metals, and the stable isotopes of oxygen and hydrogen. Figure 8 shows groundwater chemistry data plotted on a Piper diagram and the spatial distribution for the different water types. Most groundwater sampled north of Aztec exhibits a calcium-bicarbonate water type, indicative of the dissolution of calcite or limestone. Total dissolved solids (TDS) concentrations for these waters are well below 1,000 mg/L. As groundwater flows down-gradient towards the southwest, sulfate and TDS concentrations increase significantly, with many TDS concentrations exceeding 1,000 mg/L. This increase in sulfate and TDS concentrations is especially evident south of Aztec. The water samples from

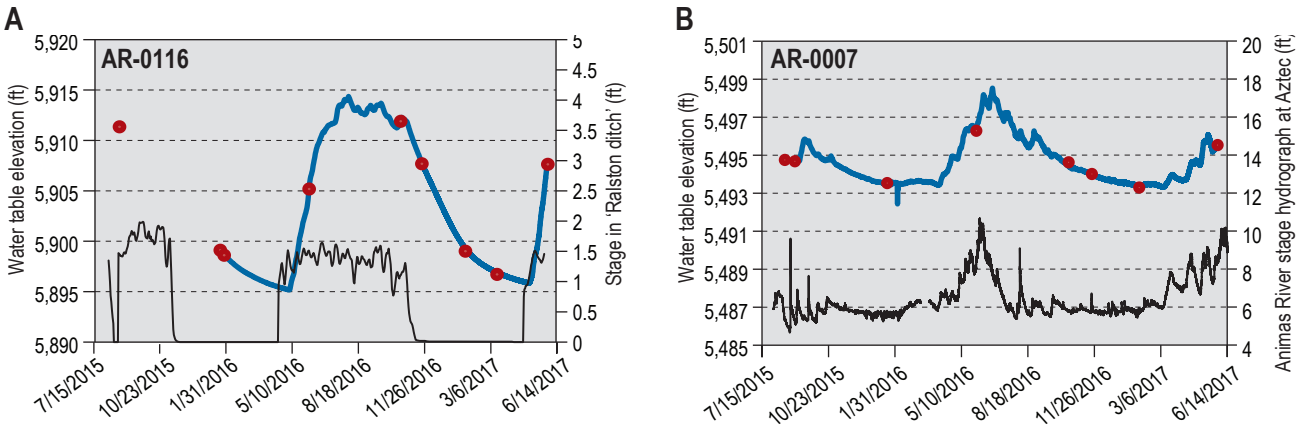

Figure 6. Examples of A) Irrigation controlled well (AR-0116) and B) river stage controlled well (AR-0007). Continuous water level data (blue line), manual measurements (red data points), stage in irrigation ditch and river for A and B respectively (Newton et al., 2017) (black line).

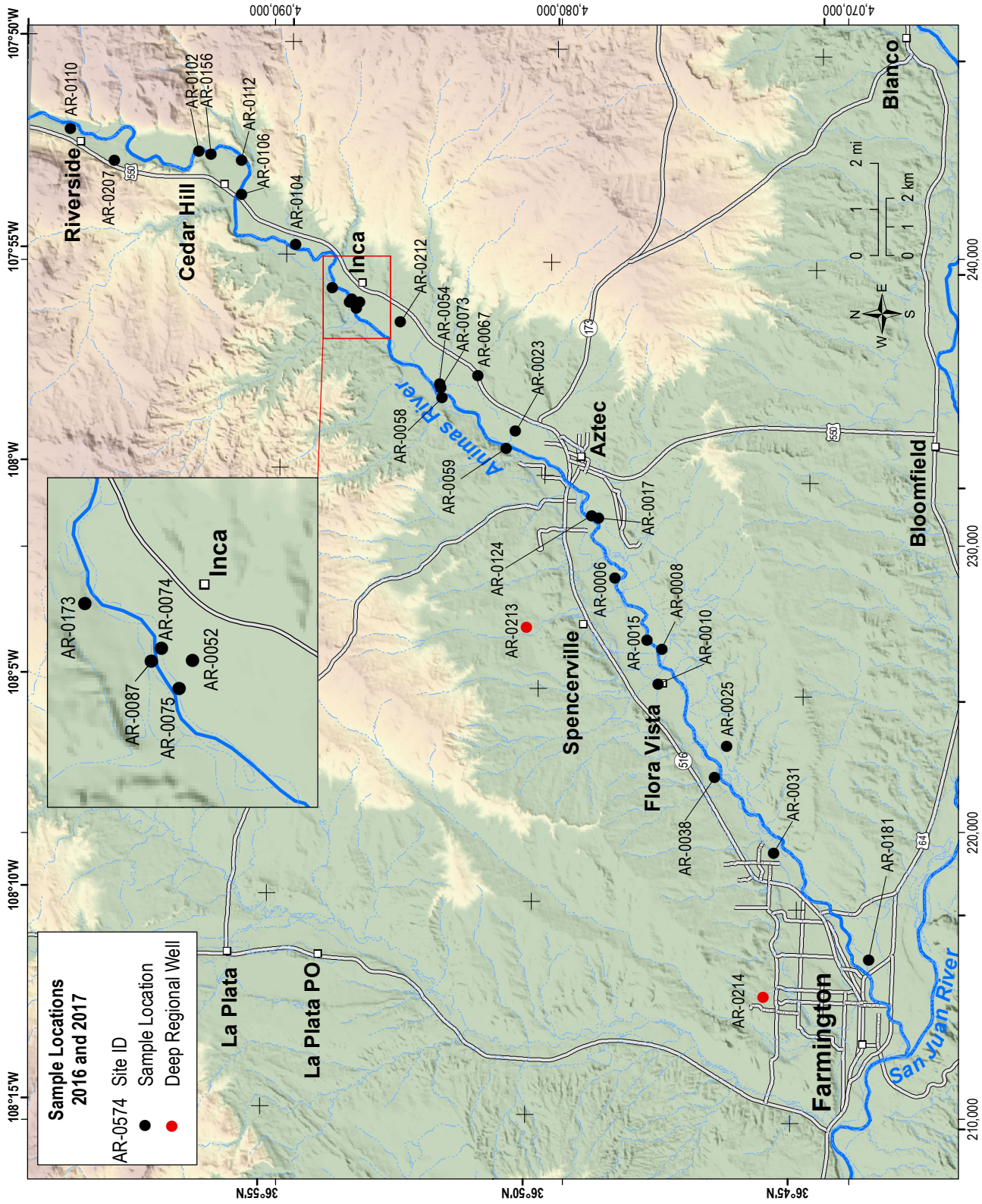

Figure 7. Wells that were sampled by Newton et al., (2017) between January 2016 and June 2017.

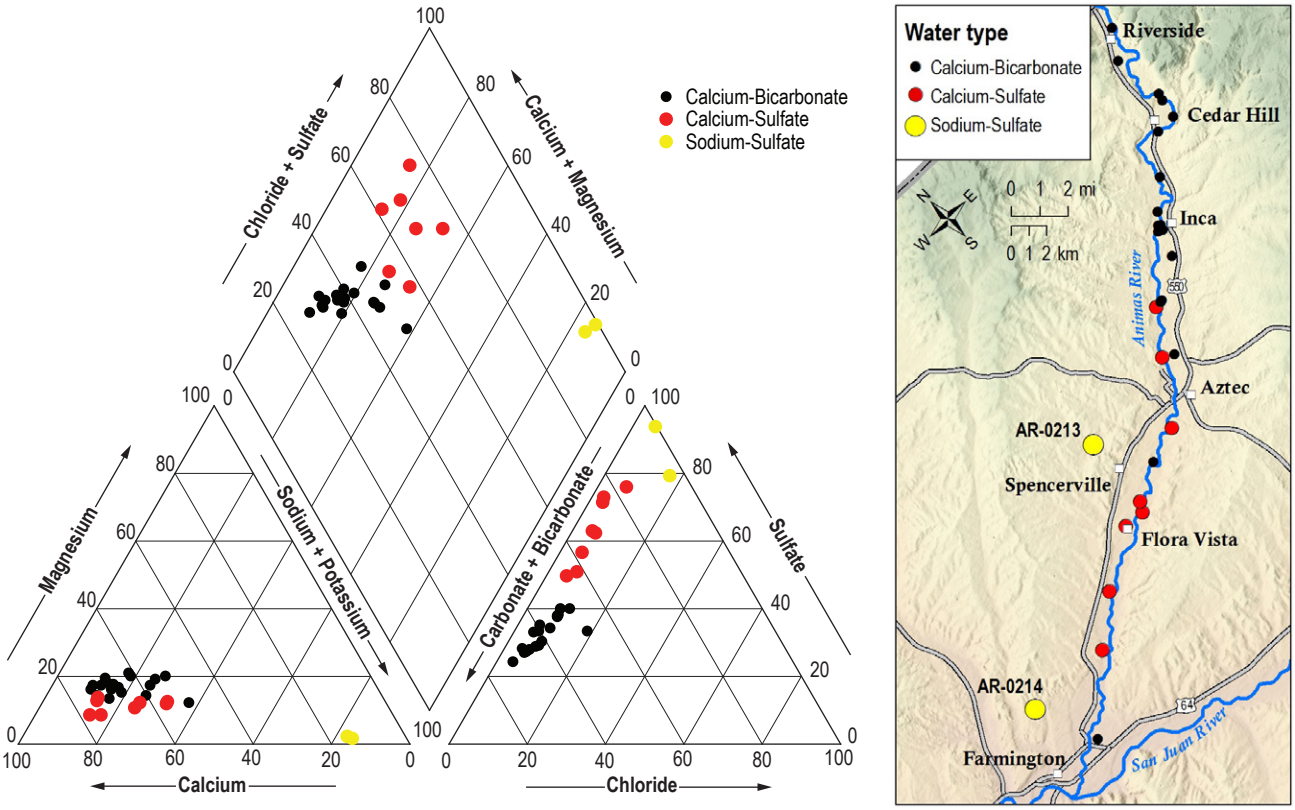

Figure 8. Piper diagram showing the relative major ion concentrations for river water and groundwater (left), locations of wells that exhibit different water types (Newton et al., 2017).

wells AR-0213 and AR-0214, which exhibit a sodium-sulfate water type, were collected from wells that are likely completed in the Nacimiento Formation just outside the Animas valley (Figure 7). Therefore this water was thought to represent regional groundwater that exists at greater depths below the alluvial aquifer. The Piper diagram in Figure 8 shows that Animas River water generally plots as calcium-bicarbonate water, similar to groundwater sampled at the northern end of the study area. Newton et al., (2017) used a simple two-endmember mixing model to show that much of the observed groundwater chemistry can be explained by the mixing of older regional groundwater and river water, which is the dominant endmember (>80% of mixture). The regional endmember was represented by the water sample collected from the well AR-0213, with a TDS concentration of about 10,000 mg/L, an exceptionally light isotopic signature, and an apparent carbon-14 age of approximately 20,000 years before present. Newton et al. (2017) suggested that this apparent mixing was due to the upwelling of high-total dissolved solids, sulfate-rich regional groundwater as a result of the thinning of the Nacimiento and Ojo Alamo Formations as shown in Figure 9. While this mixing model explained the observed distribution of many of the major ions, observed concentrations for other dissolved constituents, such as sodium, chloride, and bicarbonate, did not fit the mixing model as well, and therefore indicated a more complex system.

Over all, this interpretation of water chemistry data is consistent with the water level data described above. The primary source of irrigation water is the Animas River which is diverted and delivered to fields through a series of irrigation canals. Figure 10 shows continuous water level and specific conductance (SC, used as a proxy for TDS concentrations) data for four different wells and an irrigation ditch that show direct evidence of irrigation water recharging the alluvial aquifer. The initiation of irrigation, indicated by the instantaneous filling of the irrigation ditch, coincides with increases in groundwater levels and decreases in specific conductance due to the mixing of fresher surface water and more concentrated groundwater. All samples collected by Newton et al., (2017) exhibited chemical concentrations below the maximum contaminant levels (MCLs) as defined by the EPA National Primary Drinking Water Regulations that were established to protect against consumption of drinking water contaminants that present a risk

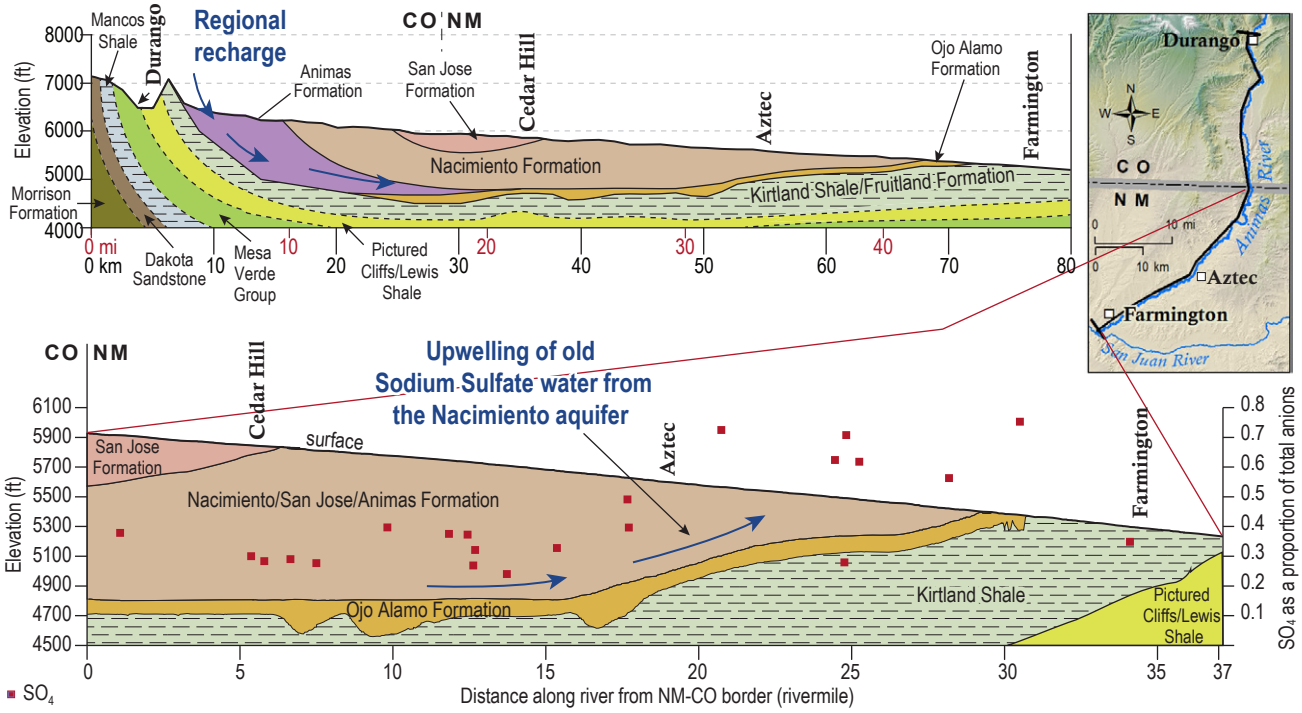

Figure 9. Conceptual model showing the upwelling of regional high-sulfate groundwater into the shallow aquifer due to the thinning of the Nacimiento Formation. Red data points show the relative sulfate conentration according to the y-axis on the right, Newton et al., (2017).

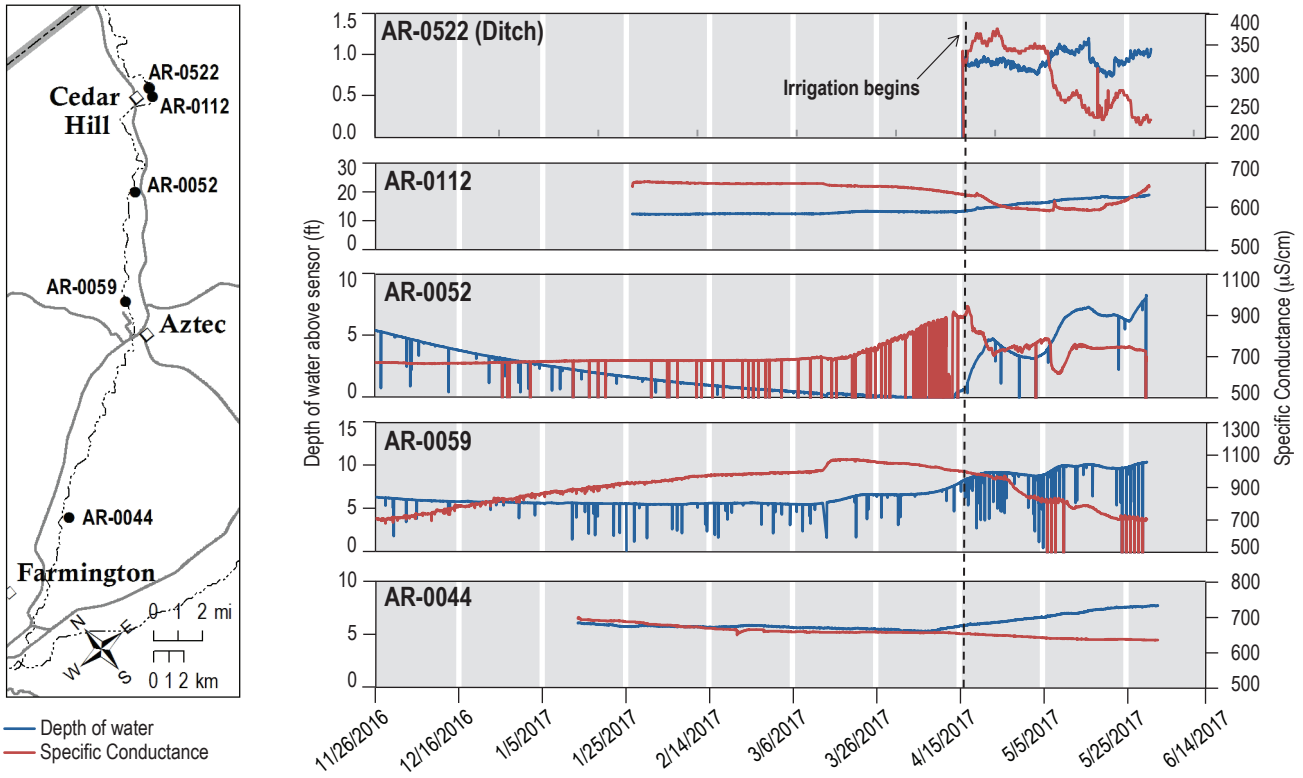

Figure 10. Continuous water level and specific conductance data in four wells and an irrigation ditch. In general, there is an inverse correlation between specific conductance and water levels in the wells. The instantaneous decreases (vertical lines) in water level and specific conductance are caused by pumping. Specific conductance decreases to near zero when water level drops below the sensor (Newton et al., 2017).

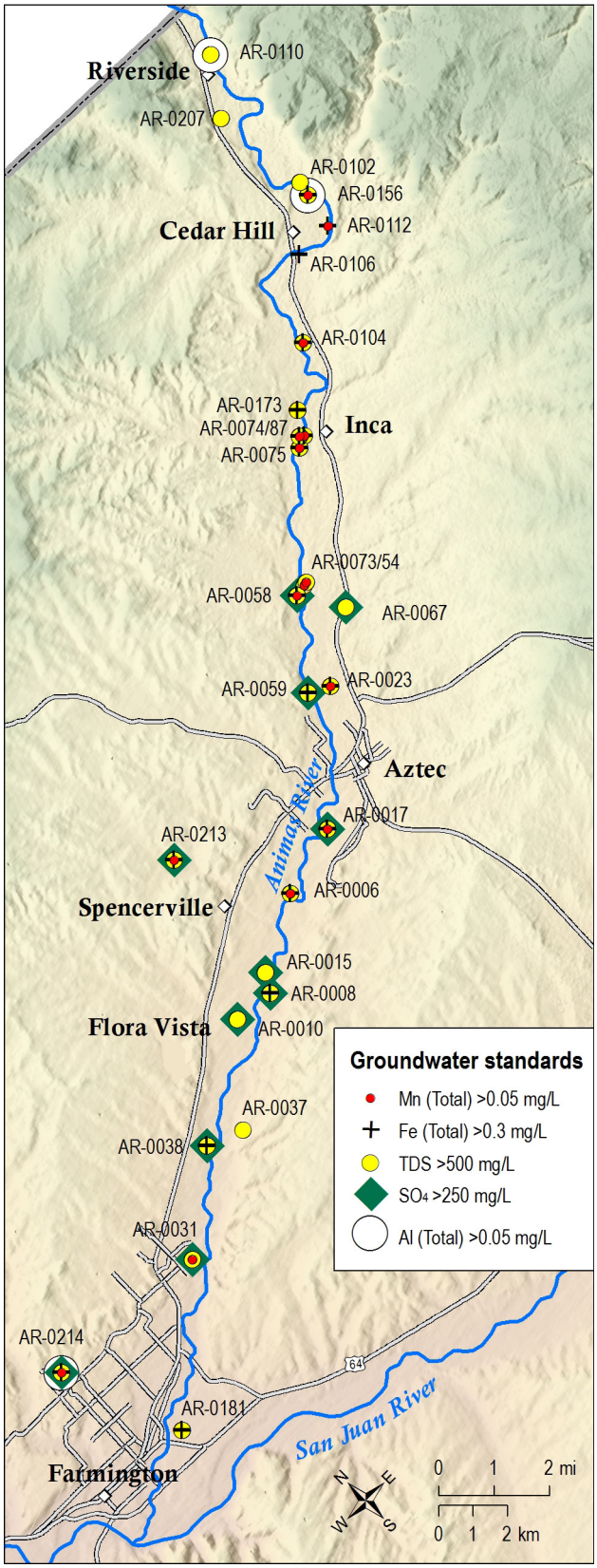

Figure 11. Location of wells that produced water exceeding US EPA secondary maximum contaminant levels for total dissolved solids (TDS), sulfate (SO_4), total iron (Fe), total manganese (Mn), and total aluminum (Al) (Newton et al., 2017).

to human health. However, some constituents were observed to exceed secondary maximum contaminant levels (SMCLs) as defined by the US EPA secondary drinking water regulation, which is a non-enforceable guideline regarding cosmetic or aesthetic effects (Figure 11). Constituents for which measured concentrations were observed to exceed the SMCLs include total dissolved solids (TDS), sulfate, chloride, iron, manganese, and aluminum.

Manganese and iron were the only two dissolved metals in groundwater that were frequently observed at concentrations that significantly exceeded US EPA secondary maximum contaminant levels. These high iron and manganese concentrations appear to be associated with Eh values less than 200 millivolts (Newton et al., 2017), and although the primary recharge source, which is river water via irrigation, is well oxygenated, measured Eh values and the ubiquitous presence of dissolved manganese indicates that dissolved oxygen is consumed quickly, resulting in manganese oxides and iron hydroxides being the main redox buffers. It is difficult to determine the source of the iron and manganese. This study aimed to assess redox conditions in the shallow aquifer to better evaluate iron and manganese sources.

NMBGMR staff member measuring the water level in a domestic well on the bank of the Animas River, New Mexico.

III. METHODS

Water Sampling

Sampling protocols used by New Mexico Bureau of Geology and Mineral Resources are described in more detail by Timmons et al., (2013), and as specified in the NMBGMR protocols for clean sampling (Appendix D). The goal was to collect water samples that were chemically representative of local groundwater from existing domestic and irrigation wells that were equipped with pumps. Most of these wells are used regularly, and therefore well bore water is mobile and likely does not reside in the well casing long enough for the chemical composition of the water to change significantly. However, we still took extra precautions to ensure the integrity of the water sample. General water sampling procedures include purging the well until field parameters [pH, dissolved oxygen, specific conductivity, oxidation-reduction potential (ORP), and temperature], which are being monitored in real time, stabilize before collecting the sample. In order to prevent contamination of the samples from external sources and cross-contamination from other samples, we followed a strict sampling protocol (Appendix D). All sampling equipment was cleaned using laboratory soap and rinsed with deionized water immediately prior to each sampling event and at the end of each day during the sampling event. A separate clean sampling manifold and tubing was used for each well and Nitrile gloves were worn during the sampling procedure.

Water samples were collected during two time periods, fall of 2018 (September 24–October 11, 74 samples) and spring of 2019 (April 1–10, 54 samples) (Figure 12a, b, and c). These periods were chosen because they typically capture the extremes of the annual hydrologic regime in this region according to Newton et al., (2017). Over most of the study area, groundwater levels are highest in early fall (September and October) due to irrigation water recharging the aquifer over the previous seven months. Groundwater levels during March and April, just before snowmelt reaches the river, are at their lowest, which correlates to base-flow conditions. Newton et al., (2017) noted some differences in water chemistry that correlated with seasonal changes in the hydrologic regime. Information about all water sampling sites is available in Appendix A. Table 1 lists well locations, approximate total depths, sample events during which each well was sampled, and the figure that shows each well location. All wells sampled for this study, except AR-0217 were private domestic and irrigation wells completed in the shallow alluvial aquifer in the Animas Valley. The well AR-0217 (Figure 12c) is located north of Farmington, outside of the river valley and is likely completed in the Nacimiento Formation at around 339 feet bgs. This well was included in this study with a goal of sampling regional groundwater.

All groundwater samples were analyzed for major cations and anions, trace metals, and the stable isotopes of oxygen ($\delta^{18}O$) and hydrogen (δD). In addition, for the fall 2018 sampling event only, samples were analyzed for dissolved organic carbon (DOC) and total organic carbon (TOC). For a subset of wells (21 samples for fall 2018, 18 samples for spring 2019, Figure 13), additional samples were collected for the analysis of sulfur and oxygen isotopes in sulfate and carbon isotopes in dissolved inorganic carbon (DIC). For trace metals and major cations, total and dissolved concentrations were determined. Water to be analyzed for dissolved trace metals and cations was filtered (0.45 micron filters) and acidified with nitric acid in the field. Water samples to be analyzed for total trace metals and cations were also acidified but were not filtered so that any constituents of interest that were adsorbed to colloids and small particulates would be included in the analysis.

Analyses for trace metals, major ions and stable isotopes of oxygen and hydrogen were performed at the Chemistry Lab at New Mexico Bureau of Geology and Mineral Resources. Samples to be analyzed for sulfur and oxygen isotopes in sulfate and carbon isotopes in DIC were sent to the Center for Stable Isotopes at the University of New Mexico, in Albuquerque, NM. Samples to be analyzed for DOC and TOC were sent to Hall Environmental Analysis Laboratory in Albuquerque, NM. Geochemical modeling to determine chemical speciation and

Table 1. Wells sampled for this study. Years that wells were sampled and the figure that shows each well location are also indicated.

WELL LOCATION				SITE INFORMATION					
Point ID	UTM Easting NAD83, Zone 13	UTM Northing NAD83, Zone 13	Elevation (ft)	Well depth (ft bgs)	2019	2018	2017	2016	Map figure
AR-0003	226176	4076850	5497	27	x	x			Figure 12b
AR-0004	233702	4079960	5660	58	x	x			Figure 12b
AR-0005	233838	4080950	5642	62	x	x			Figure 12b
AR-0006	228880	4078170	5537		x	x	x	x	Figure 12b
AR-0008	226419	4076530	5504	21	x	x	x	x	Figure 12b
AR-0010	225194	4076660	5517	38	x	x	x	x	Figure 12b
AR-0017	230984	4078740	5571	17	x	x	x	x	Figure 12b
AR-0019	231810	4078110	5646	68	x	x			Figure 12b
AR-0021	232008	4080090	5629	49	x	x			Figure 12b
AR-0023	234008	4081640	5643	31	x	x	x	x	Figure 12b
AR-0024	226448	4076370	5510	25	x	x			Figure 12b
AR-0025	223102	4073990	5599	48	x	x			Figure 11c
AR-0027	224833	4077610	5567	48		x			Figure 12b
AR-0031	219294	4072630	5383	14		x	x	x	Figure 12c
AR-0034	221070	4074330	5452		x	x			Figure 12c
AR-0038	221948	4074690	5442	35		x	x	x	Figure 12c
AR-0041	221789	4074810	5467		x	x			Figure 12c
AR-0046	220537	4074320	5463		x	x			Figure 12c
AR-0051	220096	4073740	5428	49	x	x			Figure 12c
AR-0052	238534	4087080	5739			x	x	x	Figure 12a
AR-0054	235654	4084290	5685	26		x	x	x	Figure 12b
AR-0057	232064	4080490	5638	49	x	x			Figure 12b
AR-0058	235190	4084200	5677	21	x	x	x	x	Figure 12b
AR-0059	233406	4081960	5658	50	x	x	x	x	Figure 12b
AR-0065	234946	4082450	5694		x	x			Figure 12b
AR-0066	235177	4083100	5665			x			Figure 12b
AR-0070	234425	4082180	5652		x	x			Figure 12b
AR-0074	238641	4087350	5742	20		x	x	x	Figure 12a
AR-0075	238293	4087200	5733		x	x	x	x	Figure 12a
AR-0077	238501	4087240	5739			x			Figure 12a
AR-0080	238130	4086890	5733	26	x	x			Figure 12a
AR-0081	238644	4086260	5782		x	x			Figure 12a
AR-0086	238419	4087760	5834	39		x			Figure 12a
AR-0087	238528	4087440	5739			x	x	x	Figure 12a
AR-0088	238408	4087580	5783	30	x	x			Figure 12a
AR-0094	238533	4086880	5756			x			Figure 12a
AR-0102	243793	4092680	5856	23	x	x	x	x	Figure 12a
AR-0104	240539	4089310	5782			x	x	x	Figure 12a
AR-0106	242278	4091200	5824		x	x	x	x	Figure 12a
AR-0110	244588	4097170	5946		x	x	x	x	Figure 12a
AR-0112	243470	4091200	5839		x	x	x	x	Figure 12a
AR-0115	243666	4091830	5861		x	x			Figure 12a
AR-0120	227636	4076990	5517	27	x	x			Figure 12b
AR-0122	239880	4088771	5795			x			Figure 12a
AR-0132	243670	4091423	5846			x			Figure 12a
AR-0148	240511	4088877	5781		x	x			Figure 12a
AR-0151	237621	4086363	5735	24	x	x			Figure 12a
AR-0156	243694	4092265	5860	35		x	x	x	Figure 12a
AR-0161	234703	4083789	5668	30	x	x			Figure 12b
AR-0173	239035	4088019	5797	43	x	x	x	x	Figure 12a
AR-0181	215547	4069320	5331	30	x	x	x	x	Figure 12c
AR-0187	241481	4091550	5970		x	x			Figure 12a
AR-0190	236474	4085137	5708	44	x	x			Figure 12b
AR-0198	236949	4085450	5728		x	x			Figure 11b
AR-0207	243480	4095630	5965		x	x	x	x	Figure 12a
AR-0210	224986	4076268	5499	43	x	x			Figure 12b
AR-0212	237835	4085662	5742	43	x	x	x	x	Figure 12a
AR-0217	216573	4075489	5803	339	x	x			Figure 12c
AR-0218	226473	4076865	5500		x	x			Figure 12b
AR-0220	221725	4074714	5450	37	x	x			Figure 12c
AR-0221	220176	4073806	5428		x	x			Figure 12c
AR-0224	227213	4078750	5626	24		x			Figure 12b
AR-0225	230185	4078440	5561		x	x			Figure 12b
AR-0228	238619	4087126	5755			x			Figure 12a
AR-0229	242531	4091734	5857		x	x			Figure 12a
AR-0230	242920	4091425	5856	55		x			Figure 12a
AR-0231	239808	4087752	5767	23	x	x			Figure 12a
AR-0234	218660	4072310	5405	48	x	x			Figure 12c
AR-0235	244333	4100678	5965			x			Figure 12a
AR-0236	243647	4093843	5889		x	x			Figure 12a
AR-0238	240646	4090849	5803		x	x			Figure 12a
AR-0239	241375	4090695	5833		x	x			Figure 12a
AR-0240	223552	4075180	5453		x	x			Figure 12c
AR-0241	234560	4081741	5674		x	x			Figure 12b

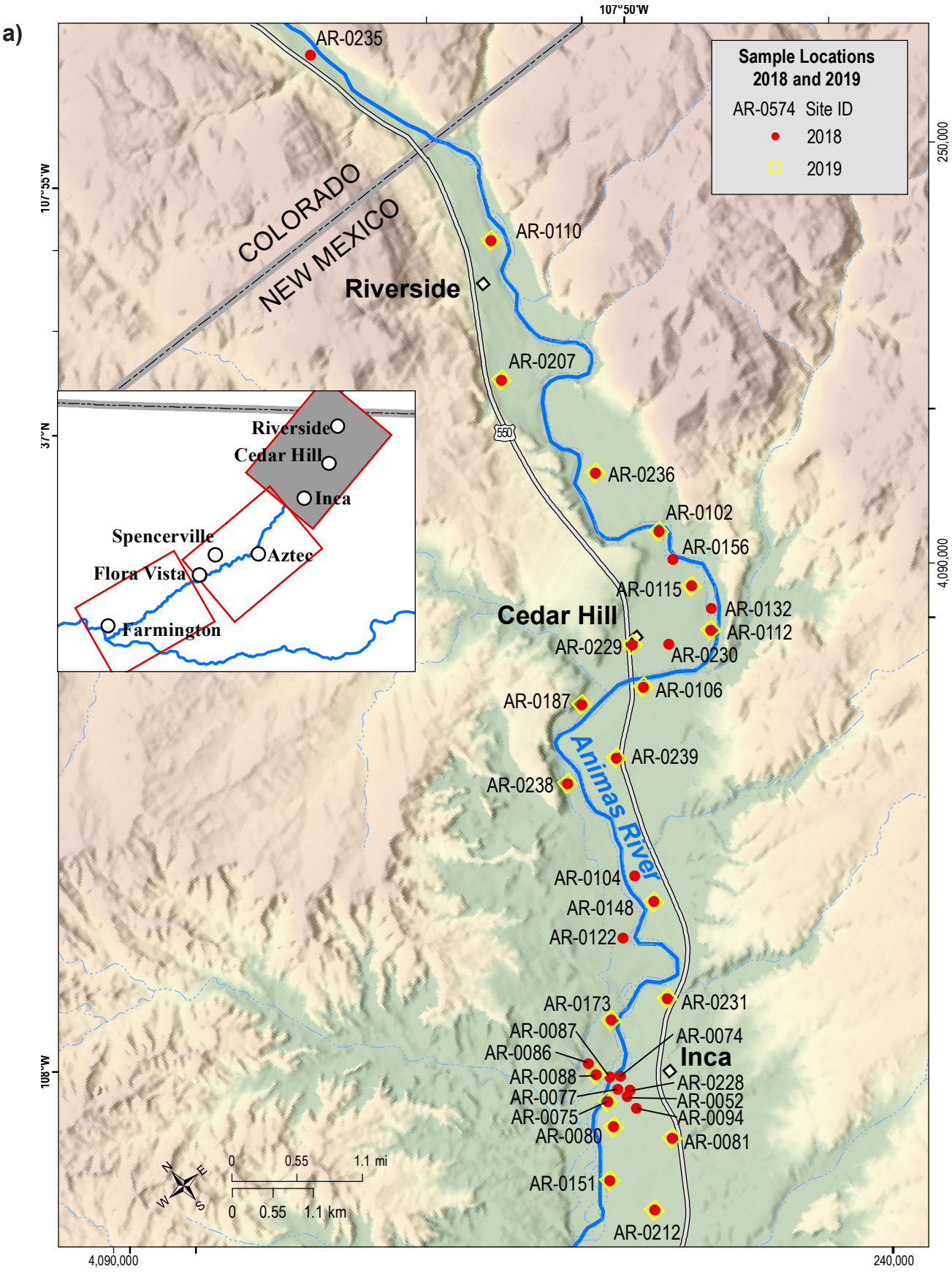

Figure 12a. Well locations for samples collected during the fall 2018 (September and October 2018) and spring 2019 (April 2019).

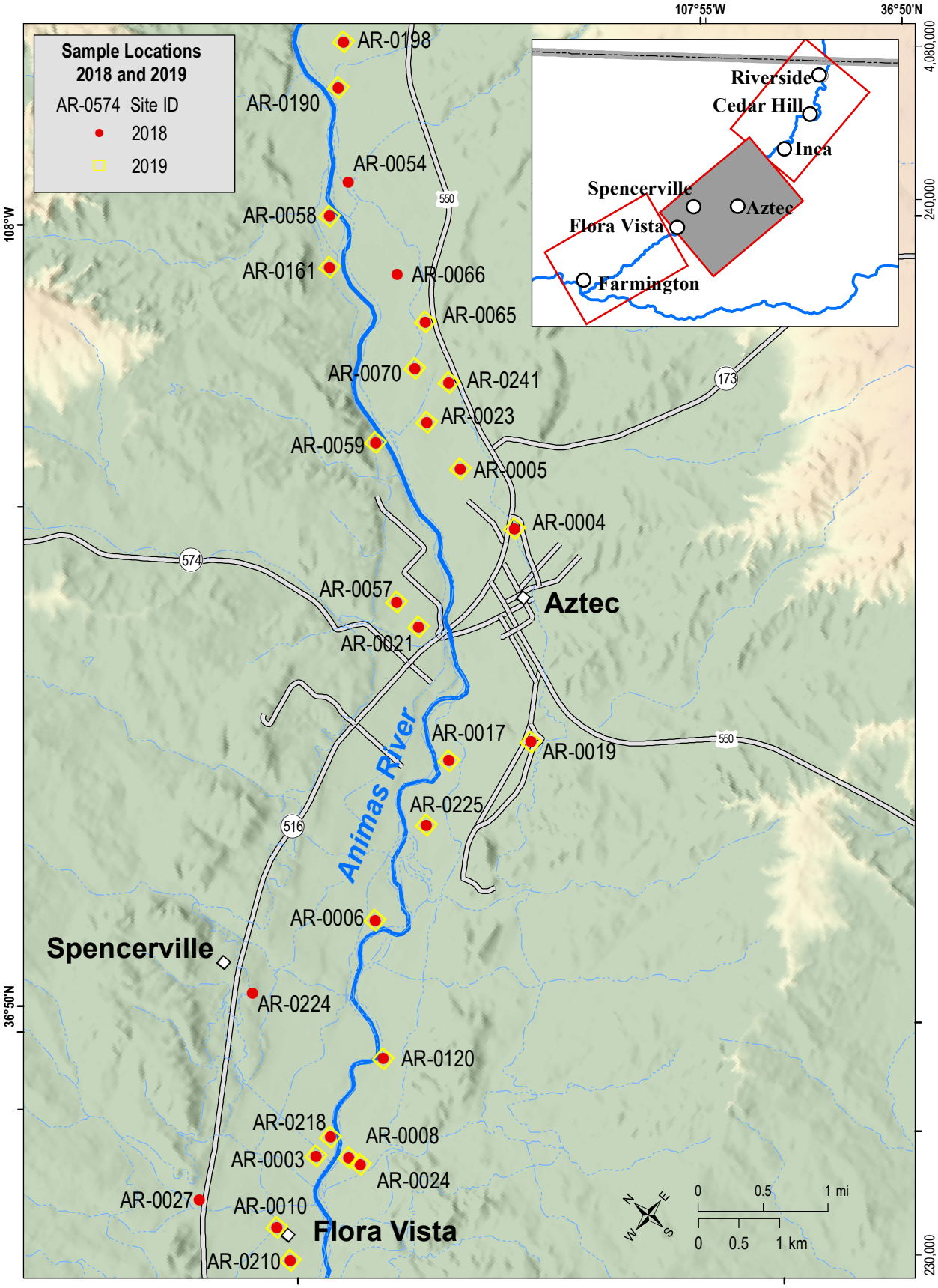

Figure 12b. Well locations for samples collected during the fall 2018 (September and October 2018) and spring 2019 (April 2019).

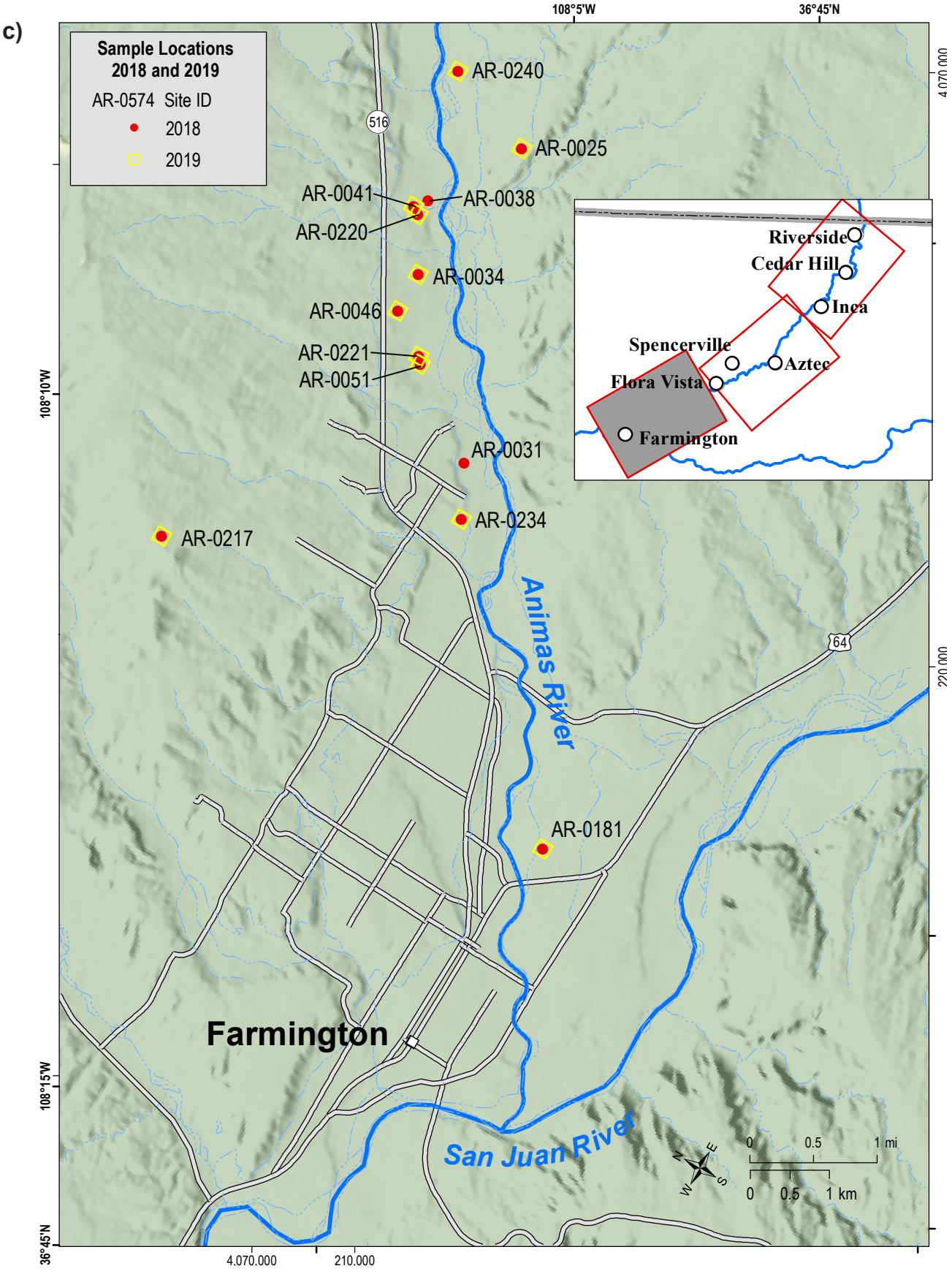

Figure 12c. Well locations for samples collected during the fall 2018 (September and October 2018) and spring 2019 (April 2019).

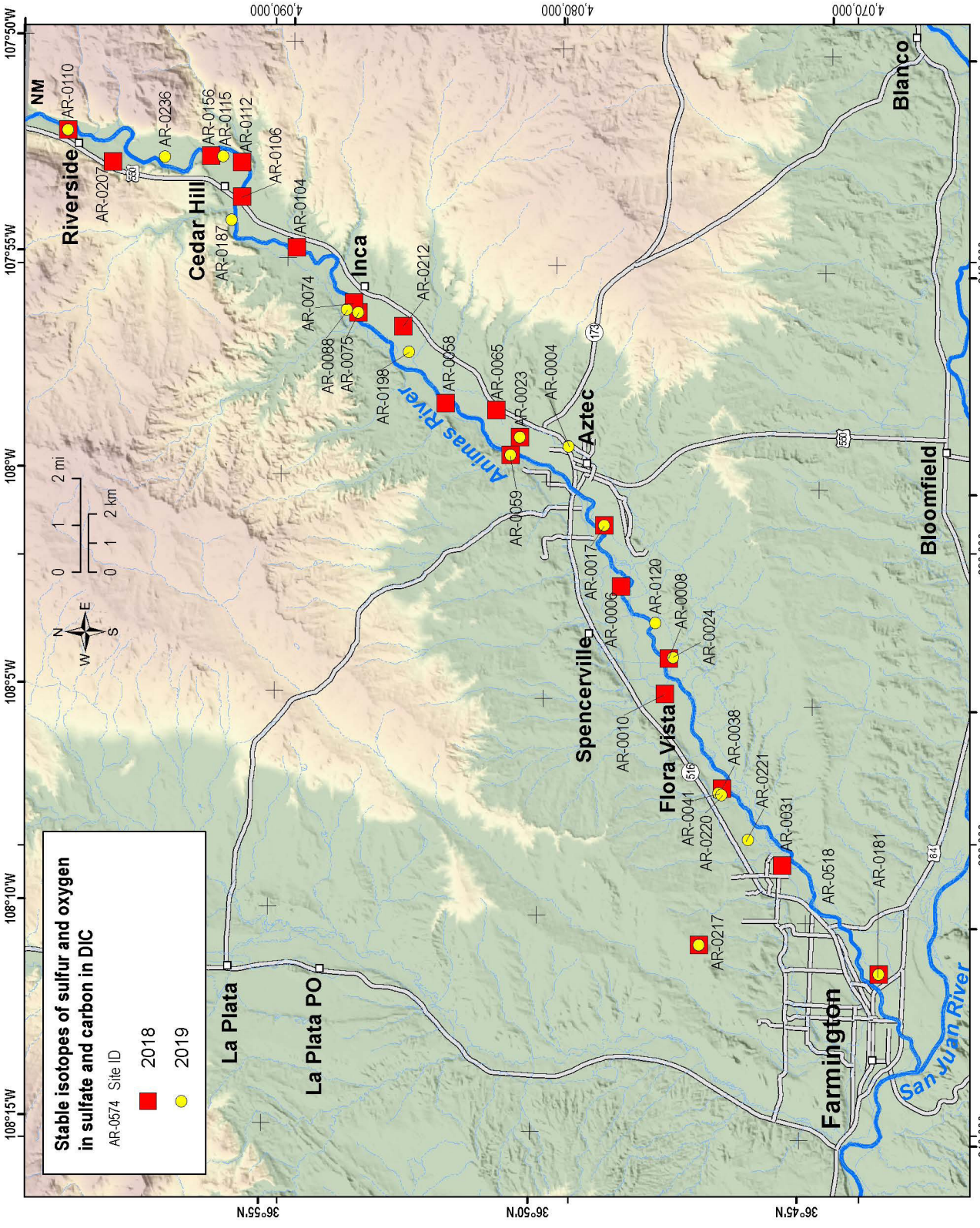

Figure 13. Sample locations for the stable isotopes of sulfur and oxygen in sulfate and carbon in dissolved inorganic carbon. Samples collected in 2019 were not analyzed for oxygen isotopic composition in sulfate due to technical issues.

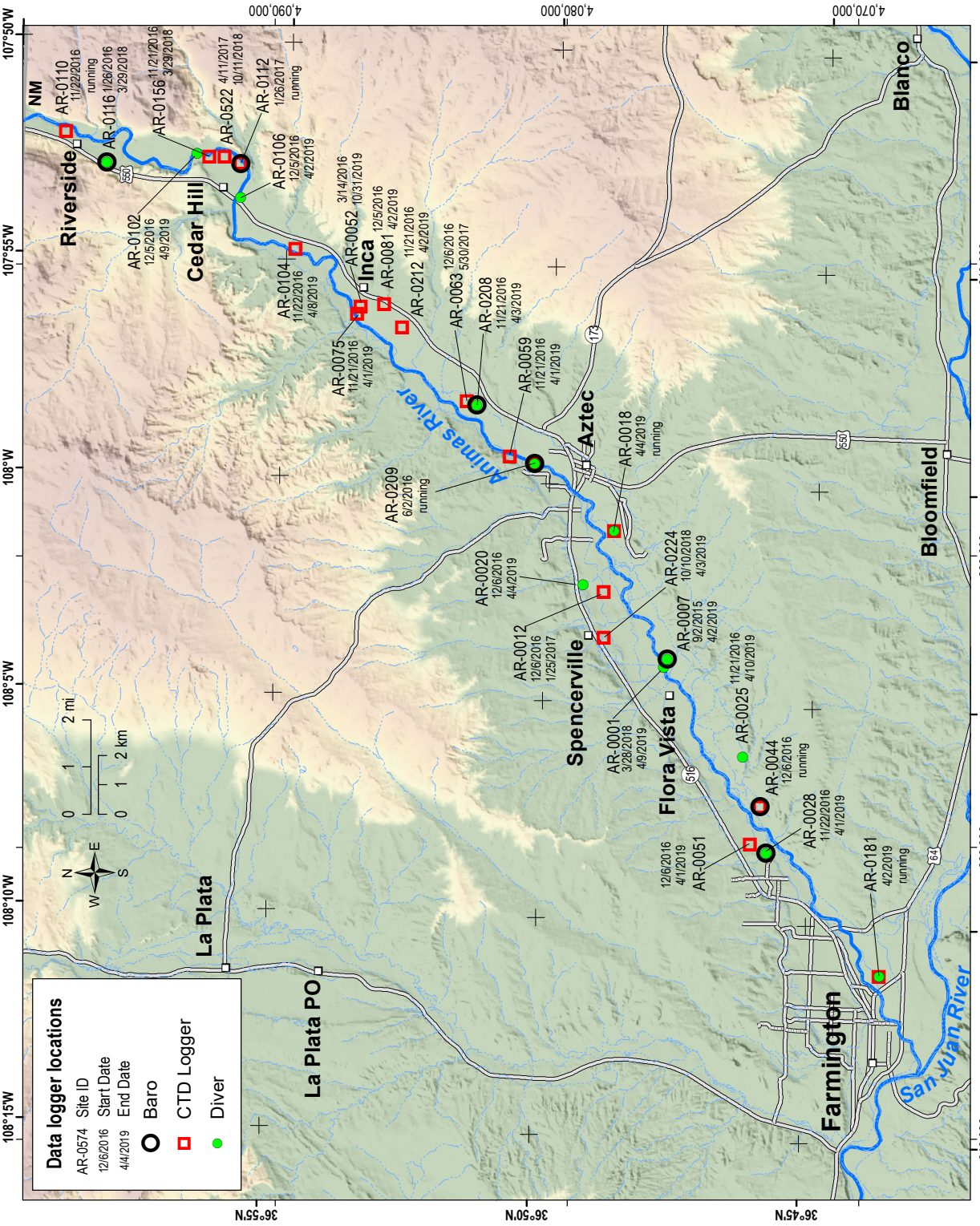

Figure 14. Data logger locations. Divers are installed in the wells and record water level and temperature. CTD Loggers record specific conductance as well as water level and temperature. Baros record barometric pressure, which is used to correct water level data.

saturation indices was done using PHREEQC (Parkhurst, 1995).

Groundwater Levels

When possible, we measured the water level in wells before collecting a sample. Water levels were measured following U.S. Geological Survey protocols for a steel tape measurement device with repeat measurements to within 0.02 feet (Cunningham and Schalk, 2011). If water level measurements were not repeatable within 0.02 feet, notes were made and entered into the database, suggesting that these measurements were of lower data quality. This may happen for various reasons, such as when the well is pumping, recovering, or a nearby site is being pumped. The goal is to obtain a static water level measurement which is confirmed by a repeatable measurement within 0.02 ft. All manual groundwater level measurements are found in Appendix B. Water level data from pressure transducers with data recorders are available from the New Mexico Bureau of Geology and Mineral Resources upon request.

Continuous Data Recorders

We use the term "continuous" to refer to data that were collected at regular time intervals by instruments installed in the field. For this study, most continuous data were collected hourly. Continuous measurements of pressure and temperature were recorded using Van Essen "Divers" and "Baros" to measure and record pressure data in wells and the atmosphere respectively. We processed these data using software provided by Van Essen, which subtracts atmospheric pressure from total pressure measured in the wells and accounts for water temperature to convert pressure readings to water head that is equal to the depth of water above the pressure transducer. These continuous water level data were then adjusted based on manual water level measurements that were done at the time of the download. These adjustments that are based on the difference between the manual water level measurement and the corresponding instrument measurement (recorded at the time closest to that of the manual measurement) were applied to continuous water level data going backward in time, to the previous site download/measurement.

A subset of these data recorders (CTD Divers) measured specific conductance in addition to temperature and pressure. Throughout the duration of this study, the factory calibrated instruments yielded specific conductance measurements within 5% of measurements made independently in the field with instruments that had been recently calibrated against known standards. Therefore the recalibration of the CTD Divers was not necessary. Figure 14 shows locations of the wells where these instruments were installed and the time period for each dataset.

IV. RESULTS

This section presents data collected for this study. Data interpretation is presented in the Discussion section. Manual water level measurements and water chemistry data are provided in Appendix B and Appendix C respectively.

Groundwater Levels

Depth to water data is shown below on Table 2 and Figure 15. With the exception of AR-0217, which is a deep well located outside the river valley, depth to water throughout the Animas Valley is relatively shallow. Depth to water ranged from 0.24 to 53.73 and 2.15 to 56.72 feet bgs for fall, 2018 and spring, 2019 sampling events respectively. For most wells, the water table was observed to be deeper in the spring, 2019 than six months earlier. In general the depth to water decreases with proximity of the river (Figure 15). However in some areas, the depth to water appears to be highly variable among wells in close proximity to each other.

Figure 16 and Figure 17 show hydrographs for wells AR-0116 and AR-0007, which were identified as irrigation-controlled and river stage-controlled wells respectively by Newton et al., (2017). Water level fluctuations in AR-0116 correlate with the timing of irrigation, quickly increasing in response to the initiation of flow in the irrigation ditch and then gradually decreasing after flow in the ditch has stopped. In 2018, decreased water levels in the ditch were observed with no apparent influence on groundwater levels. Water level data for the well AR-0007, which correlate to fluctuations in river stage, showed a slight

Table 2. Depth to water data for fall 2018 and spring 2019 sample events. The calculated difference for wells that were measured for both sampling events is the result of subtracting the 2018 measurement from the 2019 measurement. ft bgs = feet below ground surface, NA = Not Applicable, the water level in the well was not measured. **Water level measurements for well AR-0217, which is located outside the river valley, are not included in the statistics provided below.

DEPTH TO WATER (ft bgs)			
Point ID	Fall 2018	Spring 2019	Difference (ft bgs) Spring 2019 to Fall 2018
AR-0001	6.6	5.19	-1.41
AR-0003	4.31	2.36	-1.95
AR-0004	23.38	31.8	8.42
AR-0005	3.42	8.09	4.67
AR-0006	4.06	3.03	-1.03
AR-0007	12.16	12.57	0.41
AR-0008	11.22	11.55	0.33
AR-0010	13.7	16.65	2.95
AR-0017	1.66	2.2	0.54
AR-0018	0.24	2.68	2.44
AR-0019	32.22	42.16	9.94
AR-0020	23.75	37.14	13.39
AR-0021	34.86	35.88	1.02
AR-0023	4.74	6.23	1.49
AR-0024	12.37	15.24	2.87
AR-0025	23.85	33.71	9.86
AR-0028	14.04	12.6	-1.44
AR-0034	13.76	19.65	5.89
AR-0041	29.44	31.17	1.73

DEPTH TO WATER (ft bgs)			
Point ID	Fall 2018	Spring 2019	Difference (ft bgs) Spring 2019 to Fall 2018
AR-0044	31.45	31.71	0.26
AR-0046	24.2	24.2	0
AR-0051	24.38	25.9	1.52
AR-0052	14.11	24.72	10.61
AR-0057	34.63	37.9	3.27
AR-0059	32.14	33.45	1.31
AR-0065	19.92	32.06	12.14
AR-0066	4.44	2.15	-2.29
AR-0070	10.29	15.42	5.13
AR-0075	5.63	4.9	-0.73
AR-0081	42.22	56.72	14.5
AR-0088	4.44	5.11	0.67
AR-0102	8.44	9.35	0.91
AR-0104	2.53	4.08	1.55
AR-0106	5.72	7.6	1.88
AR-0110	18.12	23.64	5.52
AR-0112	13.53	15.48	1.95
AR-0120	5.62	4.61	-1.01
AR-0148	4.81	7.13	2.32

DEPTH TO WATER (ft bgs)			
Point ID	Fall 2018	Spring 2019	Difference (ft bgs) Spring 2019 to Fall 2018
AR-0151	8.22	13.58	5.36
AR-0161	8.45	9.9	1.45
AR-0173	17	20.2	3.2
AR-0181	11.85	14.72	2.87
AR-0187	8.93	8.23	-0.7
AR-0208	4.83	2.35	-2.48
AR-0209	4.42	3.67	-0.75
AR-0210	9.19	11.32	2.13
AR-0221	19.78	16.79	-2.99
AR-0224	19.92	26.26	6.34
AR-0225	5.98	5.03	-0.95
AR-0229	27.39	32.16	4.77
AR-0231	12.69	14.12	1.43
AR-0234	28.55	29.95	1.4
AR-0238	7.06	10.35	3.29
AR-0239	21.06	28.07	7.01
AR-0241	10.61	9.44	-1.17
AR-0027	37.26	NA	NA
AR-0031	8.25	NA	NA

DEPTH TO WATER (ft bgs)			
Point ID	Fall 2018	Spring 2019	Difference (ft bgs) Spring 2019 to Fall 2018
AR-0038	9.5	NA	NA
AR-0054	8.72	NA	NA
AR-0077	5.21	NA	NA
AR-0080	3.97	NA	NA
AR-0086	17.84	NA	NA
AR-0087	8.64	NA	NA
AR-0092	53.73	NA	NA
AR-0094	14.56	NA	NA
AR-0122	21.04	NA	NA
AR-0156	17.54	NA	NA
AR-0230	37.39	NA	NA
AR-0232	8.82	NA	NA
AR-0240	5.8	NA	NA
**AR-0217	269.31	268.37	-0.94
Maximum	**53.73**	**56.72**	**14.5**
Minimum	**0.24**	**2.15**	**-2.99**
Mean	**15.15**	**17.31**	**2.72**

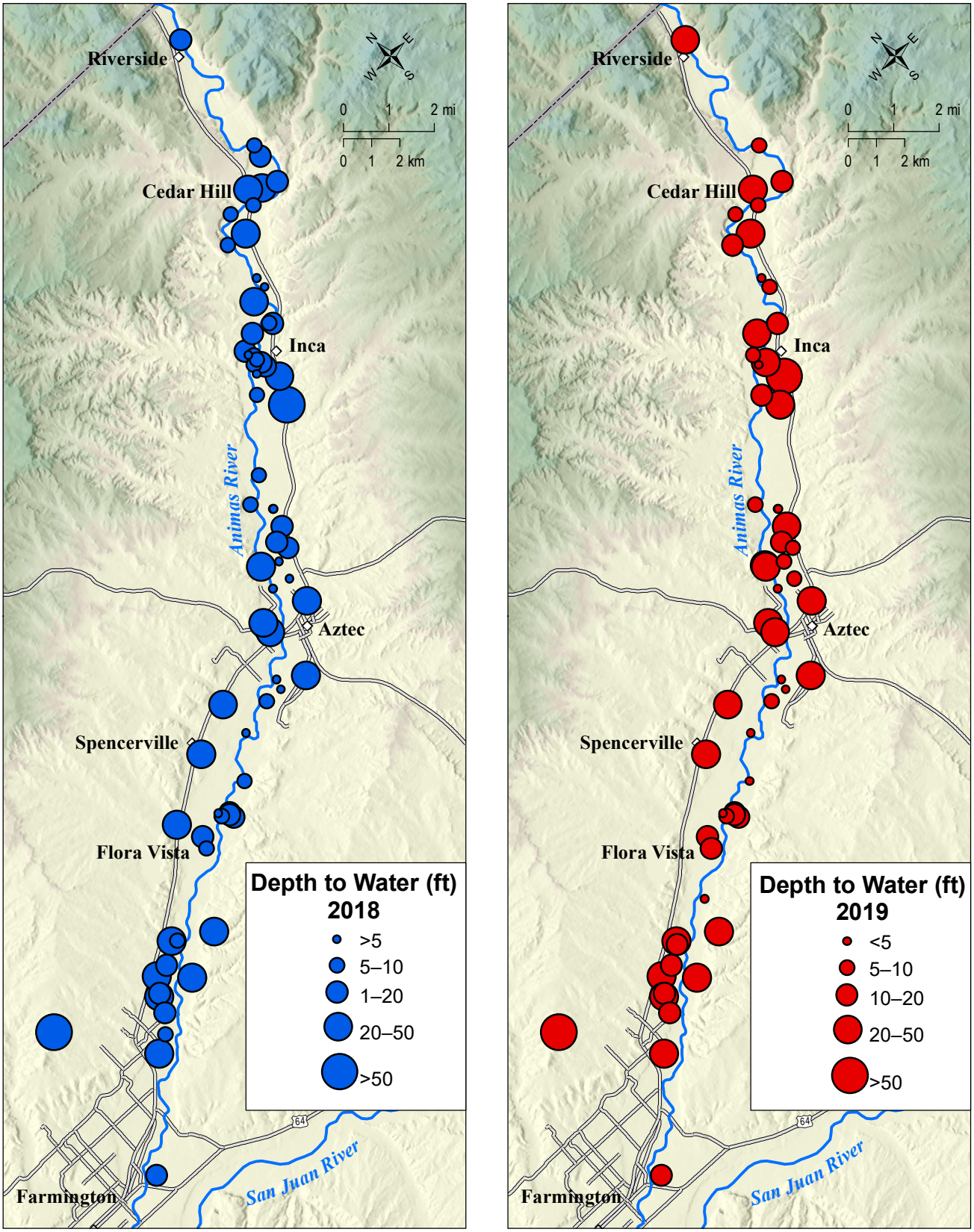

Figure 15. Spatial distribution of depth to water measurements below land surface.

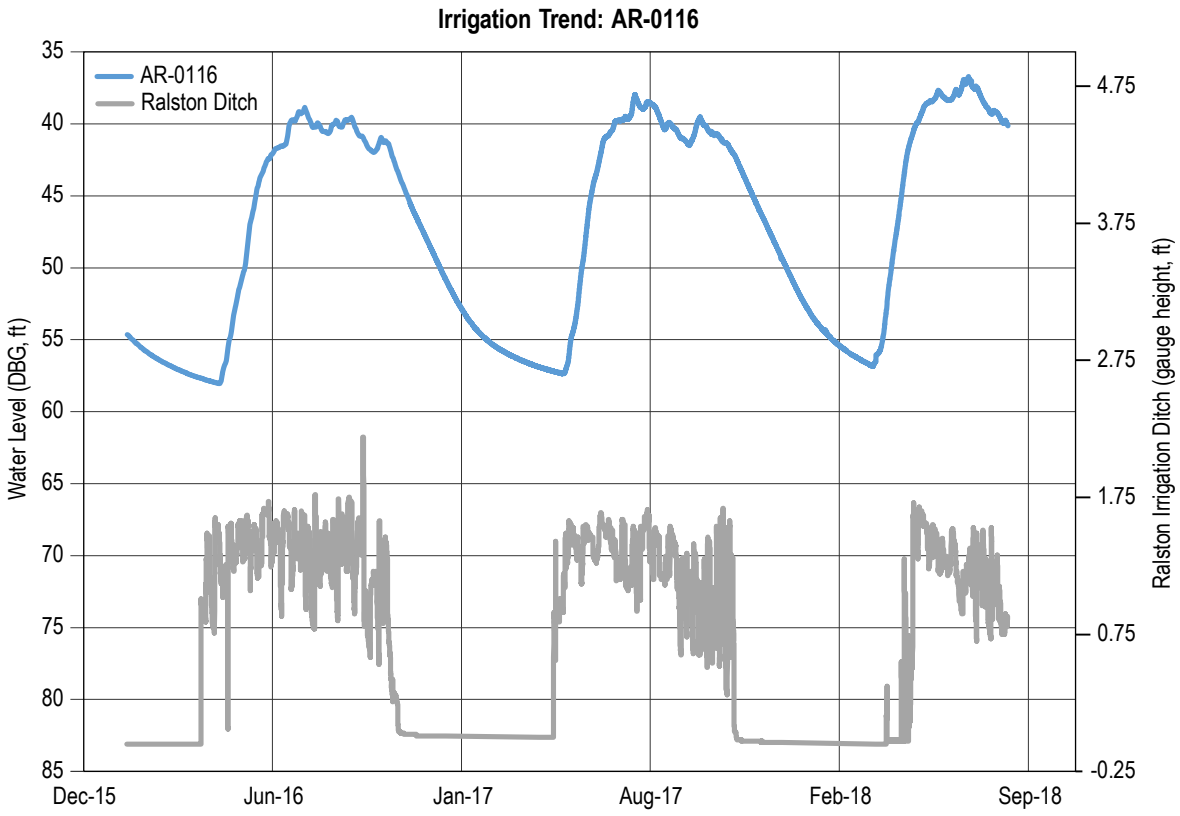

Figure 16. Continuous water level data for AR-0116 (blue line) and irrigation ditch (gray line). Figure 10 shows the location of the ditch.

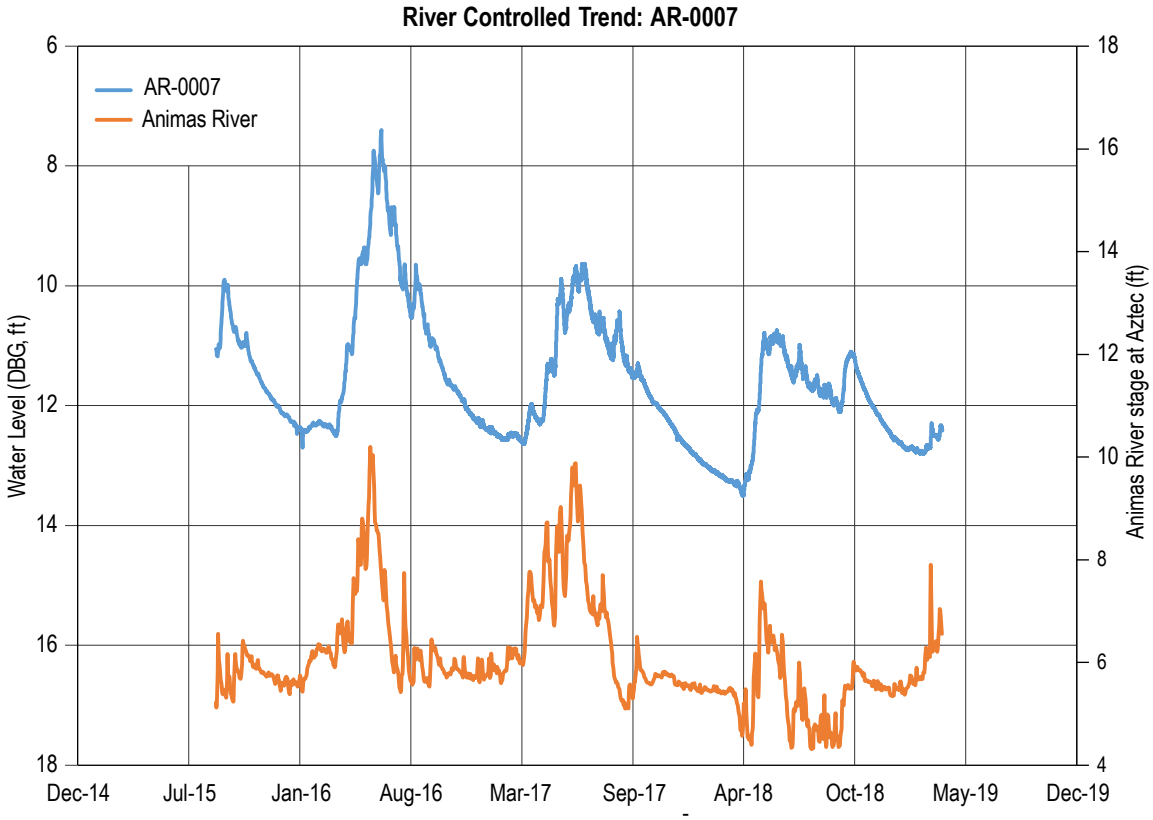

Figure 17. Continuous water level data for AR-0007 (blue line) and Animas River stage (orange line, USGS 09364010).

decrease in 2018 compared to previous years due to extremely low river discharge that year.

Groundwater Chemistry

Major Ion Chemistry

Table 3 and Table 4 show selected chemistry data and statistics for samples collected in the fall of 2018 and the spring of 2019 respectively. The data in these tables include major cations (dissolved and total), major anions, pH, total alkalinity (as CaCO3), dissolved oxygen (DO), and Eh. Figure 18 shows the spatial distribution of sulfate concentrations for samples collected in the fall of 2018 and the spring of 2019. Sulfate concentrations in groundwater increase down gradient, to the south and west, with the highest sulfate concentrations observed south of Aztec. A similar spatial trend was also observed for TDS concentrations (data not shown). An exception to this trend is the well AR-0187, located in the northern portion of the study area near Cedar Hill (Figure 12A). AR-0187 showed the highest sulfate concentrations of 1,630 and 1,160 mg/L for fall, 2018 and spring 2019 respectively. The deep well, AR-0217, produced water with a TDS concentration of 1,520 mg/L, a sulfate concentration of 830 mg/L, and was characterized as a calcium-bicarbonate water type.

Table 3. Major cation concentrations for samples collected in the fall 2018. Unless otherwise indicated, all concentrations are resented as mg/L.

Point ID	Collection Date	Ca	Ca (total)	Mg	Mg (total)	Na	Na (total)	K	K (total)	Cl	HCO_3	SO_4	TDS	ALK	pH	DO	Eh (mV)
AR-0003	9/26/2018	305	310	41.3	42.9	209	215	2.18	2.29	37.7	307	1030	1800	252	7.02	0.1	123.7
AR-0004	9/25/2018	418	427	26.4	26.7	213	217	1.37	1.28	31.5	301	1230	2100	247	6.88	0.15	284.4
AR-0005	9/27/2018	181	192	15.7	16.9	50	56	1.29	1.4	25.5	288	366	799	236	7.11	0.05	176.6
AR-0006	9/25/2018	134	133	15.8	16.2	28.2	28.7	2.05	2.13	22.6	341	139	525	279	6.82	0.11	197.3
AR-0008	9/25/2018	270	268	37.3	37.6	184	184	3.21	3.13	25.7	337	858	1570	277	6.99	1.01	221.9
AR-0010	9/25/2018	194	192	14	14	61.4	61	1.67	1.55	27.6	293	383	859	240	7.01	2.21	258.4
AR-0017	9/25/2018	314	310	19.8	19.9	100	98.3	1.53	1.59	18.4	317	720	1360	260	6.81	0.22	233.9
AR-0019	9/24/2018	578	588	16	16.1	55.9	54	1.18	1.05	13.6	226	1330	2150	186	6.83	1.11	164.3
AR-0021	9/25/2018	198	192	24.3	24.4	67.8	68.1	1.4	1.41	37.2	311	408	915	255	7.03	2.17	236.8
AR-0023	9/26/2018	132	129	15.3	15.5	33.2	33.6	0.79	0.78	24.3	276	181	544	226	7.06	0.15	208.9
AR-0024	9/26/2018	189	188	24.1	24.1	110	110	2.36	2.34	18	285	520	1020	234	7.17	0.45	192.7
AR-0025	10/4/2018	105	106	27.3	27.9	23	23.7	0.68	0.73	23.5	301	151	502	247	6.98	5.96	337.1
AR-0027	9/27/2018	343	338	39.8	39.4	46.2	45.1	4.3	4.11	19.8	290	767	1380	237	6.87	4.83	263.5
AR-0031	9/26/2018	503	489	54.6	55.2	113	111	3.16	3.22	73.4	348	1210	2170	285	6.67	3.39	238.4
AR-0034	10/2/2018	322	328	39.5	40.9	67.4	70.7	2.22	2.34	43.2	349	740	1430	286	6.75	1.6	276.7
AR-0038	9/25/2018	238	238	27.7	27.6	52.1	51.6	2.4	2.34	35.6	367	458	1020	301	6.78	1.35	223.4
AR-0041	10/4/2018	342	344	36.1	36.5	54.2	51.4	2.43	2.64	25.3	371	751	1420	304	6.72	0.42	188.2
AR-0046	10/4/2018	292	296	25.7	26.2	47.8	49.8	2.24	2.48	29.1	348	604	1200	285	6.87	0.33	223.3
AR-0051	10/10/2018	394	404	42.5	42.8	74.2	74.9	2.73	2.75	55.1	365	905	1690	299	6.9	0.05	267.2
AR-0052	10/3/2018	127	128	16.6	17.1	29.4	30.8	1.91	1.99	36.3	297	160	532	243	6.56	1.61	278.6
AR-0054	9/26/2018	149	149	23.8	24	34.4	34.2	1.44	1.46	18.8	429	141	620	351	6.83	0.19	258.3
AR-0057	9/26/2018	110	110	14.2	14.2	42.5	42.1	1.13	1.14	13.8	220	208	516	180	7.29	3.17	254.5
AR-0058	9/27/2018	186	181	18.7	18.4	85	83.5	2.46	2.35	31.1	338	387	895	277	6.85	0.58	228.5
AR-0059	9/27/2018	103	103	13.5	13.3	35.1	36	1.49	1.49	26.1	242	153	469	198	6.92	4.15	231.9
AR-0065	10/3/2018	82.2	79.6	10.3	10.1	18.8	18.7	1.04	1.02	18.1	186	107	342	153	7.24	6.68	286.2
AR-0066	10/2/2018	152	157	32	32	97.4	101	1.43	1.62	23.4	352	402	905	289	7.04	0.43	192.3
AR-0070	9/25/2018	134	129	13.5	13.5	35.9	35.2	1.18	1.17	13.5	320	177	552	263	7.08	1.85	308.3
AR-0074	10/10/2018	128	130	17.9	18.5	37.3	37.3	3.18	3.29	31.4	334	151	551	274	6.95	0.1	178
AR-0075	10/9/2018	166	169	24.1	24.6	107	109	4.41	4.55	126	376	284	930	308	7.23	2.5	112.9
AR-0077	10/2/2018	137	139	18.8	19	30.2	30.6	2.36	2.52	23.9	380	142	569	312	6.98	0.16	231.9
AR-0080	10/3/2018	144	143	20.7	20.8	121	121	2.72	2.87	46.5	323	376	888	265	7.07	0.27	128.9
AR-0081	10/11/2018	115	116	20.5	21	38.5	39.2	1.99	1.99	21.8	328	145	526	269	6.92	5.15	249.9
AR-0086	9/27/2018	120	117	19.9	19.5	47.3	46.2	0.536	0.436	26.9	327	167	564	268	6.97	1.7	206.5
AR-0087	9/26/2018	116	112	20	20.1	63.3	62.7	1.85	1.94	29.7	341	179	596	280	6.95	0.25	170.3
AR-0088	9/27/2018	116	111	26.2	26.2	93.1	93	1.49	1.49	36.5	332	252	715	272	7.04	3.07	230.8
AR-0094	10/3/2018	129	130	18	18.4	21.8	22.4	1.3	1.35	32	306	146	516	251	7.05	5.04	334
AR-0102	10/4/2018	127	127	25.6	26	41.2	42.2	3.24	3.32	37.9	364	164	600	298	6.23	0.96	342.3
AR-0104	10/2/2018	117	110	16.9	15.8	75	89	0.967	1.09	38.8	342	189	625	280	6.45	0.08	206.6
AR-0106	10/9/2018	109	110	16.4	16.7	23.1	23.4	3.06	3.11	24.8	281	124	455	230	7.17	0.06	94.3

Table 3—Continued. Major cation concentrations for samples collected in the fall 2018. All concentrations are presented as mg/L.

Point ID	Collection Date	Ca	Ca (total)	Mg	Mg (total)	Na	Na (total)	K	K (total)	Cl	HCO_3	SO_4	TDS	ALK	pH	DO	Eh (mV)
AR-0110	10/4/2018	107	104	24.8	24.4	51.2	52.5	1.85	2.06	32.8	314	171	559	258	6.38	0.5	149.7
AR-0112	10/1/2018	123	122	17.5	17.5	25.3	25.6	2.02	2.14	30.1	311	130	500	255	6.97	0.12	109.8
AR-0115	10/2/2018	137	136	20.7	21.1	27.8	28.6	2.43	2.54	29.8	351	153	562	287	5.98	5.41	391.4
AR-0120	9/26/2018	218	219	26.9	26.9	105	106	1.54	1.55	30.8	352	559	1140	289	6.99	1.12	305.1
AR-0122	10/3/2018	129	126	20.7	21.2	28.3	29.2	1.07	1.12	22.2	371	126	538	304	6.63	5.17	388.7
AR-0132	10/1/2018	126	124	17.3	17.5	28.4	28.6	2.7	2.77	32.9	301	151	521	247	6.9	0.44	181
AR-0148	10/9/2018	159	161	20.5	20.8	47.9	48.3	1.1	1.11	22.6	370	238	694	304	7.06	0.07	129.6
AR-0151	10/3/2018	138	137	19.4	19.9	22.9	23.4	2.02	2.13	27.1	352	139	540	289	6.86	1	233
AR-0156	10/2/2018	134	133	26.4	26.8	37.8	40.3	3.91	4.05	34.3	367	175	612	301	5.98	2.65	366
AR-0161	9/27/2018	150	147	16	15.9	91.4	90.3	2.28	2.33	36.9	294	328	786	241	6.97	0.36	212.5
AR-0173	10/3/2018	122	121	25.8	25.8	65	66.9	1.16	1.31	26.3	333	199	664	273	6.01	5.41	307.5
AR-0181	9/26/2018	164	164	26.9	26.9	39.4	39.9	2.84	2.85	32.1	364	246	711	298	6.73	0.75	256.5
AR-0187	10/2/2018	289	285	65	65	570	575	2.18	2.02	156	345	1630	2900	283	6.69	0.07	121.9
AR-0190	10/2/2018	115	109	15.9	15.6	23.1	22.9	1.6	1.6	22.8	272	126	465	223	7.01	5.99	316.8
AR-0198	10/2/2018	122	119	15.4	15.5	19.7	20.2	1.19	1.21	24.9	280	130	480	230	7.24	5.93	371.8
AR-0207	10/4/2018	119	113	21.1	20.6	26	25.8	1.84	1.82	25.8	311	135	502	255	6.66	5.24	864.1
AR-0210	9/27/2018	142	141	9.59	9.71	34.3	35.1	1.66	1.67	21	317	166	560	260	6.99	0.53	292.3
AR-0212	10/10/2018	117	118	16.1	16.5	16.9	17.2	0.928	0.969	19.5	298	114	448	244	7.13	5.1	318.7
AR-0217	10/1/2018	360	358	36.8	35.9	57.6	60.9	2.25	2.42	8.56	364	830	1520	299	6.71	0.29	172.2
AR-0218	9/27/2018	417	405	66.2	67.6	365	357	3.61	3.69	85.6	335	1590	2740	274	6.89	1.01	303.4
AR-0220	10/4/2018	309	304	34.8	36.1	49.7	52.2	2.15	2.25	28.1	360	659	1290	295	6.86	0.15	335.1
AR-0221	9/25/2018	258	255	30.5	30.5	59.2	59.2	1.95	1.96	49.6	333	537	1140	273	6.96	0.53	302.3
AR-0224	9/25/2018	128	124	14.3	14.1	39.7	39.2	1.16	1.16	23.9	244	212	560	200	7.25	4.89	282.3
AR-0225	9/26/2018	167	165	13	13	62.8	62.5	1.7	1.72	16.3	310	307	755	254	7.12	2.37	292.7
AR-0228	10/3/2018	129	128	17	17.4	27.4	28.6	1.94	2.05	34.7	291	158	531	239	6.57	2.93	338.3
AR-0229	10/2/2018	111	107	17.7	17.4	25	24.7	1.9	1.89	22.3	291	121	459	239	5.96	7.47	446.3
AR-0230	10/3/2018	129	127	19.3	20.1	23.4	24.8	2.4	2.57	28.4	320	144	521	263	6.6	5.04	351.2
AR-0231	10/9/2018	50.6	51.7	7.97	8.22	88.3	90	1.16	1.2	26.3	214	139	432	175	7.49	0.6	55.9
AR-0234	9/25/2018	437	427	26.2	26.2	164	162	3.58	3.55	74.1	267	1140	2010	219	7.2	5.88	116.3
AR-0235	10/4/2018	113	112	18.2	18.8	38.1	40	2.32	2.4	40.7	275	158	523	225	6.17	0.09	388.5
AR-0236	10/4/2018	150	145	26.3	26.8	25.7	27.8	8.9	8.85	27.4	424	153	623	348	6.2	4.8	424.2
AR-0238	10/3/2018	104	101	12.4	12.3	47.3	47.3	2.06	2.08	25.8	238	174	495	195	6.63	0.05	200.6
AR-0239	10/4/2018	160	162	22.9	23.5	26.3	27.9	2.03	2.14	29.3	421	151	628	345	6.9	5.01	351.3
AR-0240	9/27/2018	297	291	50.2	48.9	98	95.7	3.71	3.46	36.5	364	773	1460	298	6.73	0.4	276.6
AR-0241	9/25/2018	120	119	14.1	13.7	24.6	23.1	1.93	2.22	23.7	296	129	482	242	7.01	3.02	281.5
Minimum		**50.6**	**51.7**	**7.97**	**8.22**	**16.9**	**17.2**	**0.536**	**0.436**	**8.56**	**186**	**107**	**342**	**153**	**5.96**	**0.05**	**55.9**
Maximum		**578**	**588**	**66.2**	**67.6**	**570**	**575**	**8.9**	**8.85**	**156**	**429**	**1630**	**2900**	**351**	**7.49**	**7.47**	**864.1**
Mean		**190.13**	**188.96**	**23.85**	**24.03**	**69.60**	**70.27**	**2.13**	**2.17**	**33.16**	**320.12**	**393.19**	**894.20**	**262.45**	**6.84**	**2.08**	**257.79**

The Piper diagram shown in Figure 19, which shows all data for samples collected for this study, exhibits a linear trend for major anions that shows that most groundwater sampled can be characterized with the dominant anion being bicarbonate or sulfate. All water samples had low relative chloride concentrations (<25% as a proportion of total anions in meq/L). For cations, most samples plot in a cluster with calcium as the dominant cation with a few samples exhibiting higher relative concentrations of sodium. Most water samples can be categorized as calcium-bicarbonate and calcium-sulfate water types.

Figure 20 shows total dissolved solids concentrations as a function of relative sulfate concentrations (as a proportion of total anions in milliequivalents per liter). We observed a rough exponential relationship with total dissolved solids increasing as sulfate becomes the dominant anion. Alkalinity and pH were examined because these parameters often affect concentrations of dissolved constituents. A rough inverse relationship between alkalinity and pH was observed (Figure 21), and the majority of pH values measured during the fall of 2018 were lower than those measured in the spring of 2019 (Figure 22). The six wells that exhibit the lowest pH values measured for the 2018 sampling event, which include AR-0229, AR-0115, AR-0173, AR-0236, AR-0102, and AR-0110, are all located in the northern portion of the study area (Figure 12A).

Table 4. Major cation concentrations for samples collected in the spring 2019. All concentrations are presented as mg/L.

Point ID	Collection Date	Ca	Ca (total)	Mg	Mg (total)	Na	Na (total)	K	K (total)	Cl	HCO_3	SO_4	TDS	ALK	pH	DO	Eh (mV)
AR-0003	4/9/2019	373	366	53.8	53.1	241	238	2.16	1.89	72	319	1240	2160	261	7.13	1.95	160.8
AR-0004	4/2/2019	425	401	27	26.1	202	195	1.14	1.1	29.1	297	1230	2100	243	6.92	0.12	202.4
AR-0005	4/4/2019	203	193	18.2	17.5	98.3	96.4	1.32	1.22	26	320	438	961	262	7.02	1.99	389.7
AR-0006	4/2/2019	149	148	18.7	18.7	29.5	29.7	2.17	2.15	21.4	377	170	593	309	7.02	0.23	153
AR-0008	4/2/2019	233	227	32.2	31.6	172	171	2.79	2.79	25	329	738	1390	270	7.13	1.23	210.4
AR-0010	4/10/2019	216	217	16	15.9	59.1	58.9	1.74	1.38	28.3	284	428	925	233	7.07	2.25	352.8
AR-0017	4/4/2019	302	300	20.1	20.2	82.3	83.5	1.35	1.36	20.2	320	688	1300	262	7.06	0.1	202.6
AR-0019	4/4/2019	592	560	16.4	16	56.4	54.6	1.11	1.08	18.8	146	1380	2190	119	6.99	1.07	220.1
AR-0021	4/4/2019	172	167	22.5	22.3	63.6	62.3	1.29	1.31	32.4	289	341	799	237	7.02	1.78	208.6
AR-0023	4/8/2019	126	130	14.5	15.5	31.6	33.6	0.735	0.756	26.2	270	193	545	221	7.24	0.04	221.4
AR-0024	4/8/2019	168	169	22.5	22.5	95.1	95.2	2.3	1.84	24.6	288	426	899	236	7.25	0.15	170.8
AR-0025	4/10/2019	117	116	31.2	31.9	31	32.1	1.65	1.65	25.9	300	201	583	246	6.93	4.06	348.9
AR-0034	4/10/2019	267	272	35.3	34.9	65.6	63.7	2.18	1.78	40.2	335	619	1240	275	6.8	1	332.8
AR-0041	4/9/2019	230	235	37.7	38.2	98.4	97.1	2.8	2.32	27.3	362	612	1210	297	6.84	0.25	272.5
AR-0046	4/8/2019	363	364	32.3	32	53.5	52.3	2.74	2.23	30.4	355	811	1500	291	6.83	0.2	231.4
AR-0046	4/8/2019	361	363	32.2	32.2	53.1	52.8	2.75	2.2	30.2	354	808	1490	290	6.84	0.11	229.4
AR-0051	4/1/2019	306	299	31.2	30.5	64.6	63.7	2.22	2.28	49.8	345	645	1310	283	6.85	0.8	209.2
AR-0057	4/4/2019	117	117	15.5	15.7	52.5	52.5	1.25	1.27	17.3	231	226	561	189	7.34	4.1	187.3
AR-0058	4/4/2019	165	164	16.5	16.6	67.4	66.9	1.92	1.91	31.3	343	273	742	281	7.05	3.92	239.1
AR-0059	4/1/2019	140	136	18.1	18.5	95.9	116	2.3	2.2	35.4	290	307	759	238	7.2	0.38	250
AR-0065	4/3/2019	174	173	23.1	23.6	35.1	35.5	1.44	1.3	23.1	232	353	741	190	7.25	3.3	300.8
AR-0070	4/3/2019	142	140	14.5	14.4	42.5	42.1	1.21	1.19	16.7	305	204	590	250	7.1	2.47	272.8
AR-0075	4/1/2019	132	129	19.6	19.1	80.8	79.9	3.13	3.07	59.9	345	223	717	283	7.41	4.21	117
AR-0080	4/3/2019	154	158	23.4	22.9	88.7	158	2.36	2.42	62.7	321	320	827	263	7.17	5.02	168
AR-0081	4/2/2019	129	129	23.2	23.4	42	41.8	2.07	2.1	27.9	325	166	576	267	6.96	4.75	242.8
AR-0088	4/10/2019	99.5	106	22.2	24.4	78.3	86.3	1.15	1.25	33.3	321	218	637	263	7.24	2.94	302.5
AR-0102	4/9/2019	133	135	27.2	28.4	42.8	44.6	3.32	3.43	38.5	362	174	618	297	7.01	0.3	326.1
AR-0106	4/3/2019	118	118	18.3	18.3	24.4	24.5	2.81	2.82	32.9	274	137	483	224	7.3	0.07	159.1
AR-0110	4/9/2019	136	137	31	32.4	78	69.4	2.31	2.3	57.1	319	254	758	261	7.12	4.71	268.6
AR-0112	4/9/2019	97.9	97.9	14.6	14.8	29.2	30	1.78	1.78	29	222	139	436	182	7.43	1.18	91.3
AR-0115	4/10/2019	129	133	20.8	21.1	31.8	32.4	2.61	2.64	29.2	332	148	543	272	7.29	6.38	262.3
AR-0120	4/8/2019	216	212	27.5	26	82.5	77.3	1.43	0.912	26.3	305	497	1020	250	7	1.44	380.6
AR-0148	4/2/2019	173	174	21.7	21.9	100	98.7	1.03	1.04	61.3	354	327	880	290	6.95	0.06	130.5
AR-0151	4/2/2019	145	140	22	23.1	25.9	26.9	2	2.11	32.9	343	157	569	281	7.02	3.12	212.5
AR-0161	4/4/2019	175	171	19.6	19	90.5	88.3	2.2	2.27	42.1	297	376	868	243	7.13	0.08	245.1
AR-0173	4/10/2019	119	117	24.6	24.8	62.8	63.6	1.3	1.3	36.8	310	194	627	254	7.25	6.4	238.6
AR-0181	4/2/2019	161	158	25.8	25.5	46.2	46.5	2.87	2.86	29.7	359	250	710	294	7.09	2.88	383.6
AR-0187	4/4/2019	208	202	47.6	45.8	446	436	1.97	1.9	128	334	1160	2180	274	7.32	0.05	98.5
AR-0190	4/3/2019	107	105	15.5	15.2	22	21.7	1.6	1.56	22.6	241	113	433	198	7.08	3.86	353.4
AR-0198	4/2/2019	117	120	14.7	15.4	22.2	22.7	1.12	1.19	23.2	286	130	472	234	7.08	2.43	369.2
AR-0207	4/9/2019	145	146	26.7	27.4	30.7	31.9	2.05	2.12	37.5	364	169	613	298	7.09	3.04	672
AR-0210	4/10/2019	153	150	10.3	10.4	35.6	35.4	1.67	1.23	17.4	314	203	599	257	6.94	0.96	281.8
AR-0212	4/3/2019	127	129	17.9	18	21.6	21.8	1.05	1.07	21.5	327	119	487	268	7.21	0.77	298
AR-0217	4/1/2019	360	352	36.8	36.7	59.5	57.8	2.23	2.27	8.41	356	824	1510	292	6.79	0.17	320.7
AR-0218	4/9/2019	348	338	60	59.5	389	388	3.08	2.51	67.4	343	1470	2550	281	7.2	0.98	280.2
AR-0220	4/10/2019	242	235	28.9	28.4	50.9	50.4	1.93	1.37	31	357	466	1020	292	6.85	0.09	247.3
AR-0221	4/9/2019	255	251	30.4	29.7	59.3	58.6	1.96	1.57	47	325	536	1120	267	6.96	0.18	221
AR-0225	4/4/2019	172	171	13.5	13.8	58.4	59	1.5	1.35	18.5	304	312	760	249	7.1	5.62	269.9
AR-0229	4/3/2019	122	122	22.1	22	36.5	36.5	2.78	2.79	30.3	299	116	541	245	7.37	6.99	325.8
AR-0231	4/2/2019	121	118	19.1	19.4	165	161	1.7	1.65	63.9	223	418	915	183	7.21	0.03	155.5
AR-0234	4/2/2019	409	400	26.5	26.1	148	145	3.43	3.47	82.6	195	1080	1870	160	7.34	7.74	99
AR-0236	4/9/2019	131	126	24.6	24	23.3	23.2	8.6	8.39	28.9	340	133	557	279	7.14	6.52	416.3
AR-0238	4/9/2019	120	117	14.4	14.6	43	43	2.11	2.15	31.6	277	167	527	227	7.31	2.34	169.6
AR-0239	4/3/2019	156	158	23.1	23.9	38.4	39.1	2.32	2.17	70	371	152	649	304	7.06	6	257.4
AR-0240	4/10/2019	325	315	54.7	53.4	89.6	88.8	3.44	3.2	36.6	357	843	1550	293	6.8	0.31	250.6
AR-0241	4/3/2019	137	142	15.2	16	39.3	41.4	1.63	1.7	21	325	179	582	266	7.17	2.51	270.5
Minimum		**97.9**	**97.9**	**10.3**	**10.4**	**21.6**	**21.7**	**0.735**	**0.756**	**8.41**	**146**	**113**	**433**	**119**	**6.79**	**0.03**	**91.3**
Maximum		**592**	**560**	**60**	**59.5**	**446**	**436**	**8.6**	**8.39**	**128**	**377**	**1470**	**2550**	**309**	**7.43**	**7.74**	**672**
Mean		**200.24**	**197.66**	**24.88**	**24.87**	**79.87**	**80.76**	**2.13**	**2.02**	**36.40**	**311.04**	**437.52**	**960.57**	**254.89**	**7.09**	**2.24**	**254.50**

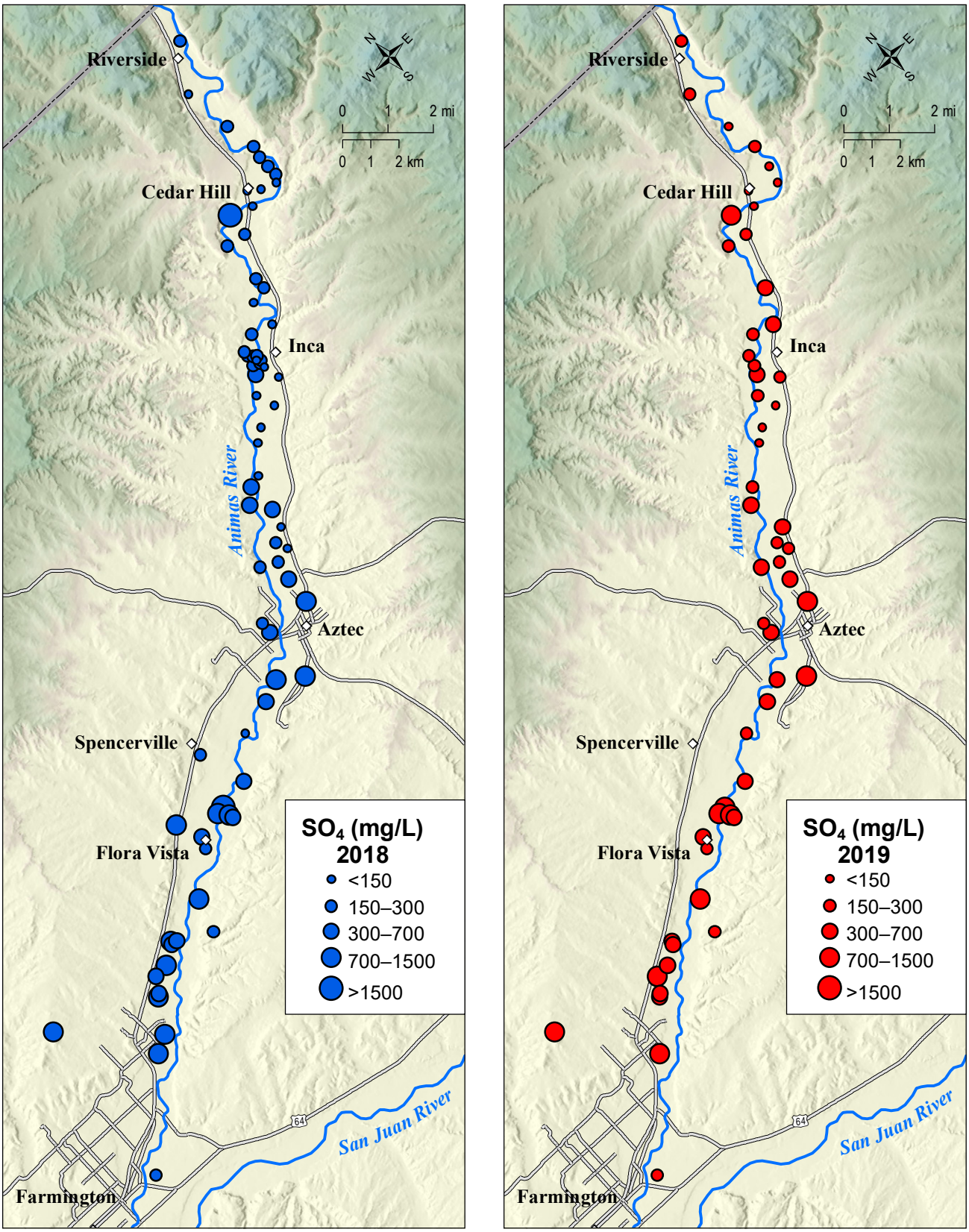

Figure 18. Spatial distribution of sulfate concentrations for samples collected in September/October 2018 (left) and April 2019 (right).

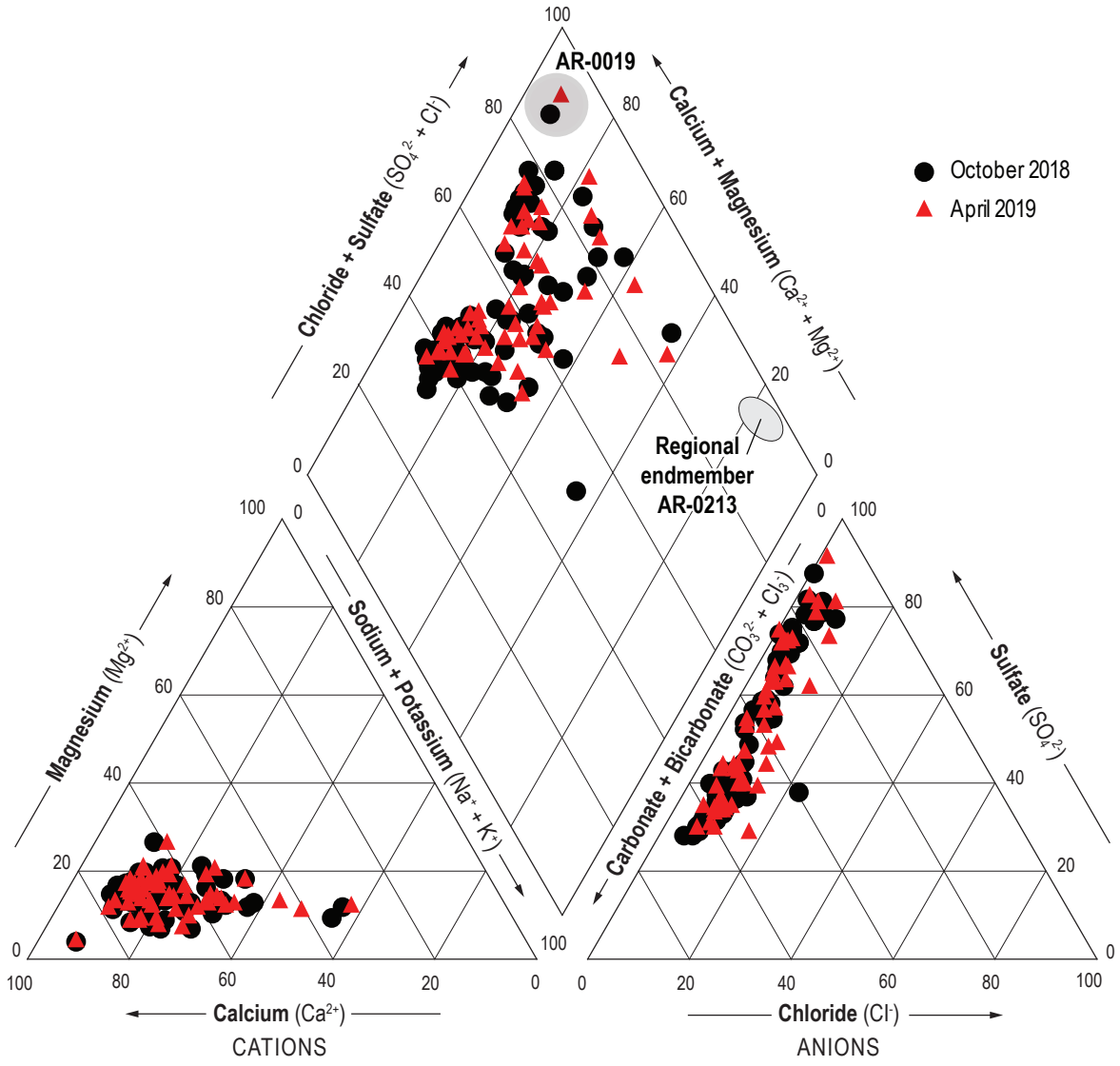

Figure 19. Piper diagram showing relative cation and anion relationships for groundwater collected in the fall 2018 and spring 2019. The chemical signature for the very brackish sodium sulfate endmember (represented by AR-0213, Newton et al., 2017) is shown by the grey oval. The well AR-0019 is also highlighted, as it will be discussed below.

Dissolved Oxygen

Figure 24 shows the spatial distribution of dissolved oxygen concentrations in wells during the fall of 2018 and the spring of 2019. We observed a large range in dissolved oxygen concentrations for each sampling event. Comparing dissolved oxygen measurements in wells sampled in both 2018 and 2019 show that concentrations can vary quite a lot over time (Figure 23). In some wells, dissolved oxygen values measured at the different times were nearly identical, while in other wells dissolved oxygen concentrations changed significantly between sampling events. Interestingly, Dissolved oxygen concentrations appear to be generally lower south of Aztec.

Trace metals and redox conditions

We analyzed water samples for the following trace metals: silver (Ag), aluminum (Al), arsenic (As), boron (B), barium (Ba), beryllium (Be), cadmium (Cd), cobalt (Co), chromium (Cr), copper (Cu), iron (Fe), mercury (Hg), lithium (Li), manganese (Mn), molybdenum (Mo), nickel (Ni), lead (Pb), antimony (Sb), selenium (Se), tin (Sn), strontium (Sr), thorium (Th), titanium (Ti), uranium (U), vanadium (V), and zinc (Zn). For most of these metals, analysis results were below the reporting limit for nearly all the samples. All water samples exhibited concentrations below the maximum contaminant levels (MCLs) as defined by the EPA National Primary Drinking Water Regulations that

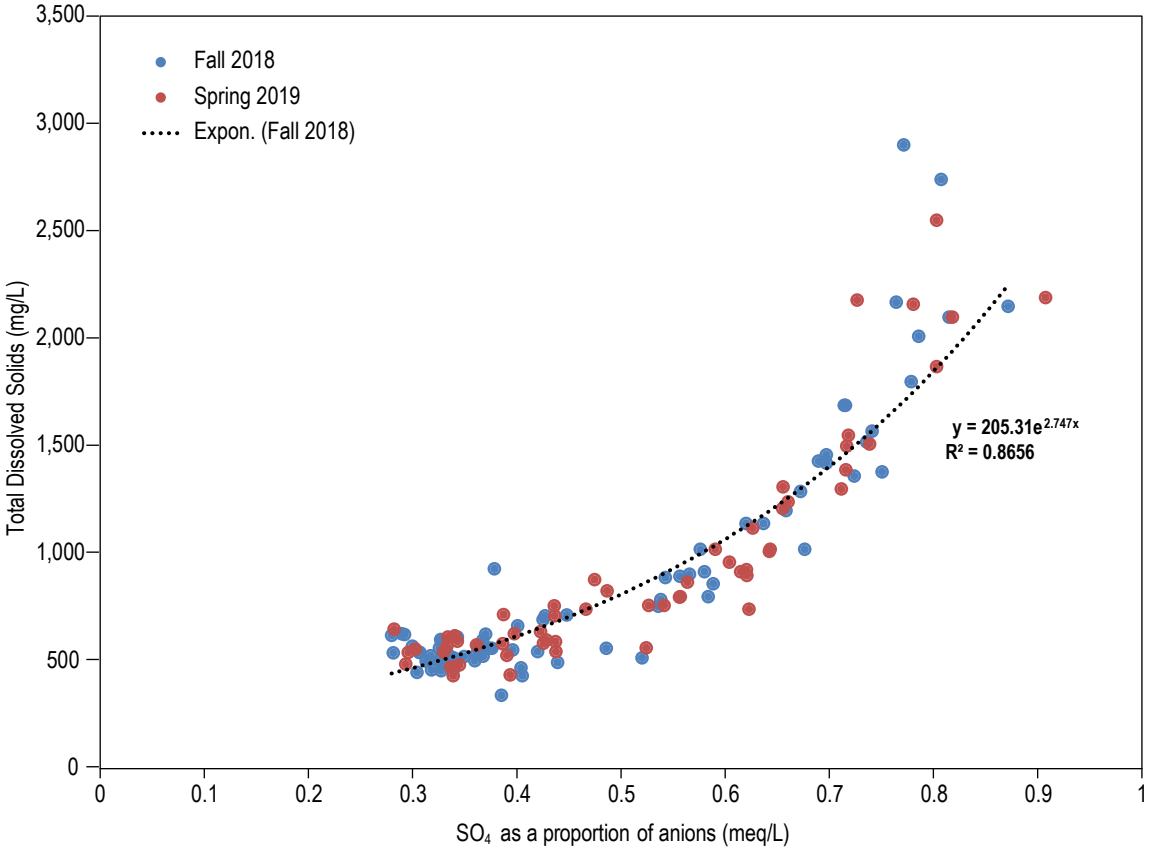

Figure 20. Total dissolved solids concentrations plotted as a function of sulfate concentrations.

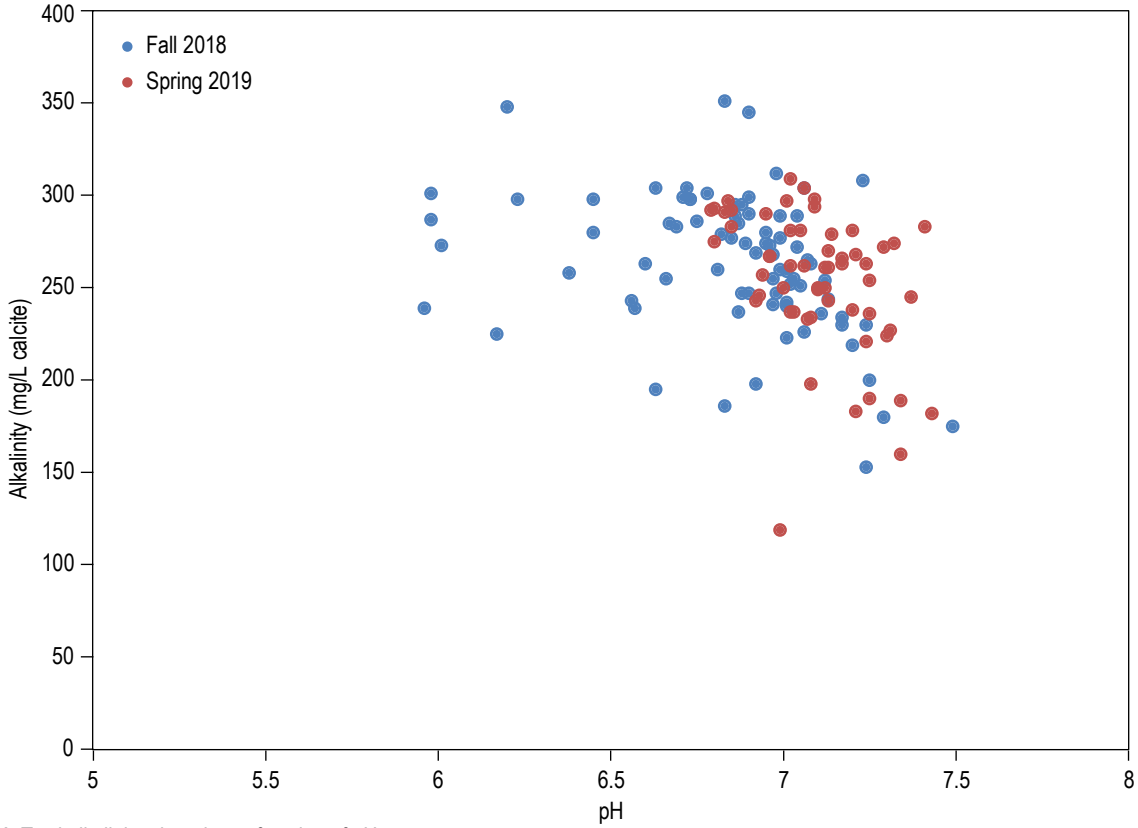

Figure 21. Total alkalinity plotted as a function of pH.

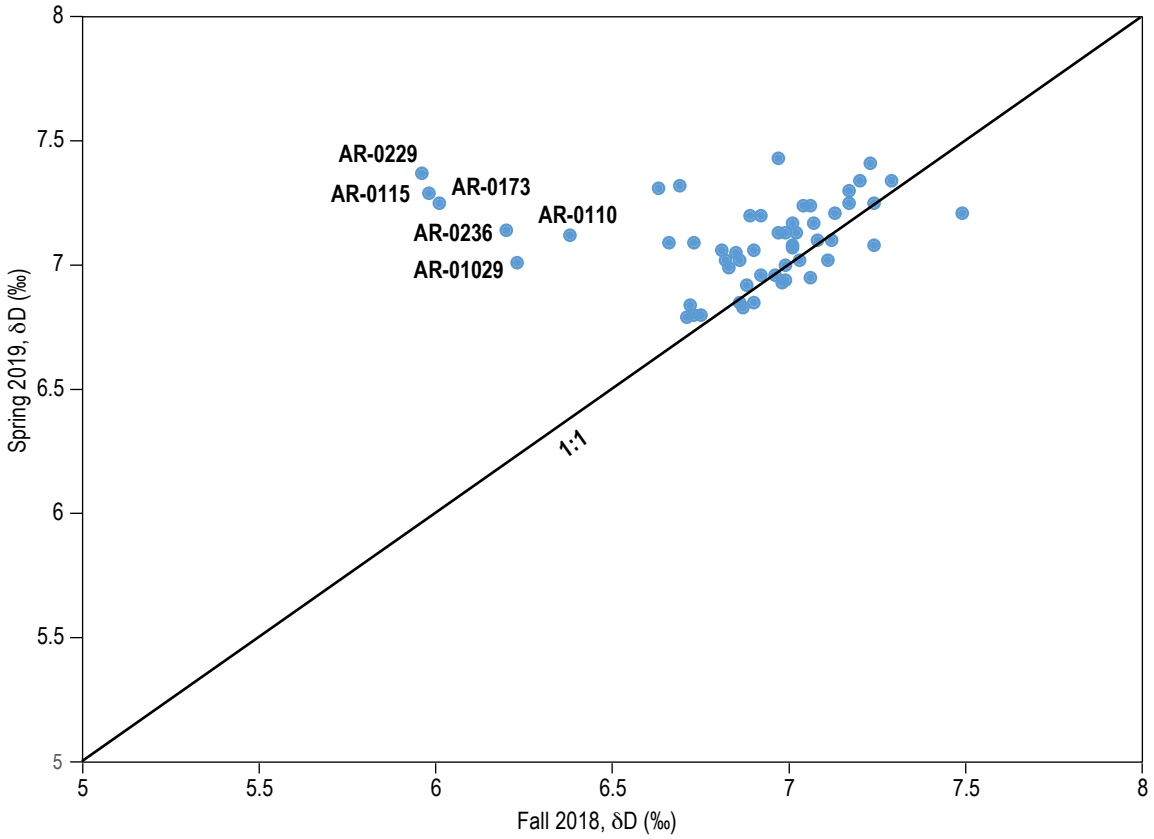

Figure 22. Comparison of pH values for samples collected from the same wells in 2018 and 2019.

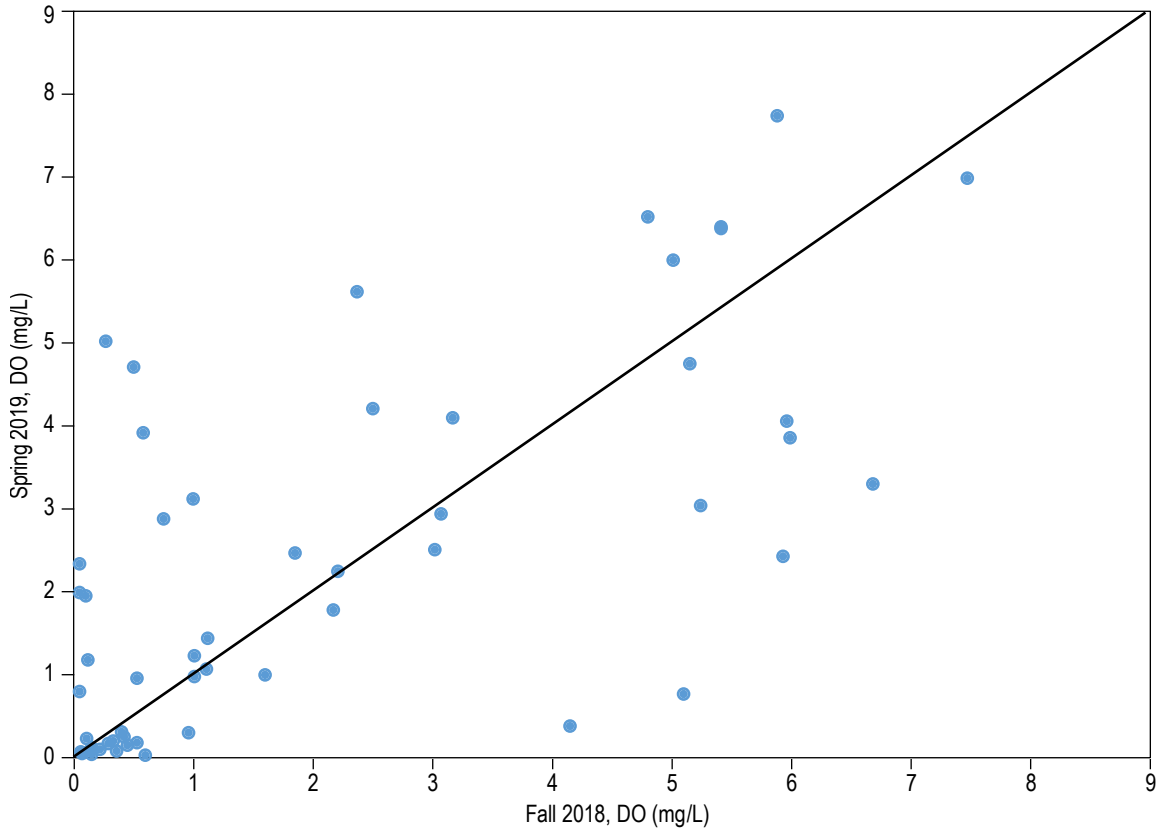

Figure 23. Comparison between dissolved oxygen measurements.

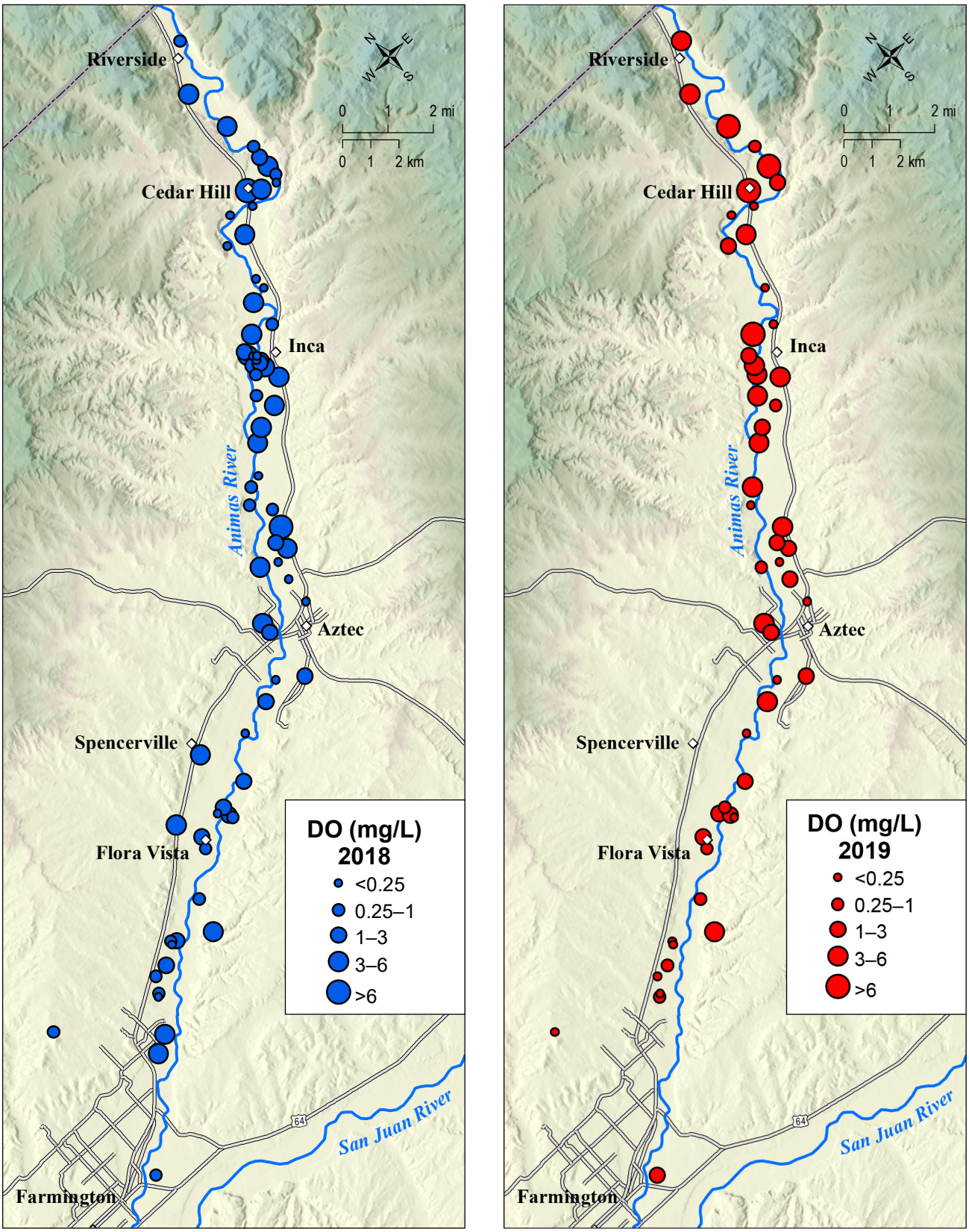

Figure 24. Spatial distribution of dissolved oxygen concentrations for samples collected in the fall 2018 (left) and spring 2019 (right).

were established to protect against consumption of drinking water contaminants that present a risk to human health. Manganese, iron, and aluminum are the only trace metals that were observed in some wells to exceed secondary maximum contaminant levels (SMCLs) (https://www.epa.gov/sdwa/secondary-drinking-water-standards-guidance-nuisance-chemicals) as defined by the U.S. Environmental Protection Agency secondary drinking water regulation, which is a non-enforceable guideline regarding cosmetic or aesthetic effects. While these contaminants are not health threatening, if present at levels above the SMCLs, these constituents may cause the water to appear cloudy or colored, or to taste or smell bad.

Figure 25, Figure 26, and Figure 27 shows the spatial distribution for total manganese, total iron, and total aluminum concentrations, respectively, for water samples that exhibited concentrations that exceed the SMCLs. As stated previously, samples analyzed for total concentrations were not filtered and samples analyzed for dissolved concentrations were filtered through a 0.45-micron filter. For this discussion, total concentrations are used because they are more representative of the water that well owners are consuming. No clear spatial trend was observed for total manganese and total iron concentrations. Both dissolved and total concentrations for manganese and iron were detected in the majority of the water samples collected (Table 5). Figure 28 shows the total concentration as a function of dissolved concentration for manganese and iron. For almost all the samples, total and dissolved manganese concentrations were almost identical, indicating that most manganese is in the dissolved phase. For iron, many samples exhibit significantly higher total concentrations, indicating that iron is often present as iron oxides/hydroxides.

Total aluminum was detected in 99 and 96 percent of the samples collected in 2018 and 2019 respectively, while dissolved aluminum was detected in 74 and 53 percent of samples. Therefore aluminum is commonly present in the solid phase. For AR-0115, located near Cedar Hill (Figure 27), the sample collected during the fall of 2018 exhibited a total aluminum concentration of 0.0008 mg/L, and dissolved aluminum was below the detection limit. In 2019, there was still no measurable dissolved aluminum, but total aluminum was slightly above the 0.05 SMCL at 0.063 mg/L. There was an even larger contrast observed for well AR-0003, located near Flora Vista (Figure 28). In 2018, total aluminum was 0.69 mg/L, well above the SMCL, and dissolved aluminum was 0.0013 mg/L. In the spring of 2019, total aluminum was 0.0083 mg/L.

Table 5. Proportion of water samples, in which iron and manganese were detected.

	Percent detection (%)	
Constituent	**Fall 2018**	**Spring 2019**
Dissolved Manganese	**78**	**86**
Total Manganese	**89**	**89**
Dissolved Iron	**61**	**71**
Total Iron	**91**	**89**
Dissolved Aluminum	**74**	**53**
Total Aluminum	**99**	**96**

For many metals in groundwater, whether they are present in the dissolved or solid phase depends on the Eh and pH. A plot of Eh versus pH (Figure 29) shows a rough inverse correlation. Samples collected in the fall of 2018 that exhibit the lowest pH values (pH <6.3) plot at the high end for Eh (300–500 mV). However, many samples with higher pH values also exhibit similar Eh values. With a few exceptions, water samples with Eh measurements less than 200 mV tend to have higher iron and manganese concentrations (Figure 30). To assess the temporal variability for Eh and dissolved manganese and iron concentrations, we calculated the ratio of 2018 measurements/2019 measurements for wells sampled both in the fall of 2018 and the spring of 2019. For dissolved iron and manganese, the majority of wells showed ratios less than one, indicating that concentrations were higher in spring 2019. Conversely, for Eh, the majority of wells showed a ratio greater than one, indicating that Eh values were generally higher in the fall of 2018.

Stable isotopes of hydrogen and oxygen

The stable isotopes of oxygen and hydrogen are useful tools for tracing the hydrologic cycle. The isotopic composition of a water sample refers to the ratio of the heavier isotopes to the lighter isotopes (R) for the hydrogen and oxygen that make up the water molecules. Because these stable isotopes are part of the water molecule, small variations in these ratios act as labels that allow tracking of waters with different stable isotopic signatures. All isotopic compositions in this report are presented as relative concentrations, or the per mil deviation of R of a sample from R of a standard (VSMOW) shown in the equation below:

$$\delta = \frac{R_{sample} - R_{standard}}{R_{standard}} * 1000‰$$

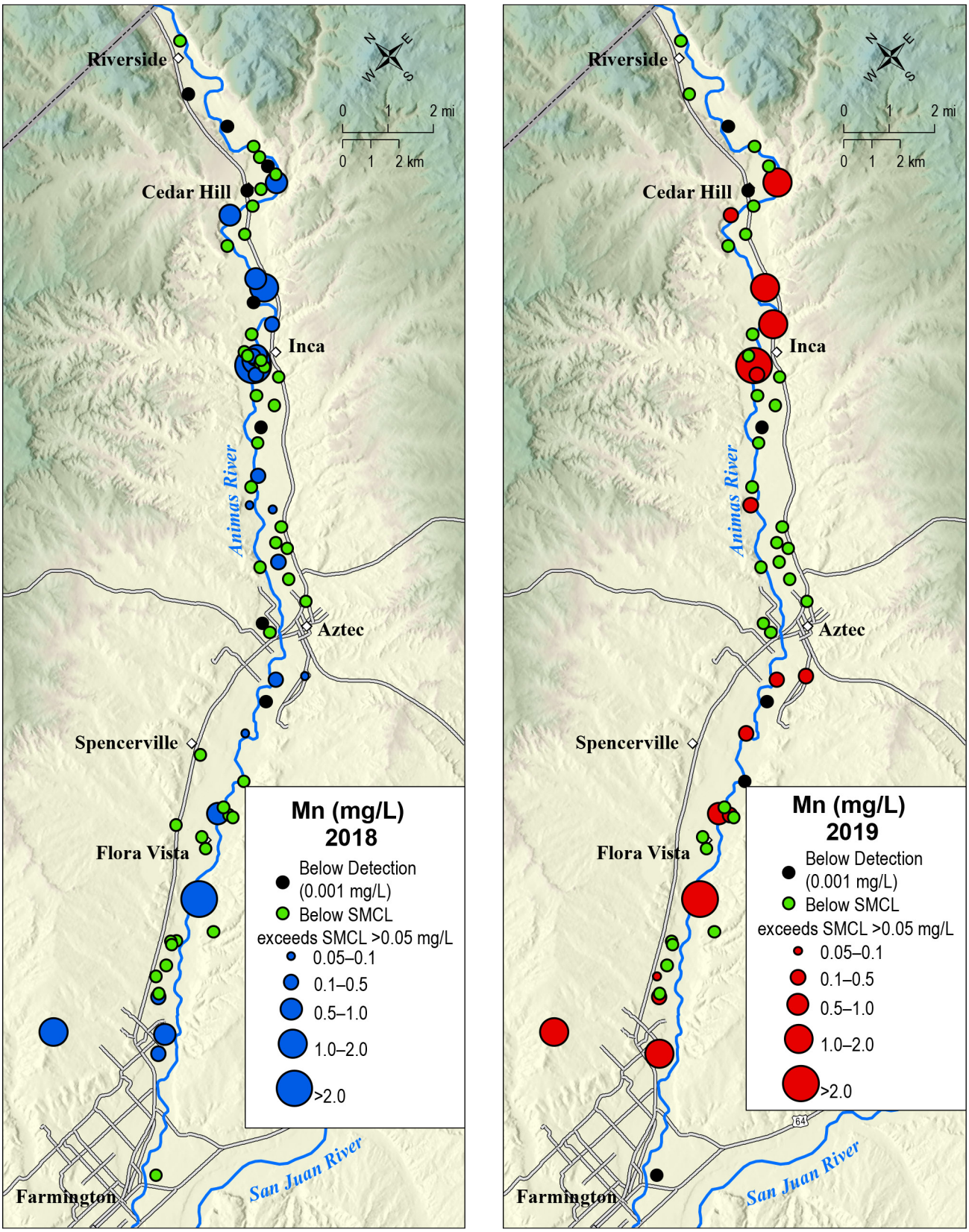

Figure 25. Spatial distribution of total manganese concentrations for wells that produced water with concentrations that exceed the EPA's secondary MCL (0.05 mg/L).

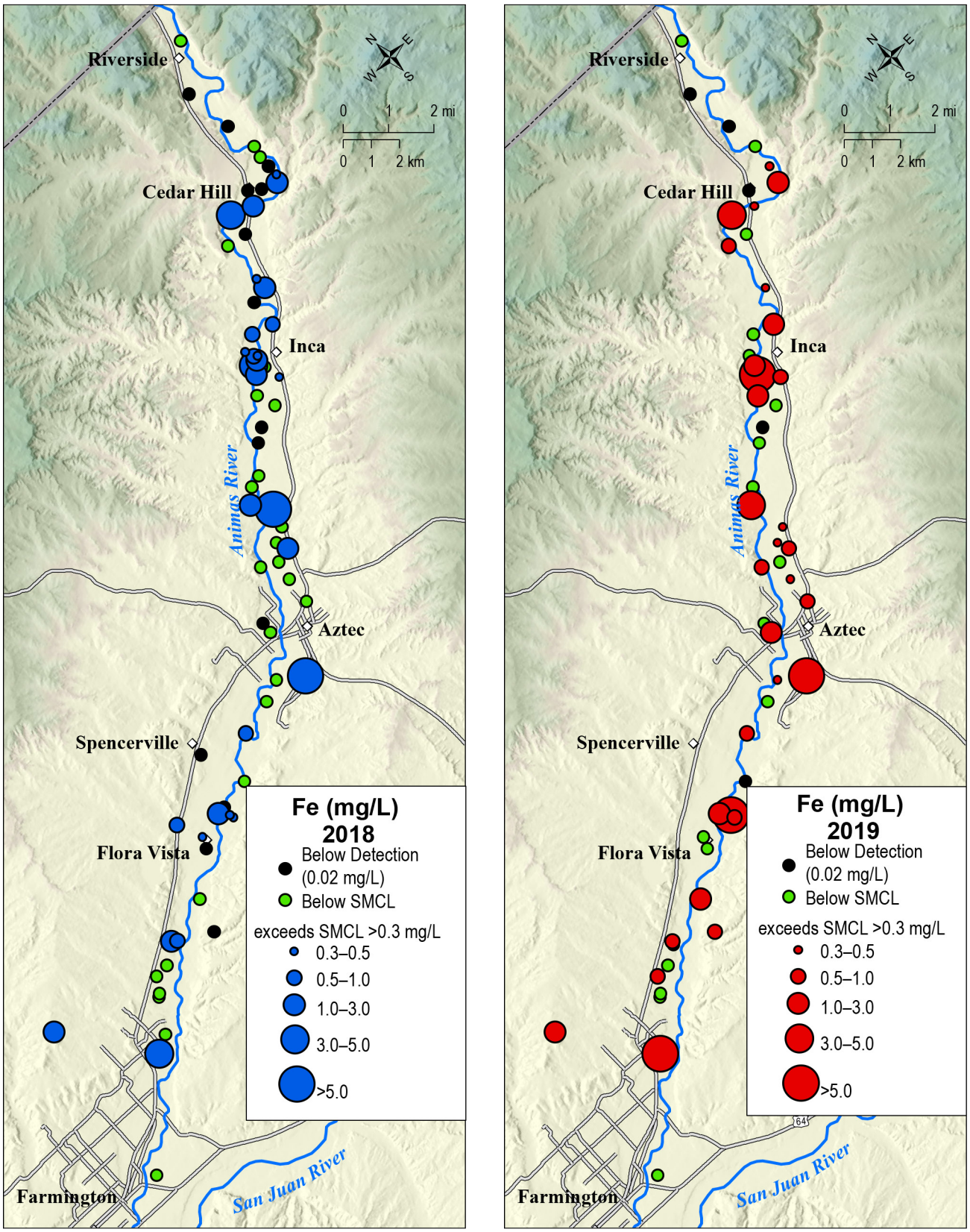

Figure 26. Spatial distribution of total iron concentrations for wells that produced water with concentrations that exceed the EPA's secondary MCL (0.3 mg/L).

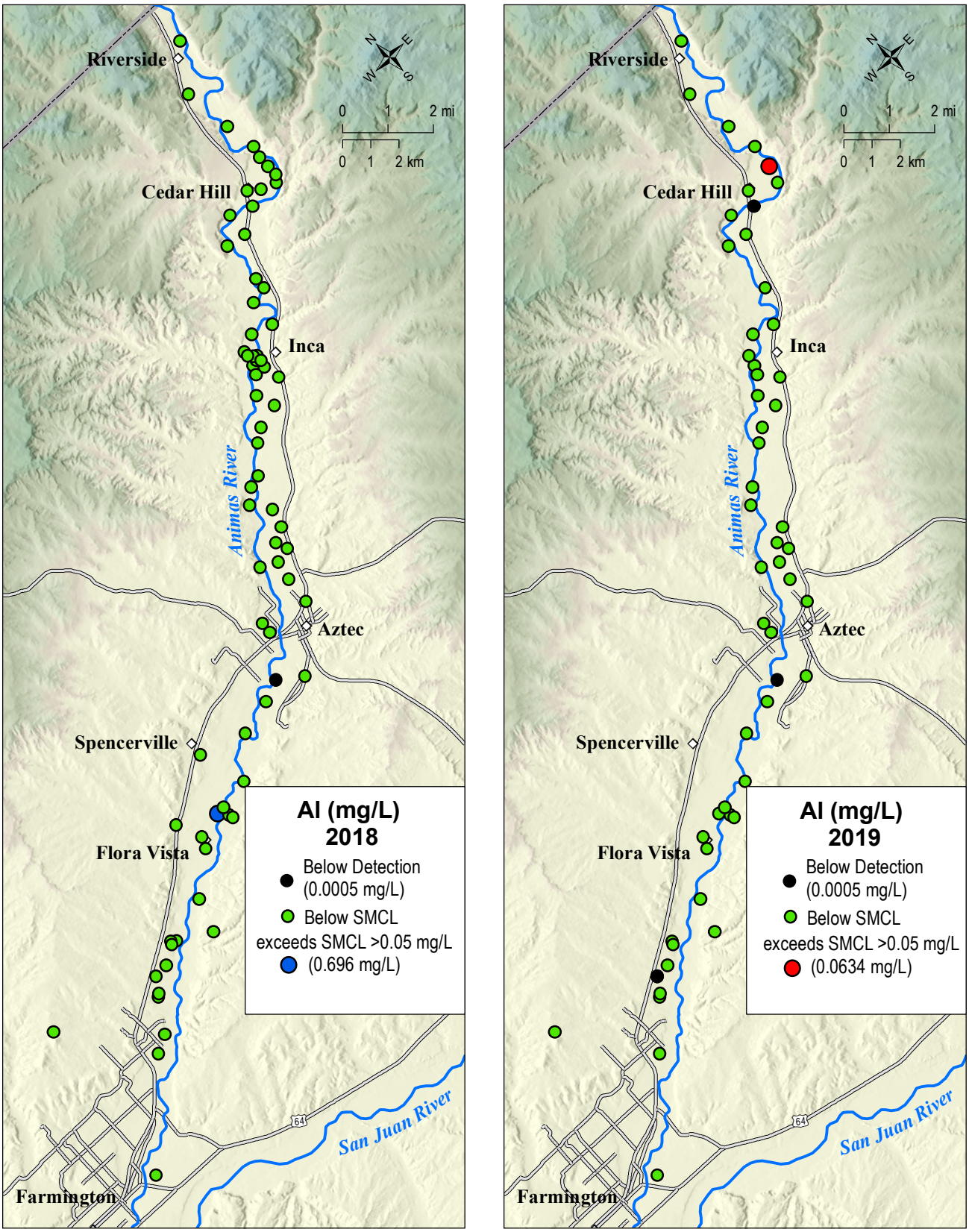

Figure 27. Location of wells that produced water with aluminum concentrations that exceed the EPA's secondary MCL (0.05 mg/L).

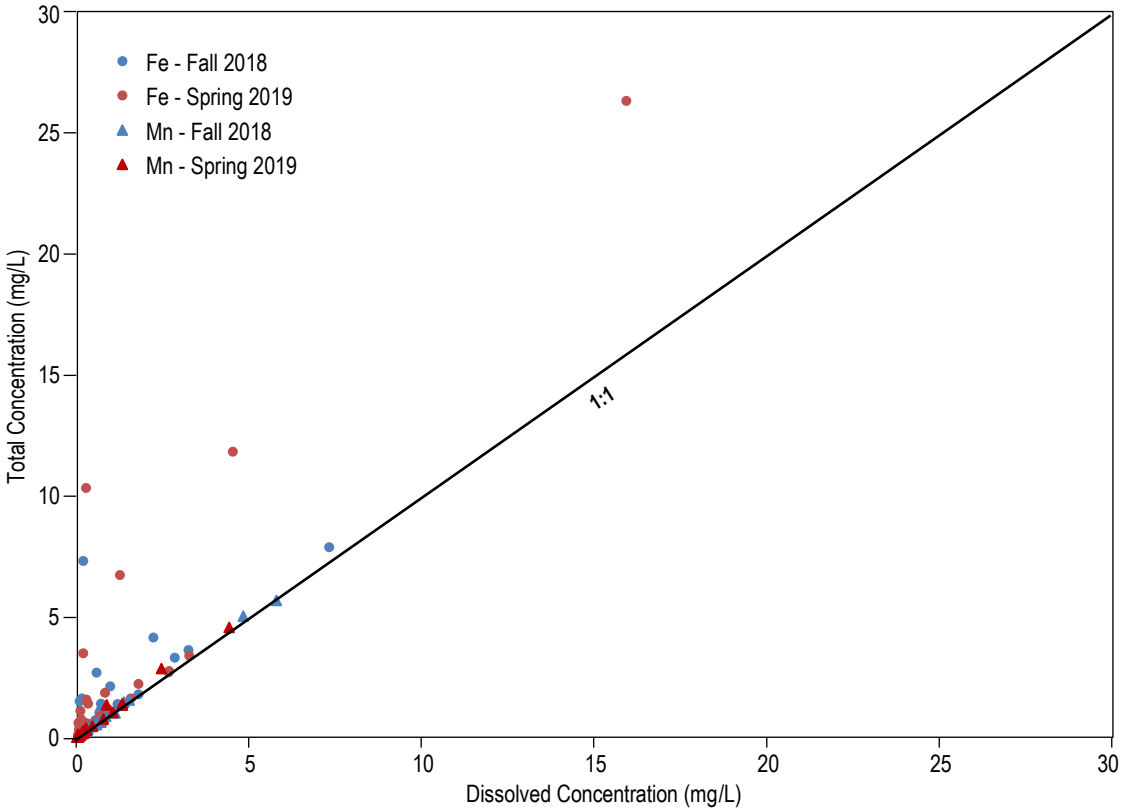

Figure 28. Total concentrations as a function of dissolved concentrations for iron and manganese.

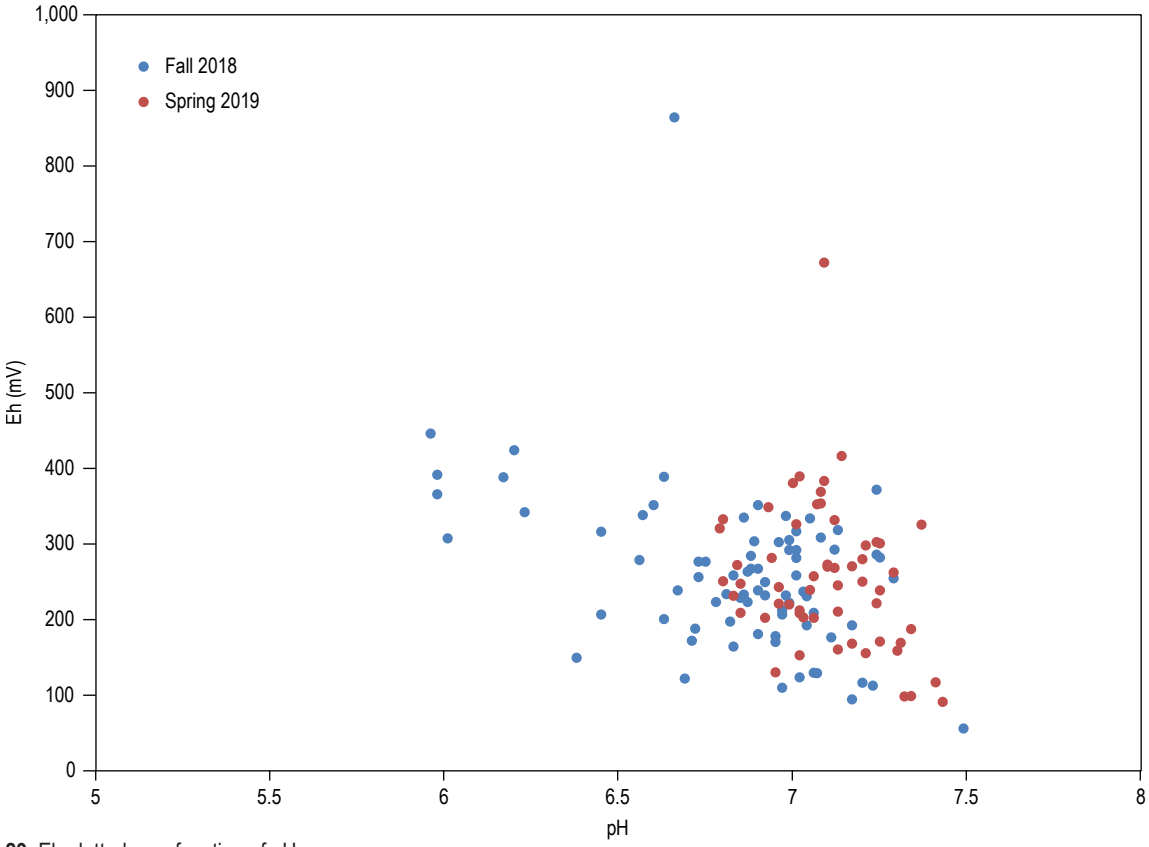

Figure 29. Eh plotted as a function of pH.

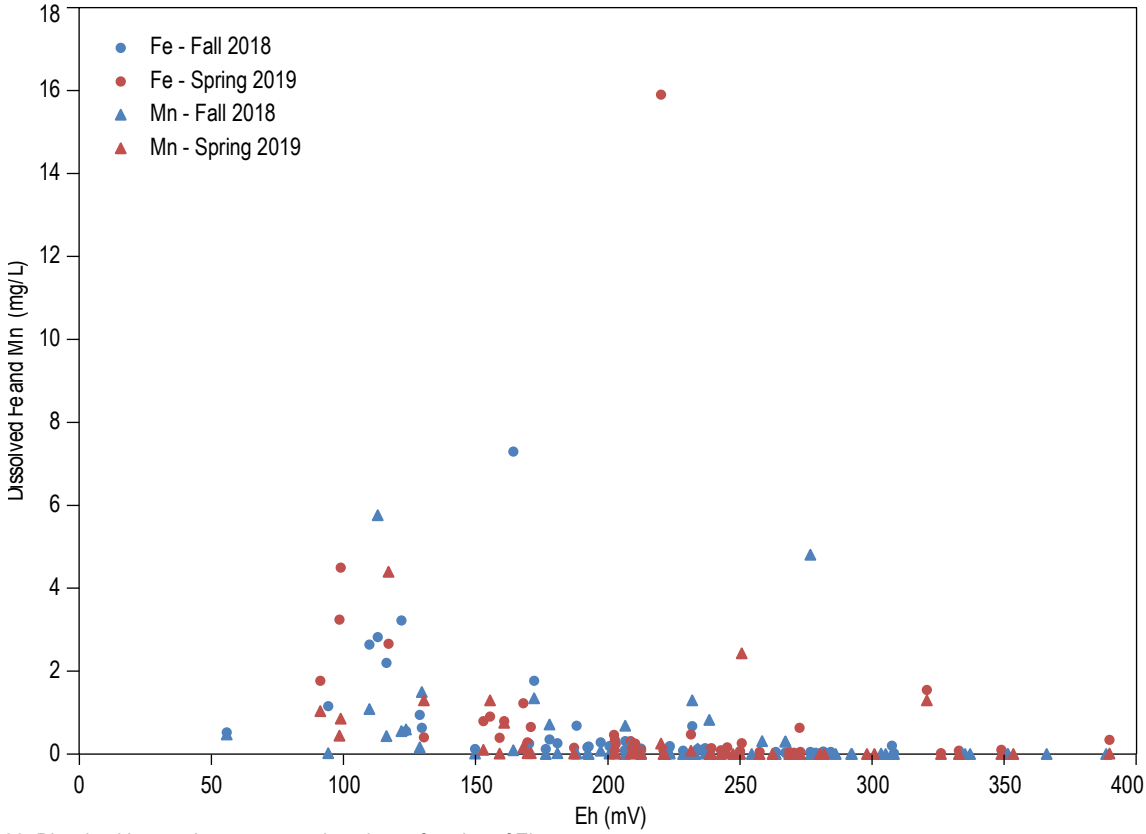

Figure 30. Dissolved iron and manganese plotted as a function of Eh.

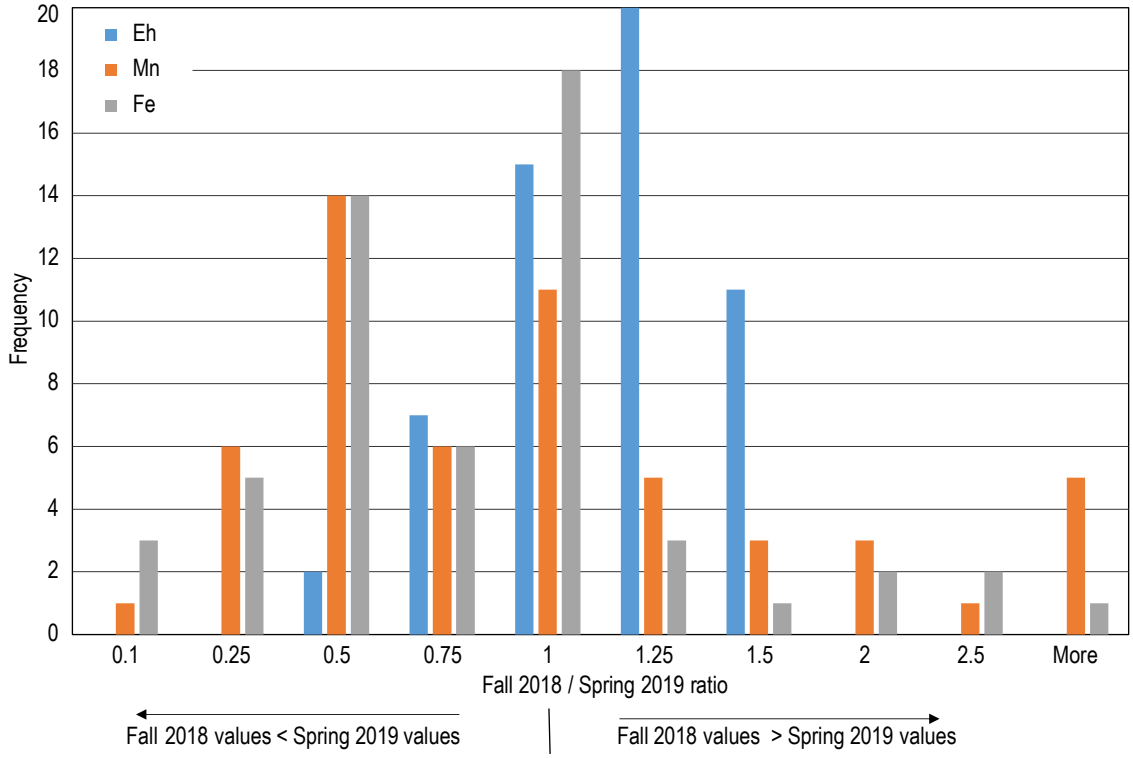

Figure 31. Histograms showing the distributions for the fall 2018 measurement/spring 2019 measurement ratios for Eh and dissolved iron and manganese concentrations in wells sampled for both sampling events. For samples with manganese and iron concentrations below the detections limits, we used the value of ½ the detection limit.

The isotopic composition of water fractionates during precipitation and evaporation due to undergoing these processes at slightly different rates for water molecules with different isotopic compositions ($^{1}H_2{}^{16}O$, $^{2}H^{1}H^{16}O$, $^{1}H_2{}^{18}O$). Isotopically lighter molecules evaporate at higher rates and heavier molecules precipitate at higher rates. It is useful to plot stable isotope data on a δD (hydrogen, ^{2}H) vs $\delta^{18}O$ (oxygen) graph, as shown in Figure 32. Almost all meteoric water ultimately originates from ocean water, which generally maintains a fairly constant isotopic composition (δD = 0‰, $\delta^{18}O$ = 0‰). Water vapor resulting from evaporation of ocean water is isotopically lighter than ocean water, and the isotopic composition of rain or snow that precipitates from this water vapor usually plots on or near the global meteoric water line (GMWL) with a slope of 8 and a deuterium excess (y-intercept) of 10 as demonstrated by Craig (1961) (Figure 32). However, the linear trend that characterizes local precipitation in a specific area may deviate from the GMWL with a similar slope but a different deuterium excess. Isotopic characterization of local precipitation is often very useful for identifying groundwater recharge sources and mechanisms. Newton et al., (2017) estimated a local meteoric water line (LMWL) (Figure 32) based on the isotopic composition of Animas River samples collected in several areas from the headwaters to the confluence of Animas and San Juan rivers. The isotopic compositions of river water defined an evaporation line that showed a larger degree of evaporation for samples collected farther downstream. Therefore the isotopic composition of river water at the headwaters of the Animas near Cement Creek were assumed to show no evaporation and to plot on the LMWL. Assuming a slope of 8, the estimated LMWL was characterized with a deuterium excess of 17. Nordstrom et al., (2007) described the Rocky Mountain meteoric water line (RMMWL), which has a slope of 8.1 and a deuterium excess of 14.8.

Figure 32 shows the isotopic composition of groundwater samples collected in the fall of 2018 and the spring of 2019. The isotopic composition of AR-0213 (Newton et al., 2017) is also included. Both datasets (fall 2018 and spring 2019) plot roughly along two apparent evaporation lines with similar slopes, 5.5 and 5.8 for the fall and spring sampling events respectively. For wells sampled during both sampling events, the majority of samples collected in

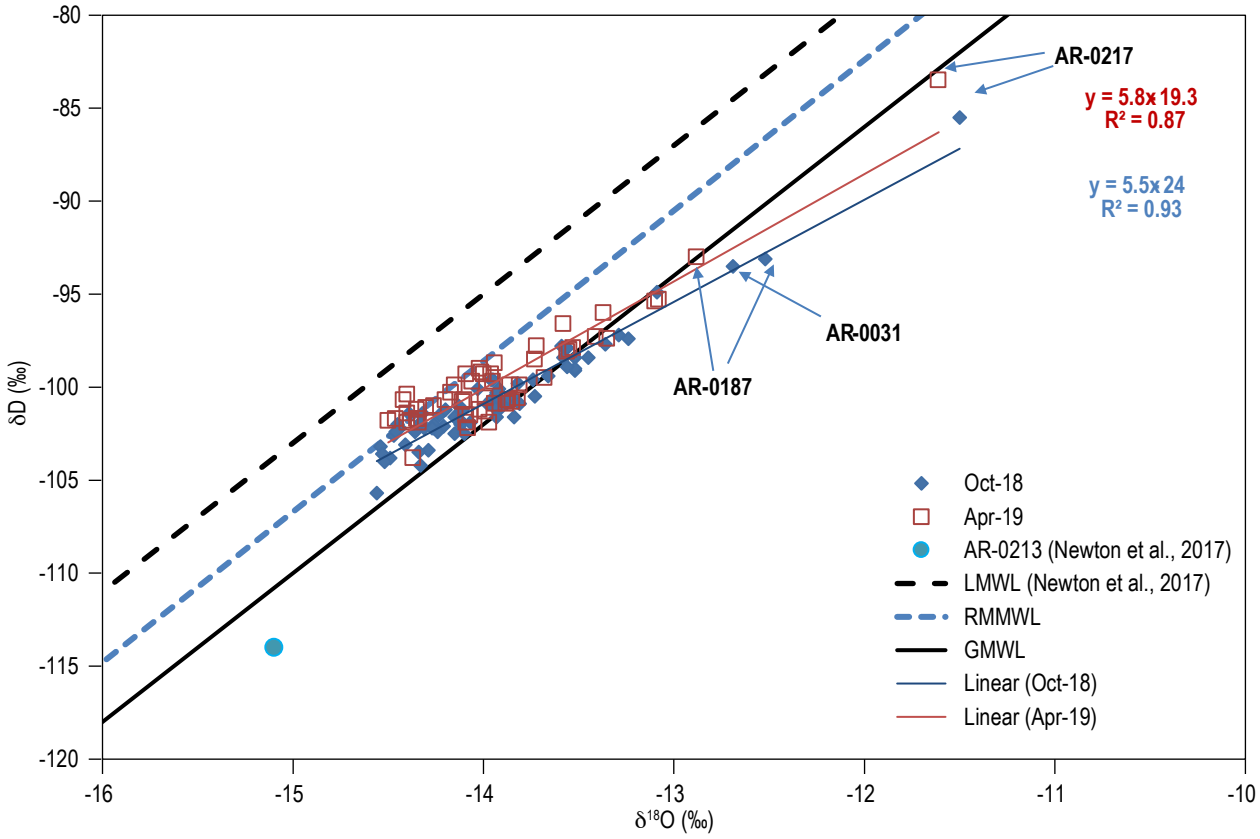

Figure 32. Stable isotopic composition of groundwater samples,local meteoric water line (LMWL) estimated by Newton et al., (2017) and the Rocky Mountain meteoric water line (RMMWL) presented by Nordstrom et al., (2007).

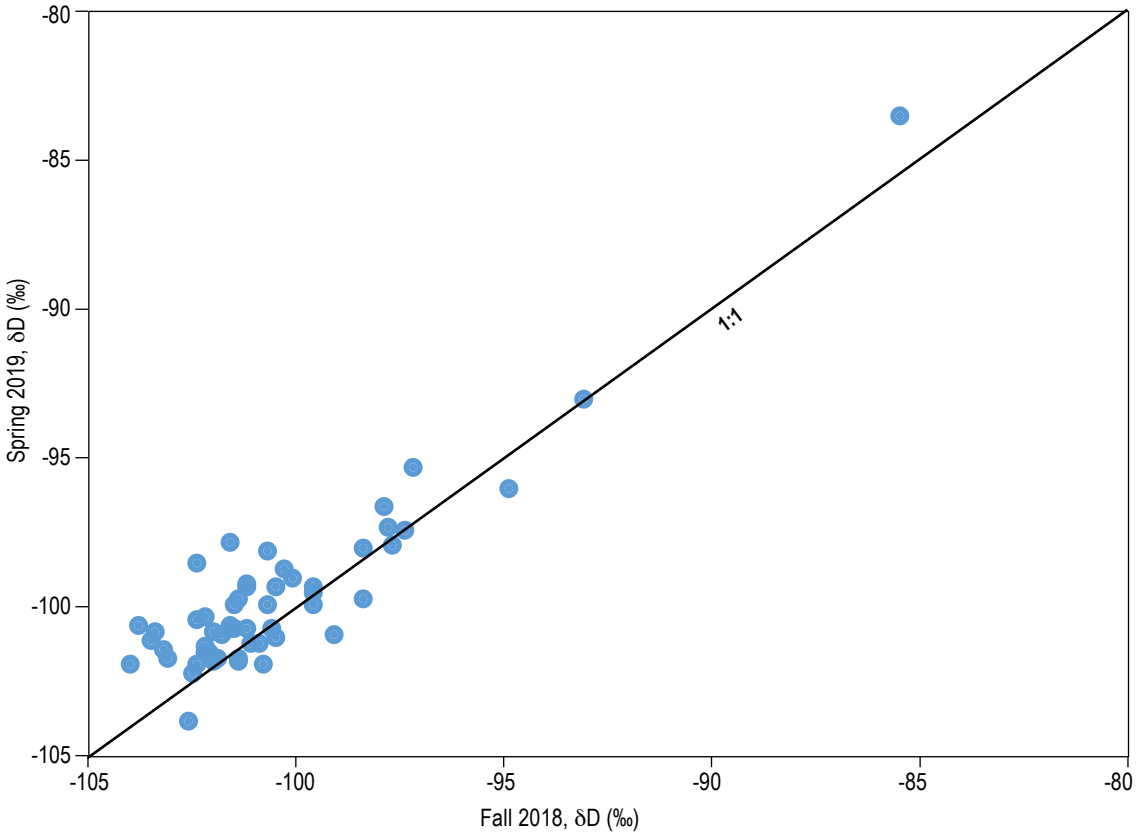

Figure 33. Comparison of hydrogen isotope data for wells which were sampled for both sampling events.

the spring of 2019 were isotopically heavier than those collected in 2018 (Figure 33).

Stable isotopic composition of dissolved sulfate

We analyzed a subset of samples for the stable isotopes of sulfur ($\delta^{34}S$) and oxygen ($\delta^{18}O$) in dissolved sulfate to assess sulfate sources in the shallow aquifer in the Animas Valley. The stable sulfur isotopic values for groundwater in the Animas Valley ranged from -12.3 to 9.2‰, with the lighter values ($\delta^{34}S$ <0) located south of Aztec (Figure 34). Stable oxygen isotopic compositions in sulfate (only analyzed for samples collected in 2018) ranged from -2.8 to 4.8‰ and also show the lightest values to the south of Aztec (Figure 35). The water sample from AR-0217 exhibits the lightest $\delta^{34}S$ and $\delta^{18}O$ values, and interestingly, the sample collected from AR-0187 exhibits a slightly lighter sulfur isotopic value than other wells in the area. Figure 36 shows $\delta^{34}S$ as a function of $\delta^{18}O$. Wells producing water with the lightest sulfate stable isotopic compositions are located south of Aztec. These data and their implications for solute source identification is discussed in detail in the Discussion section below.

Stable isotopic composition of dissolved inorganic carbon

Similar to the sulfur and oxygen isotopes in sulfate, and the hydrogen and oxygen isotopic composition of water, carbon isotope data for DIC are reported in δ-notation as a per mil deviation of the $^{13}C/^{12}C$ ratio for a sample from that of a standard (Peedee Belemnite, PDB). $\delta^{13}C$ (DIC) values ranged from -17.2 to -9.8‰, with AR-0217 having the lightest value, which was the same for both sampling events. Figure 37 shows the spatial distribution for $\delta^{13}C$ values for water samples collected in the fall of 2018 and spring of 2019. While there is no obvious trend, it should be noted that the lightest values are observed in the southernmost portion of the study area. Carbon isotopes in DIC show a rough linear inverse correlation with dissolved bicarbonate concentrations (Figure 38), which range from 186 to 429 mg/L. Most water samples that show an apparent decrease in $\delta^{13}C$ (DIC) are near saturated or over-saturated with respect to calcite (Figure 38).

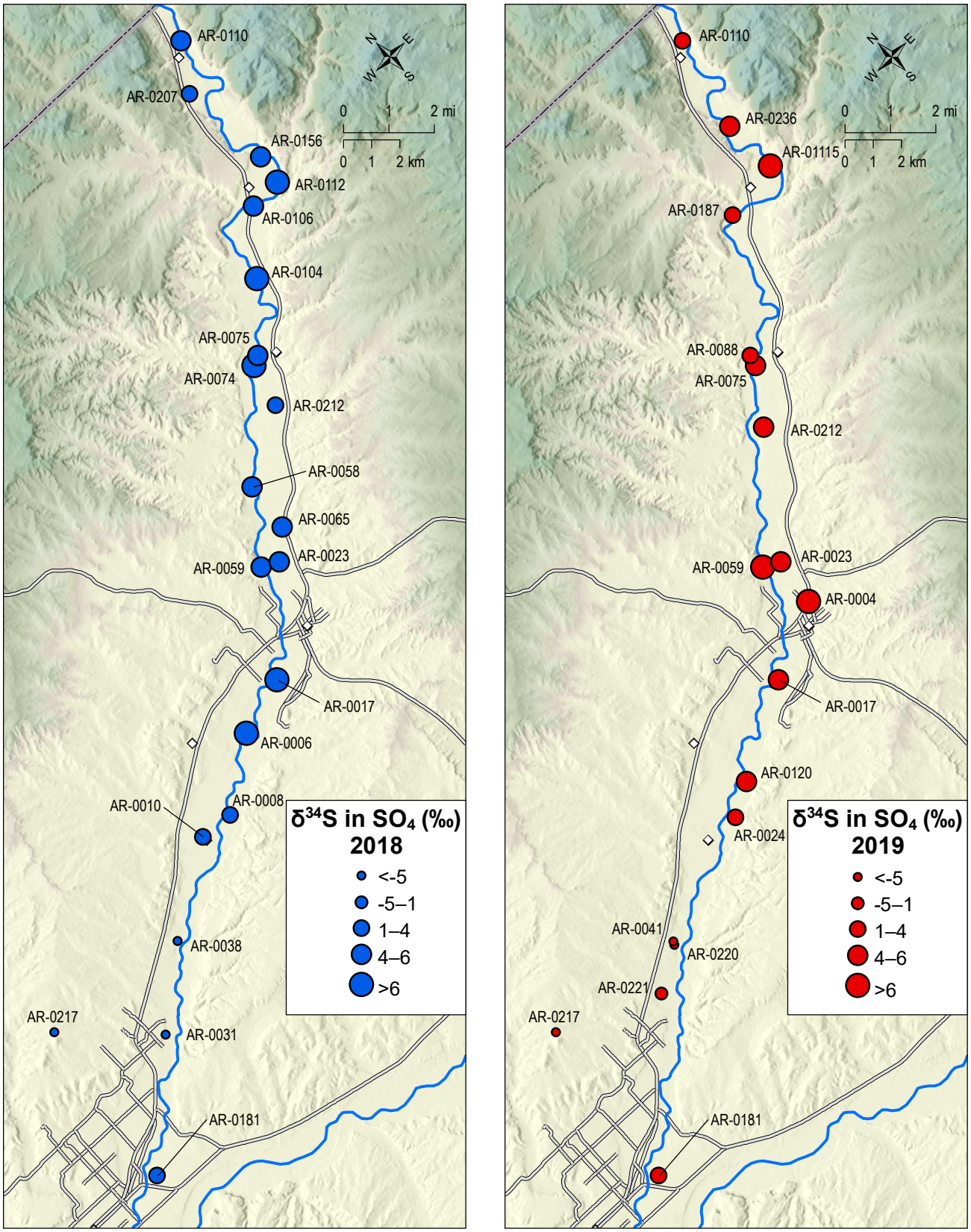

Figure 34. Spatial distribution of $\delta^{34}S$ in sulfate for samples collected in the fall of 2018 and spring of 2019.

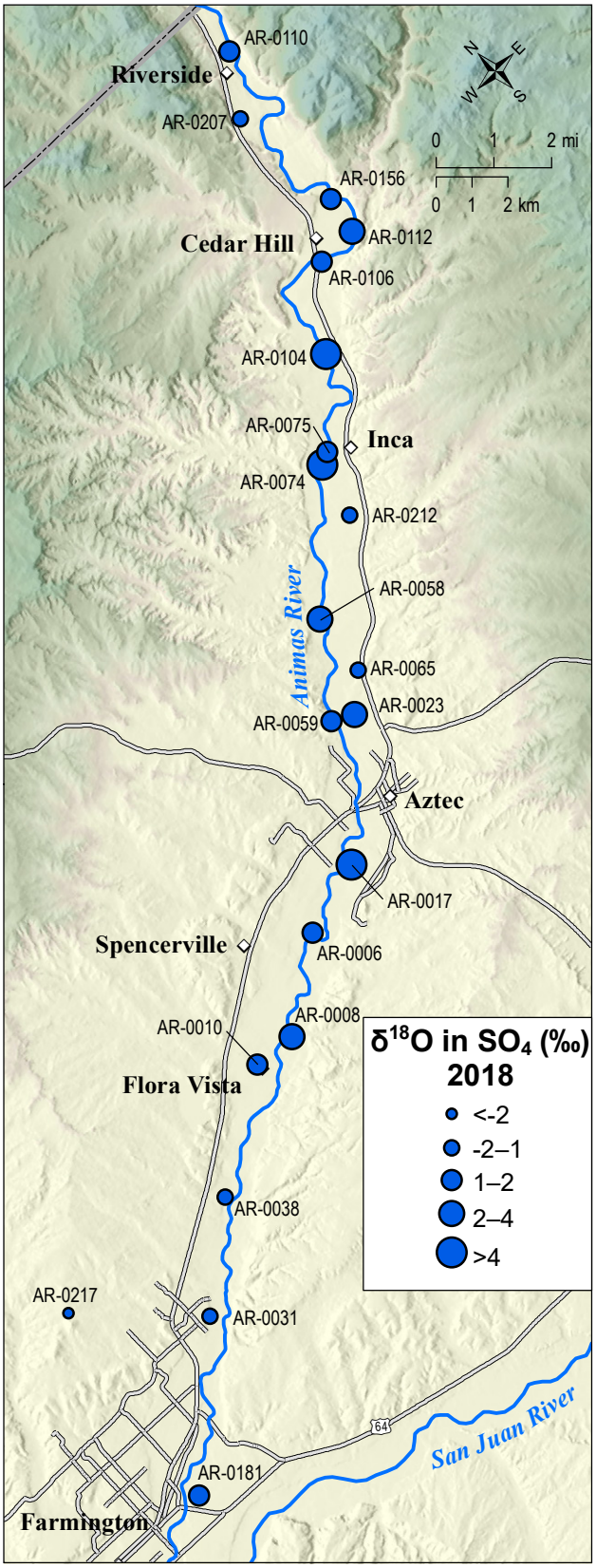

Figure 35. Spatial distribution of $\delta^{18}O$ in sulfate for samples collected in the fall of 2018.

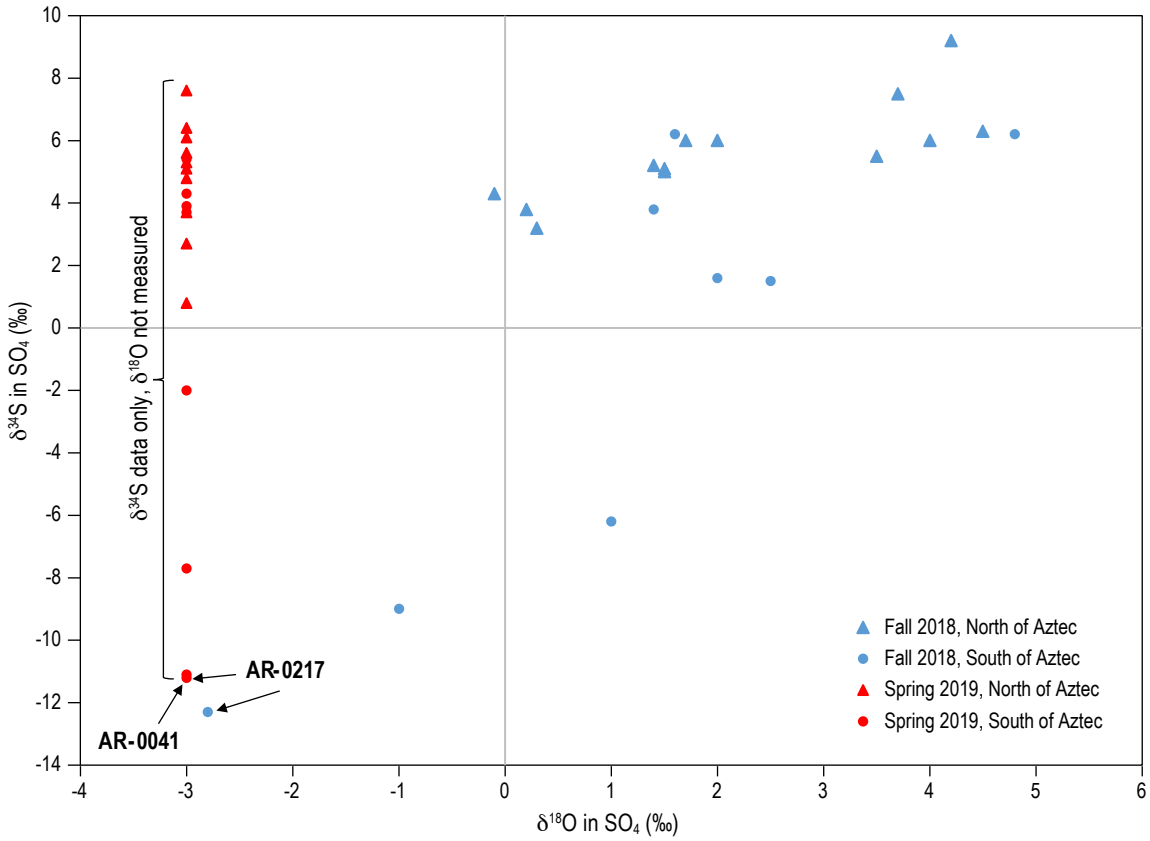

Figure 36. $\delta^{34}S$ plotted as a function of $\delta^{18}O$ for sulfate in samples collected in 2018. Samples collected in 2019 were analyzed for $\delta^{34}S$ only.

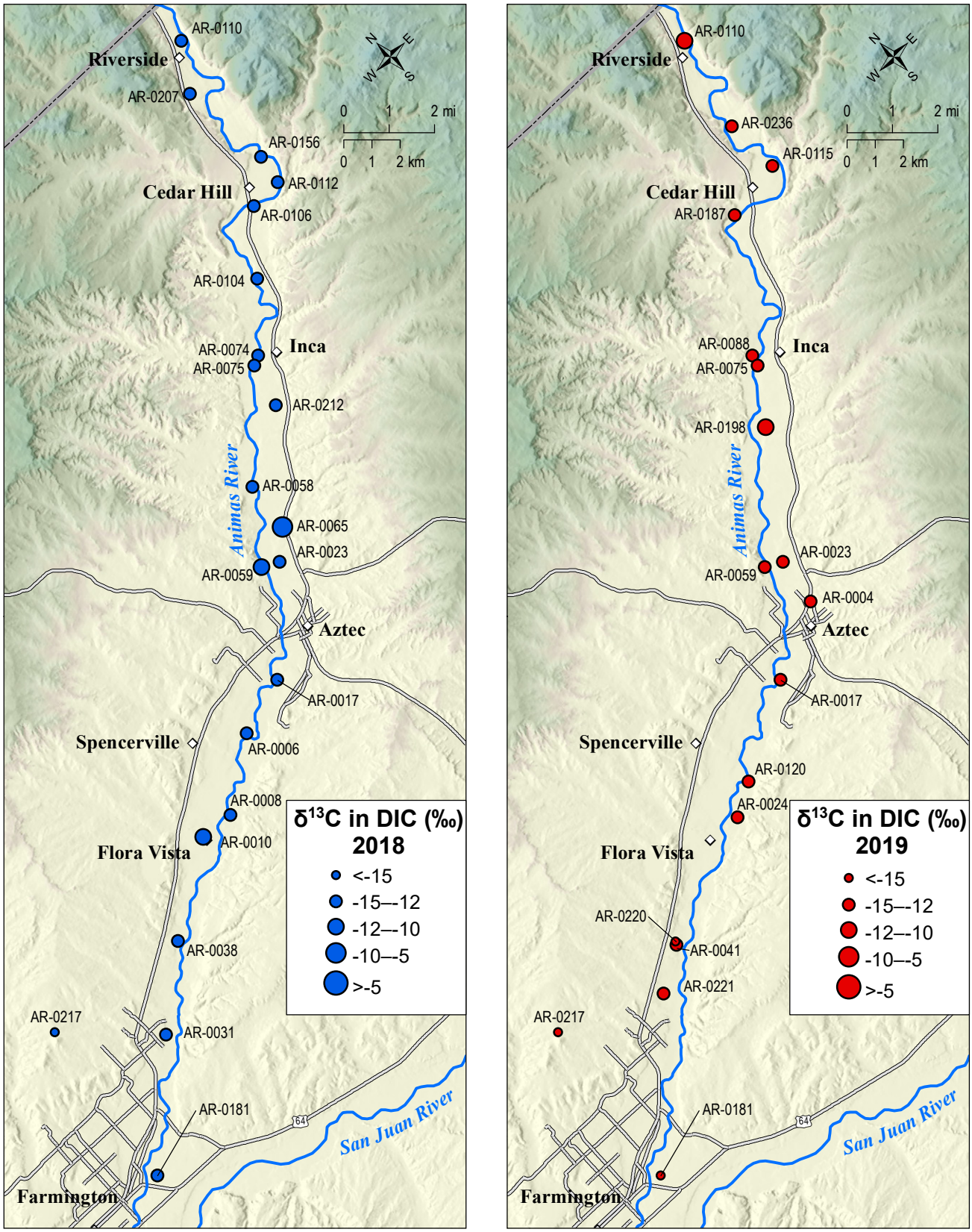

Figure 37. Spatial distribution of the stable isotopic composition for dissolved inorganic carbon (DIC).

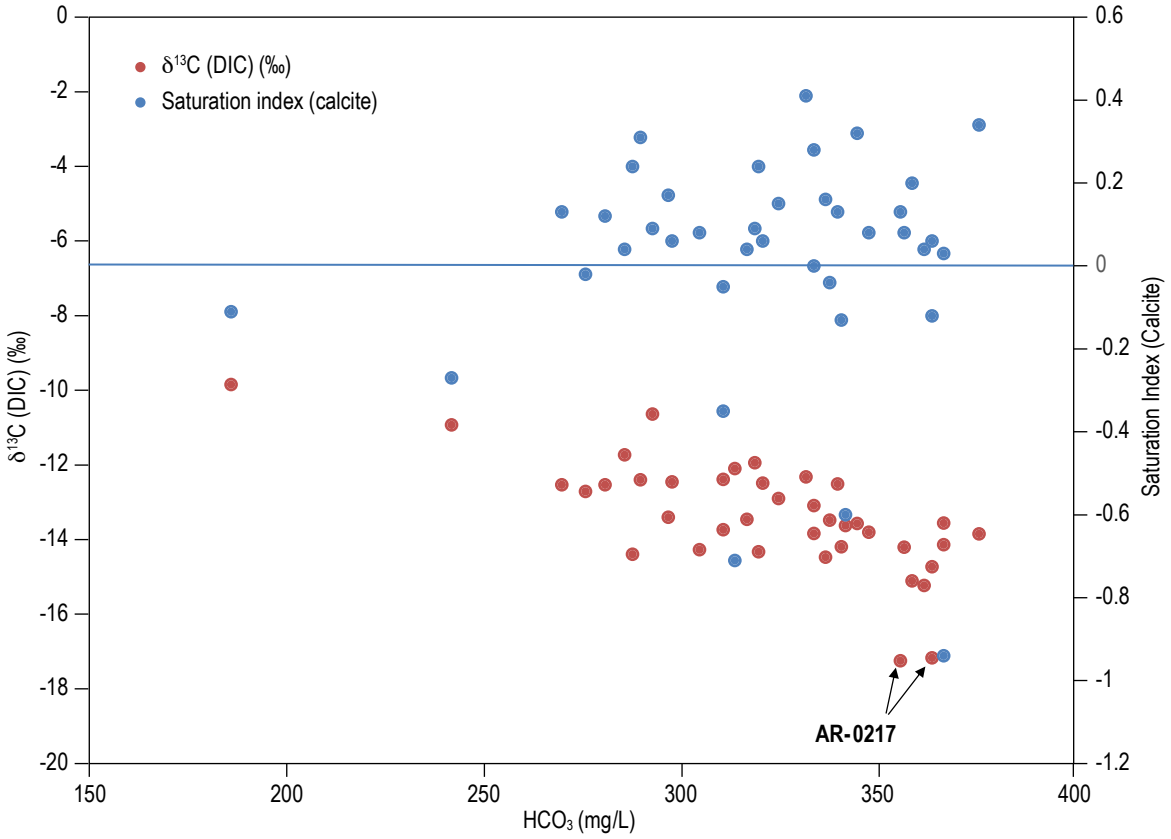

Figure 38. Carbon isotopic composition ($\delta^{13}C$) in DIC and the saturation index for calcite plotted as a function of bicarbonate concentration.

V. DISCUSSION

Groundwater Flow Conditions

Consistent with findings by Newton et al., (2017), for most wells, the depth to the water table was deeper in spring 2019 than that measured in fall 2018 (Table 2). Groundwater level elevations in much of the Animas Valley are higher during the irrigation season due to irrigation water recharging the alluvial aquifer. Continuous water level data allowed us to compare groundwater level fluctuations in 2018 to those in previous years. Figure 16 and Figure 17 show hydrographs for an irrigation-controlled and river stage-controlled wells respectively, as determined by Newton et al., (2017). While the irrigation ditch (Figure 16) shows slightly less water towards the end of the 2018 irrigation season than seen in previous years, the water level in well AR-0116 increased to levels comparable to those observed during the two previous years. We also compared water levels measured in October 2016 and October 2018 for several wells that were identified as irrigation controlled (data not shown), and there was no significant difference. Therefore, for wells in areas where the groundwater level is primarily controlled by irrigation, water levels don't appear to be significantly affected by extreme changes in river stage. Figure 17 shows the groundwater level fluctuations in the well AR-0007, as well as river stage data from the USGS gage below Aztec, NM. An increase in the depth to water in 2018, compared to previous years, suggests that water levels in wells controlled by stage of the river are affected by extreme changes in river discharge.

Groundwater level data for both sampling events were contoured (Figure 38 and Figure 39) to assess groundwater flow directions groundwater/surface water interactions and show similar characteristics to water table contours constructed by Newton et al., (2017). Groundwater generally flows parallel and towards the river, indicating gaining conditions along most of the NM reach. Water table contours for 2018 (Figure 38) and 2019 (Figure 39) look remarkably similar even with the historically low river discharge rates in 2018. With the number of data points used, there are no significant differences in groundwater flow conditions observed in the fall of 2018 and spring 2019. However, in localized regions in the northern portion of the study area, we observed water levels in some wells that appeared to be below adjacent river stage elevation (denoted by red points in Figure 38 and Figure 39), indicating a possible reversal in the hydraulic gradient between the river and the aquifer. This apparent localized reversal in gradient, which was also observed by Newton et al., (2017), was primarily observed in the spring of 2019 during base flow conditions and have implications for potential groundwater contamination due to the input of contaminated river water.

Geochemical Controls on Water Chemistry

Water chemistry data presented above provides evidence for important geochemical processes that control major ion chemistry of shallow groundwater in the Animas Valley. General chemistry analyses for samples collected in 2018 and 2019 exhibited similar ranges in concentrations and similar spatial distributions to that observed by Newton et al., (2017). Sulfate and TDS concentrations in groundwater appear to significantly increase down gradient, to the south and west, with the highest sulfate concentrations observed south of Aztec (Figure 18). In this section we discuss different geochemical processes that control the groundwater chemistry, resulting in the observed spatial and temporal trends.

Evaporation and mixing processes

The stable isotopic compositions ($\delta^{18}O$ and δD) of water samples collected for this study show clear evidence that most water sampled has under gone some degree of evaporation. Isotopic compositions for all water samples collected in the fall of 2018 and spring of 2019 plot along two different but similar apparent evaporation lines (Figure 32). Figure 41 shows chloride concentrations as a function of δD and provides additional evidence that these waters

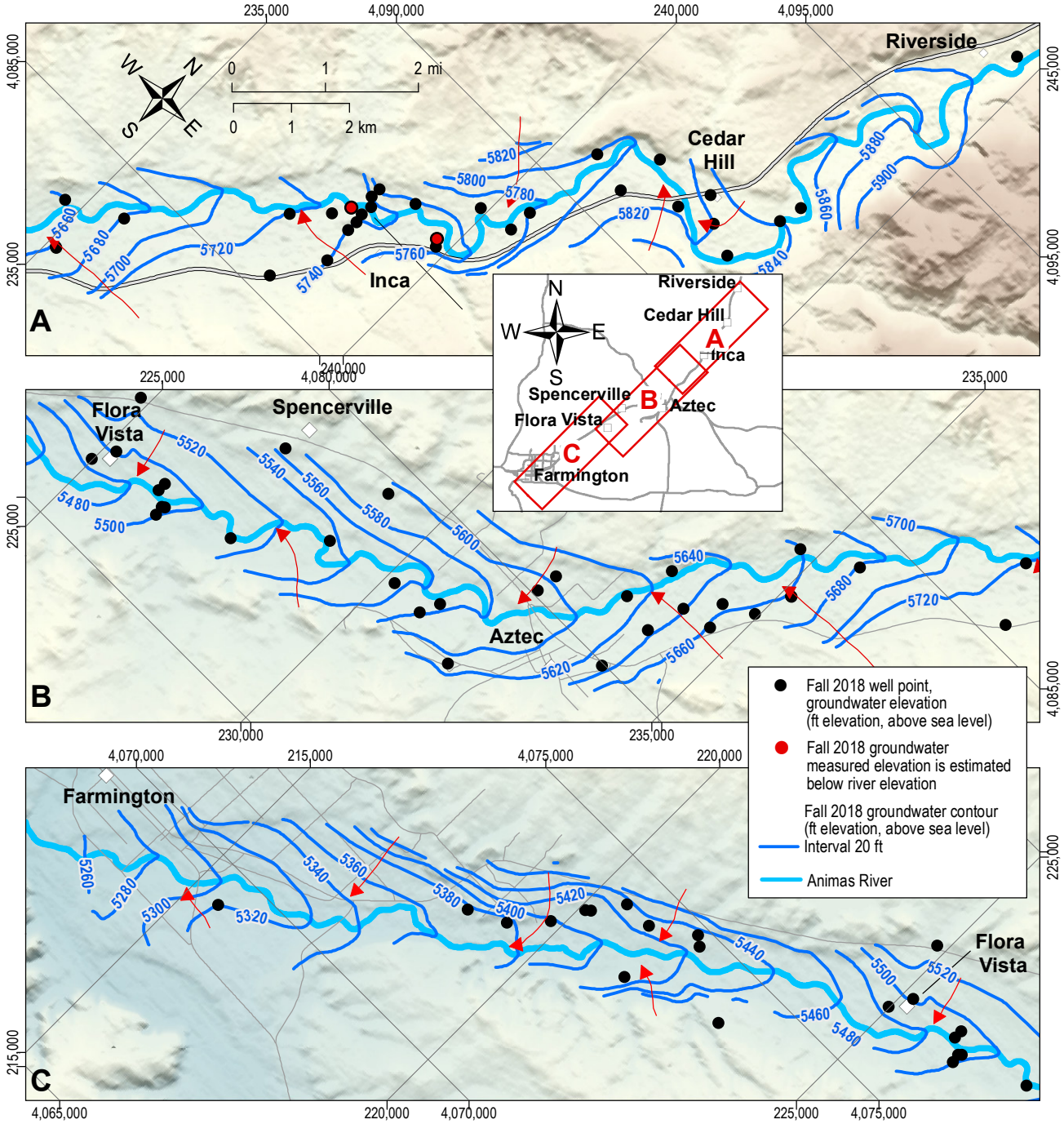

Figure 39. Groundwater level elevation contours for fall 2018 sampling event.

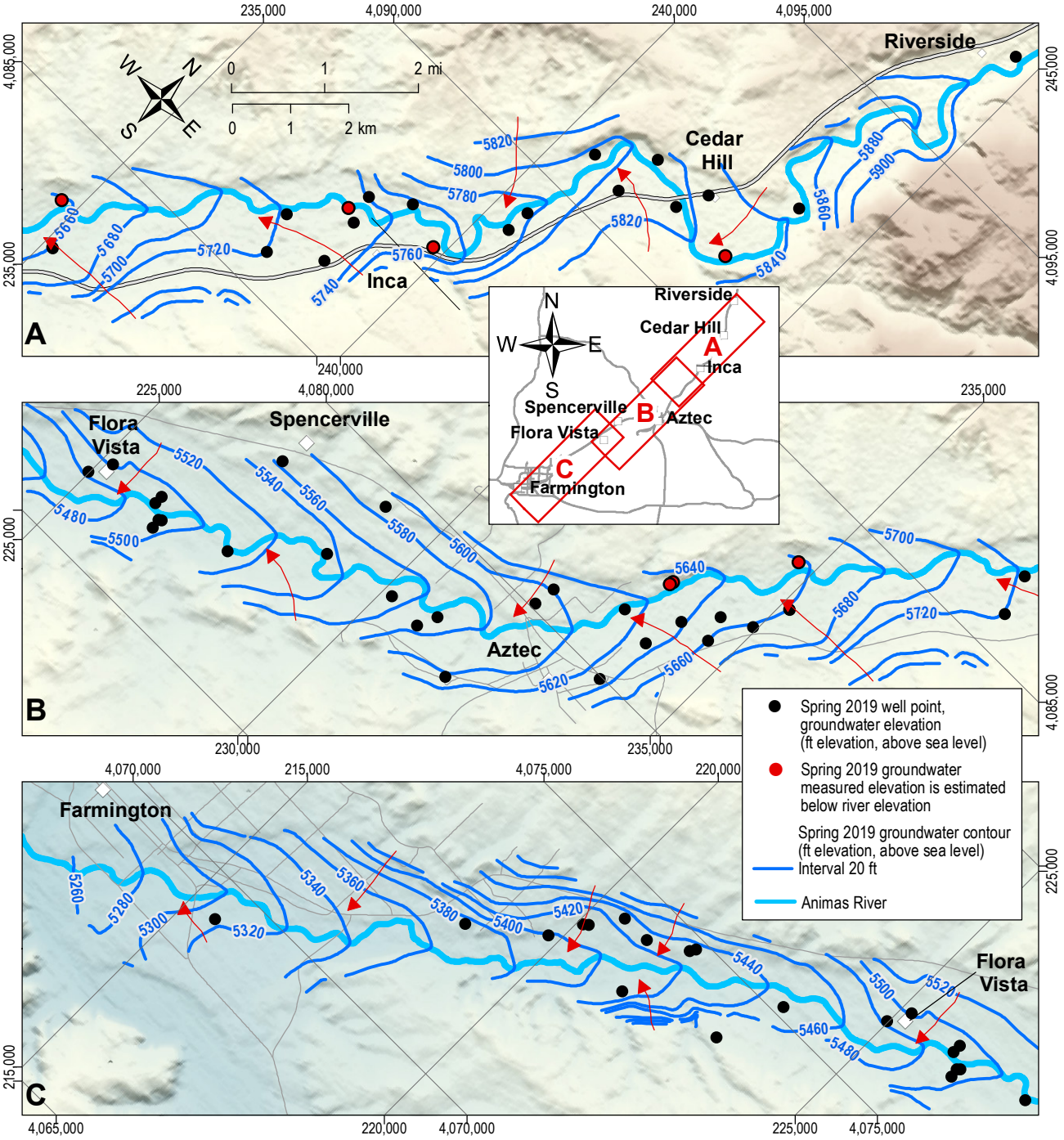

Figure 40. Groundwater level elevation contours for spring 2019 sampling event.

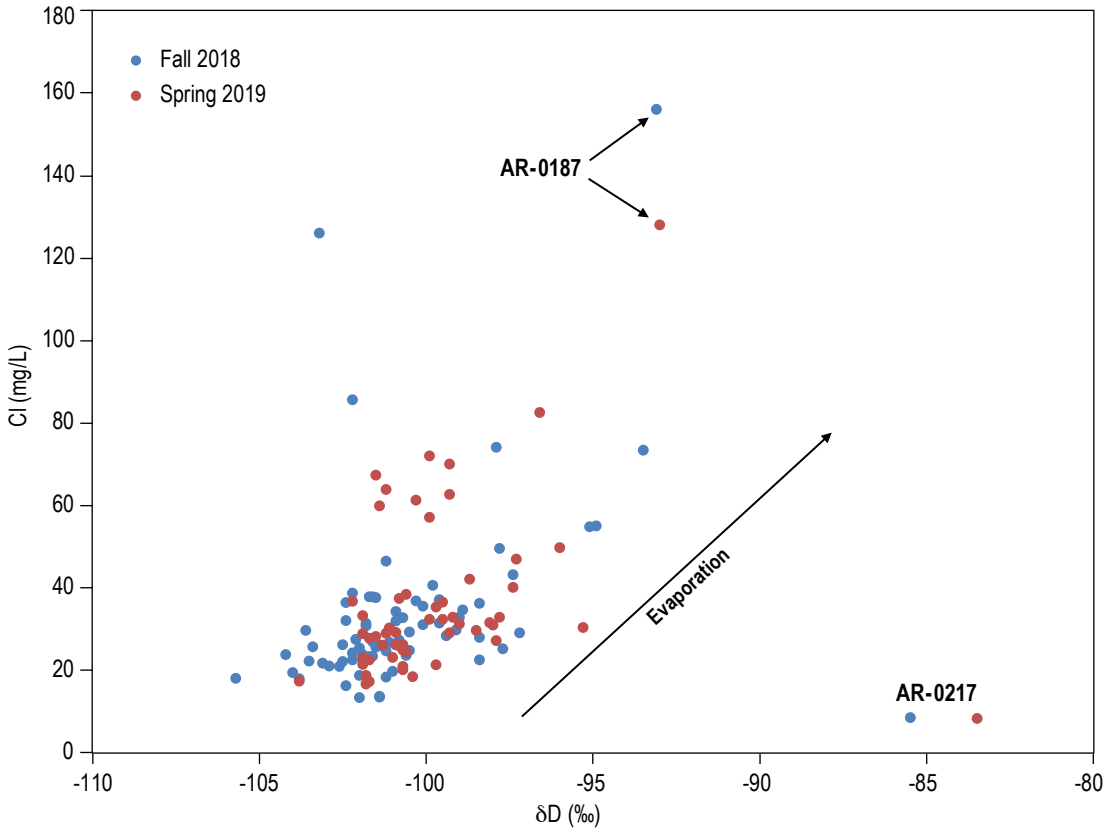

Figure 41. Chloride as a function of deuterium isotopic composition. The rough direct correlation between chloride and δD values is due to evaporation. The arrow shows the general change in chloride concentrations and δD expected due to evaporation.

have undergone evaporation. While there is significant scatter in the data, most data follows a general direct correlation where both the chloride concentration and the isotopic composition increase due to evaporation. Samples collected from AR-0217 exhibited a heavy isotopic composition (Figure 32) that plots near the GMWL, probably representing a modern mixture of local winter and summer precipitation. Data points for AR-0217 in Figure 41 are outliers in the chloride-δD evaporation trend, with relatively low chloride concentrations and heavy isotopic values, suggesting water from this well is not affected by evaporation and likely represents a different water source. Water from AR-0187 stands out as the most evaporated water on both evaporation lines in Figure 32 and on the evaporation trend seen in Figure 41.

Geochemical trends also indicate the mixing of different water sources. The linear trend between bicarbonate-dominant and sulfate-dominant water on the anion portion of the Piper diagram (Figure 19) is likely due to the mixing of two or more water sources. Relative cation concentrations may also show a mixing trend between calcium-dominant water and sodium-dominant water, but these data are also likely affected by cation exchange processes where aqueous calcium and magnesium are exchanged with adsorbed sodium on sediments. While there is no doubt that almost all water sampled has undergone cation exchange to some degree (Newton et al., 2017), for the following discussion, we assume that the extent of cation exchange that the different mixing endmembers have undergone remains constant. The distribution of data in the diamond portion of the Piper diagram in Figure 19 is likely due to mixing of three or more endmembers, a freshwater endmember and two or more high-sulfate endmembers. The following discussion examines the mixing relationships between different apparent endmembers from several different perspectives.

The freshwater endmember, which is not represented by water from a single well, is chemically similar to river water, characterized as calcium-bicarbonate water type with relative sulfate concentrations between 0.3 and 0.4 and TDS concentrations between 300 and 700 mg/L. Wells that produce water samples considered as possible high-sulfate mixing endmembers include AR-0213 (Newton et al., 2017), AR-0217, and AR- 0019. Newton et al., (2017) sampled the well AR-0213, which is completed in a bedrock aquifer just outside the river valley with a

total depth of about 500 feet bgs. This water sample stood out as an endmember with respect to water type (Figure 19), TDS, sulfate concentrations, isotopic composition (Figure 32), and age. AR-0213 produced a sodium-sulfate water type with the highest TDS and sulfate concentrations of 10,000 mg/L and 6,320 mg/L (relative sulfate concentration of 0.93) respectively. Water from AR-0213 exhibited with very light $\delta^{18}O$ and δD values, representative of very old water that originated as precipitation in the Pleistocene (Phillips et al., 1989). Also, this water sample exhibited an apparent carbon-14 age of about 20,000 years before present. Carbon-14 data was not corrected for hydrogeochemical processes such as the dissolution of calcite or limestone. The deepest well sampled for this study (total depth ~ 340 feet bgs), AR-0217, which is also located outside the river valley, produced calcium-sulfate water with a relatively high TDS concentration of about 1,500 mg/L and a sulfate concentration of about 830 mg/L (relative sulfate concentration of 0.74). As mentioned above, stable isotope data suggests that this water is likely modern local precipitation (plots near GMWL) and does not show evidence of evaporation, as seen for most other water samples. The well, AR-0019 (Figure 12b) also stood out by producing water with relatively high TDS concentrations of 2,150 and 2,190 mg/L and sulfate concentrations of 1,330 and 1,380 mg/L (relative sulfate concentrations of 0.87 and 0.91) for samples collected in the fall of 2018 and the spring of 2019 respectively. Water from AR-0019 does not stand out isotopically, plotting along the observed evaporation trends. AR-0019 water is characterized as a calcium-sulfate water type and plots at the top of the diamond portion of the Piper diagram (Figure 19). While the well AR-0187 is not necessarily considered to represent a mixing endmember, this well stood out as the only well north of Aztec that produced high-sulfate water. Water from AR-0187, located near Cedar Hill (Figure 12a), is characterized as sodium-sulfate water and exhibited the highest TDS and sulfate concentrations of 2,900 mg/L and 1,630 mg/L (approximate relative sulfate concentration of 0.75) respectively.

A three-endmember mixing relationship is seen when sodium/chloride molar ratios are plotted as a function of relative sulfate concentrations (Figure 42). The two high-sulfate endmembers are differentiated by the sodium/chloride ratios, with water from AR-0213 having the highest sodium/chloride ratio. Water from AR-0217appears to be mostly a mixture between the freshwater endmember and AR-0213. Figure 43 shows modeled mixing lines between three endmembers that are defined by δD and the sodium/chloride molar ratio. The fresh water (river or irrigation water) endmember has a δD value of about -106 ‰ and the lowest sodium/chloride ratio. The sodium-sulfate high-TDS water (AR-0213) is characterized by a very light isotopic composition and the highest sodium/chloride ratio. AR-0019 exhibits an intermediate isotopic composition and sodium/chloride ratio. The size of the data points on Figure 43 are proportional to the relative sulfate concentration (as a proportion of total anions in meq/L). A water sample that is purely a mixture of two of the endmembers will plot on the appropriate mixing line. Evaporation results in an increase in the δD value but does not affect the Na/Cl ratio. Therefore, the combination of mixing and evaporation will result in the data point plotting between the two endmembers but above the mixing line. We can see then that the combination of evaporation and mixing of the fresh water and the calcium-sulfate water (AR-0019) can explain almost all the data. However, the relative sulfate concentrations suggest that many of the water samples that plot between the fresh water endmember and AR-0019 exhibit relative sulfate concentrations that are too small for that mixing ratio. Therefore it is likely that some of that sulfate is derived from mixing with water similar in composition to AR-0213. With the exception of AR-0217, water samples with the highest δD values (AR-0031, AR-0187 and others), plot at the far end of the evaporation lines in Figure 32 and show significantly higher relative sulfate concentrations. This relationship indicates that evaporation can also increase the relative sulfate concentration. Therefore, the observed increase in sulfate concentrations along the groundwater flow path is a result of mixing and evaporation. Figure 44, which shows δD plotted as a function of relative sulfate concentration, shows the same mixing relationships as shown in Figure 43 and similarly, shows that evaporation does indeed increase the relative sulfate concentration.

In contrast from the mixing relationships seen in Figure 42, Figure 43 and Figure 44 indicate that water from AR-0217 is not an endmember or a result of these mixing and evaporative processes. The difference between these mixing relationships shown in Figure 42 and those shown in Figure 43 and Figure 44 is related to constituents being used to define endmembers. In Figure 42, both the sodium/chloride molar ratio and the relative sulfate concentration are related to the solute source, while the stable isotopic composition of water (δD), used to define mixing relationships in Figure 43 and Figure 44 is related to the water source (the precipitation in the recharge area during the time of recharge). In other words,

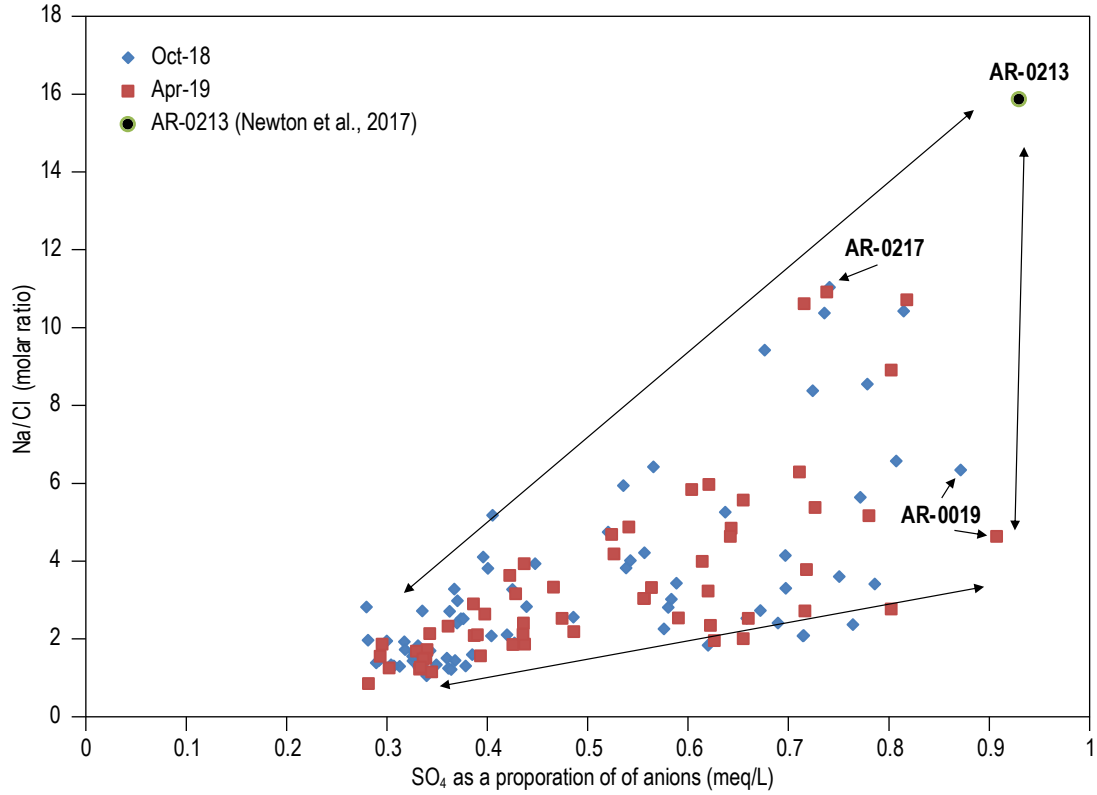

Figure 42. Sodium/chloride ratio as a function of the relative sulfate concentration. Double-ended arrows indicate mixing between two endmembers.

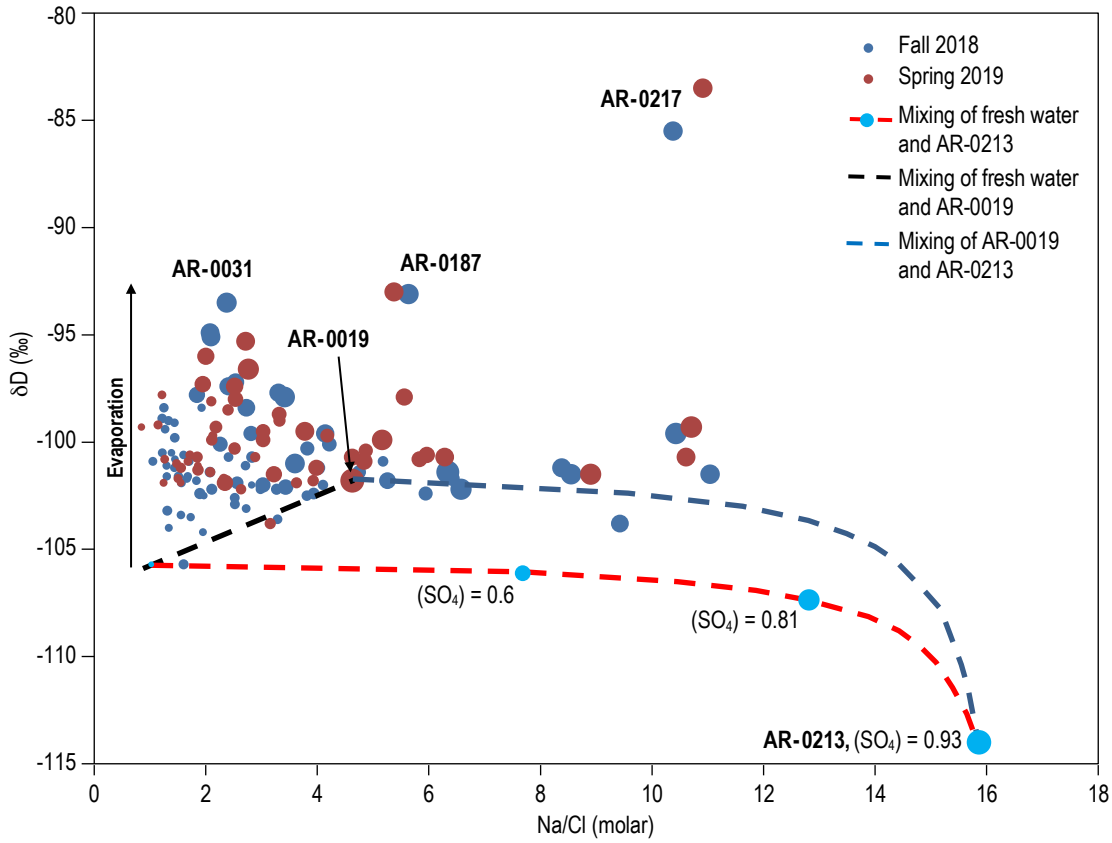

Figure 43. Mixing models for three different endmembers shown with respect to δD and the Na/Cl molar ratio. The symbol size is proportional to the relative sulfate concentration.

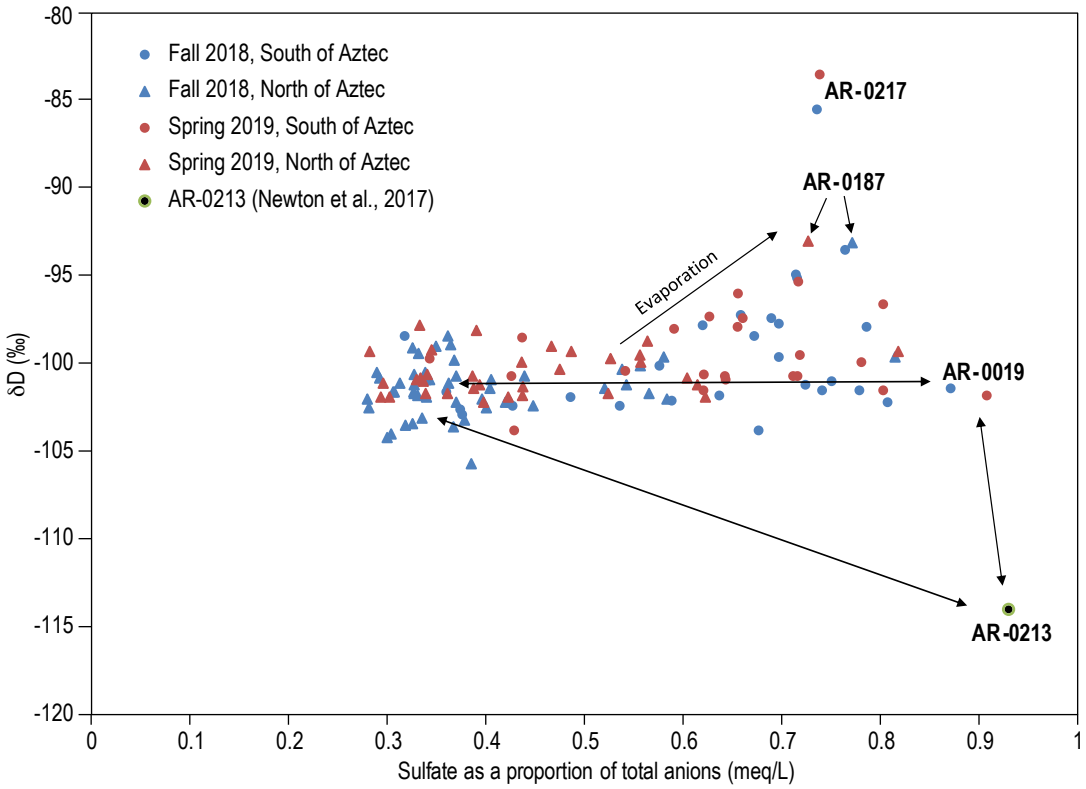

Figure 44. δD plotted as a function of relative sulfate concentration. The double-ended arrows denote mixing between two endmembers.

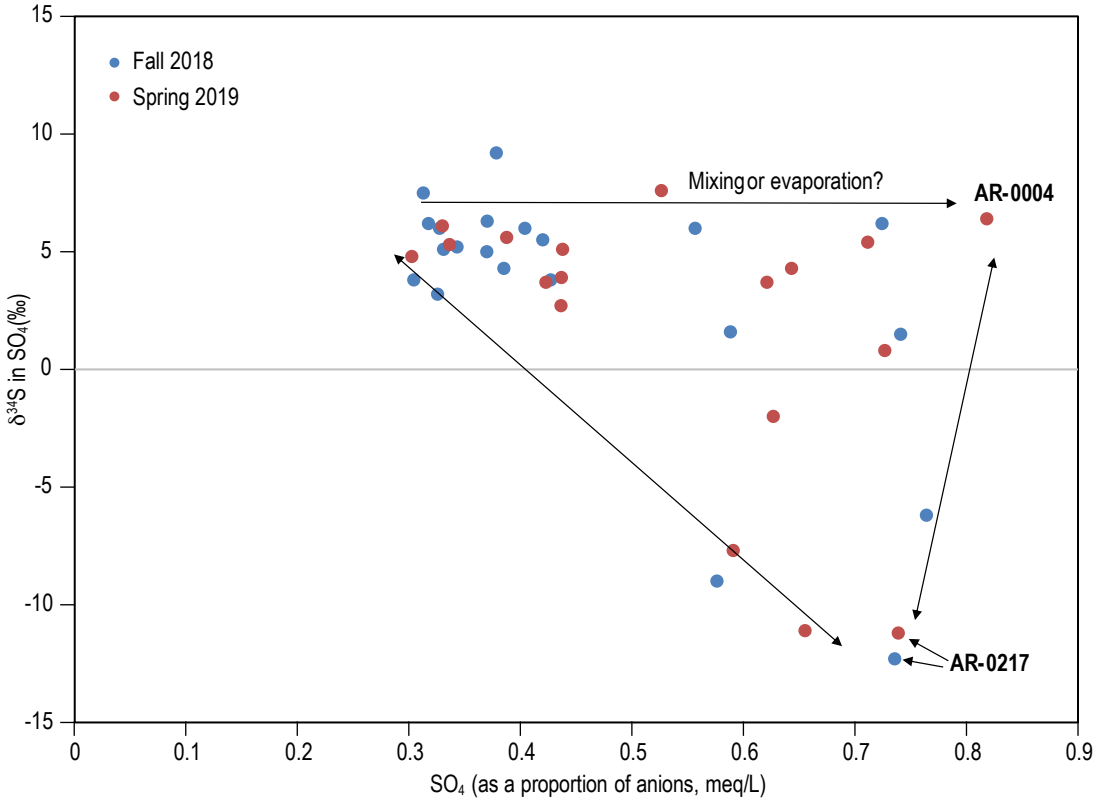

Figure 45. $\delta^{34}S$ (sulfate) plotted as a function of relative sulfate concentrations. Double-ended arrows denote mixing of two different endmembers.

it appears that while there may be different water sources traveling along different flow paths adding sulfate to the shallow aquifer (or not, in the case of AR-0217), the sulfate is coming from the same geologic source, which appears to be Paleogene rocks that lie beneath the alluvium. It is also possible that there is more than one sulfate source that is contributing to dissolved constituents in the shallow alluvial aquifer. These mixing relationships are examined in more detail below with the stable isotopes of sulfate and DIC with implications for solute source determination.

Identification of solute sources

From the discussion above, it is clear that the observed change in groundwater chemistry within the shallow aquifer is primarily due to evaporation and mixing. Groundwater at the New Mexico/Colorado border is characterized as calcium-bicarbonate water type with TDS concentrations between 500 and 800 milligrams per liter. TDS and sulfate concentrations increase down-gradient (towards the southwest) along groundwater flow paths and is particularly pronounced in wells south of Aztec with TDS and sulfate concentrations as high as 2,740 and 1,590 milligrams per liter respectively. In this section we examine major ion chemistry and isotopic compositions of sulfate and DIC to determine the geologic solute sources for 1) groundwater at the northern extent of the of the study area (NM state line), which is referred to as the fresh-water endmember and 2) the groundwater source(s) entering the shallow system and increasing TDS and sulfate concentrations along groundwater flow paths, referred to as the high-sulfate endmember(s). The following discussion is largely considered under the framework of the conceptual model presented by Newton et al., (2017) (Figure 9), where the high-sulfate endmember is moving into the shallow system from a deeper aquifer system. The stable isotopic compositions of sulfate and DIC can help to more accurately identify which aquifer that may be.

Stable isotopic compositions of sulfate—The spatial distribution of $\delta^{34}S$ (sulfate) (Figure 34) and $\delta^{18}O$ (sulfate) (Figure 35), where isotopic compositions decrease in the down-gradient direction, suggests that sources of sulfate in the fresh-water endmember and the high-sulfate endmember(s) have different and distinct isotopic signatures. However, as in seen in Figure 47, while water from AR-0217 does exhibit a $\delta^{34}S$ value that is much lighter than those for water with lower relative sulfate concentrations, there are several wells that produce water with high relative sulfate concentrations (>0.5) and heavier $\delta^{34}S$ values. As discussed above, evaporation does cause the relative sulfate concentration to increase, likely due to a decrease in alkalinity caused by the resulting calcite precipitation. It appears that evaporation can cause the relative sulfate concentration to increase significantly if we assume that the observed increased δD values in Figure 44 is primarily due to evaporation. Therefore, the increase in relative sulfate concentrations for waters with heavier sulfate isotopic compositions may be primarily due to evaporation. An alternative explanation would be the mixing with a high-sulfate water with a sulfate isotopic composition similar to that of the fresh water endmember, which may be represented by AR-0004. This well, which is located just north of Aztec (Figure 12b), does exhibit high TDS and sulfate concentrations (2,100 and 1,230 mg/L respectively) but did not really stand out as a possible mixing endmember. Unfortunately, we do not know the sulfate isotopic composition for water from AR-0213 or AR-0019. These data would likely help to determine the processes that result in high relative sulfate concentrations and heavy isotopic compositions.

Sulfur and oxygen isotope data for dissolved sulfate were compared to values measured by Nordstrom et al., (2007) for streams, springs, mines, and minerals in the Upper Animas River Basin above Silverton, Colorado (Figure 48). Isotope values in all shallow groundwater samples collected for this study north of Aztec and some samples collected south of Aztec look similar to those for springs and streams in the Upper Animas watershed with a slight shift in $\delta^{18}O$ towards heavier values. The four labeled points for samples collected south of Aztec plot with lighter isotopic values along an apparent mixing line, with AR-0217 as the endmember. While we are uncertain of the cause for the apparent small shift in $\delta^{18}O$ values relative to those for springs in the Upper Animas watershed, the sulfate isotopic compositions of groundwater north of Aztec suggests that the sulfate source for the fresh water endmember is likely pyrite and other sulfides, and hypogenic gypsum and anhydrite in the Animas River headwaters in the San Juan Mountains.

Sulfate stable isotope data indicates that the sulfate source for the high-sulfate mixing endmember (AR-0217) is characterized by a distinct isotopic signature that is significantly lighter (for both $\delta^{34}S$ and $\delta^{18}O$) than that observed for the fresh water endmember. The stable isotopic composition of sulfur in sulfate reflects the $\delta^{34}S$ of the evaporites and sulfide

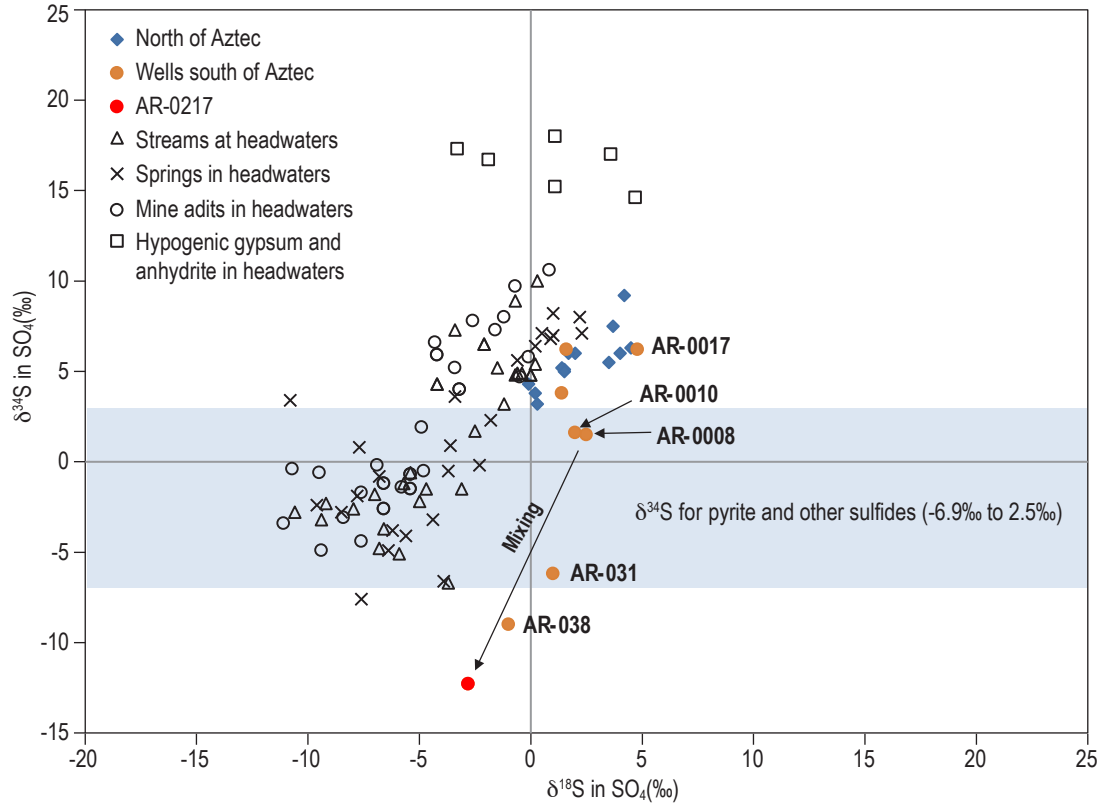

Figure 46. $\delta^{34}S$ (sulfate) as a function of $\delta^{18}O$ (sulfate) for groundwater samples along with values for streams, springs, mine adits, and rocks in the Upper Animas watershed by Nordstrom et al., (2007).

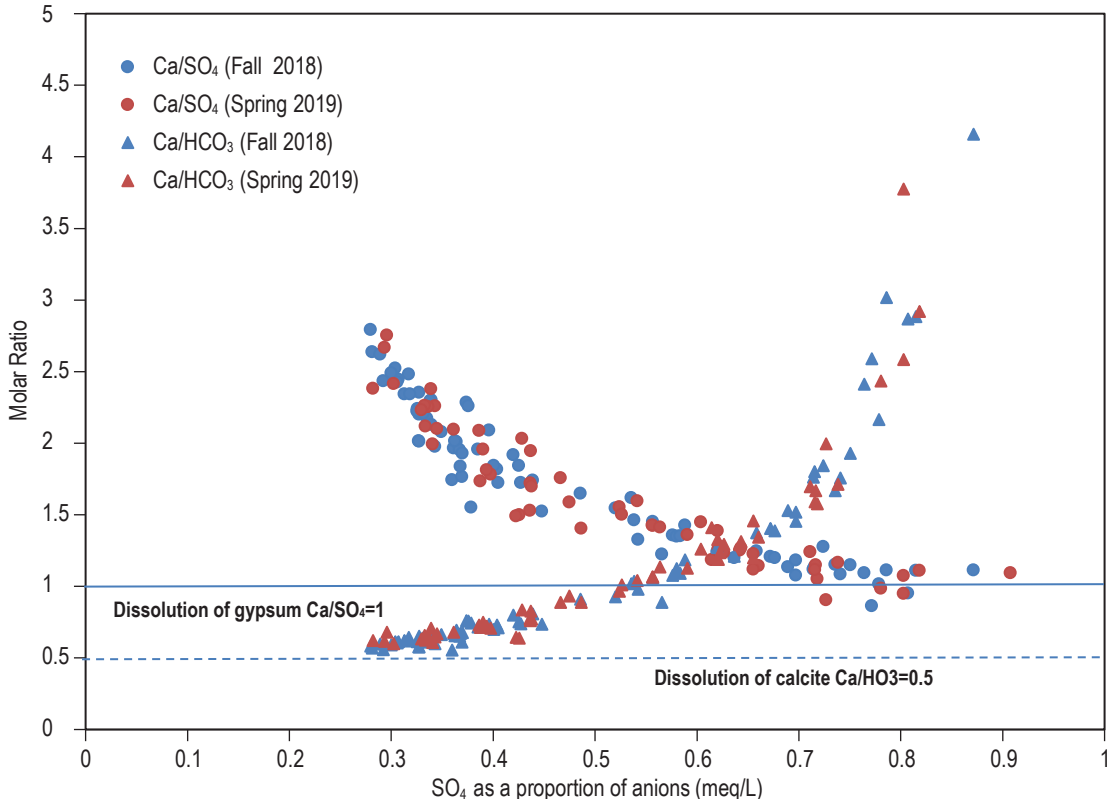

Figure 47. Molar ratios (Ca/SO_4 and Ca/HCO_3) as a function of relative sulfate concentrations. Calcium concentrations were corrected to represent values before subsequent cation exchange reactions.

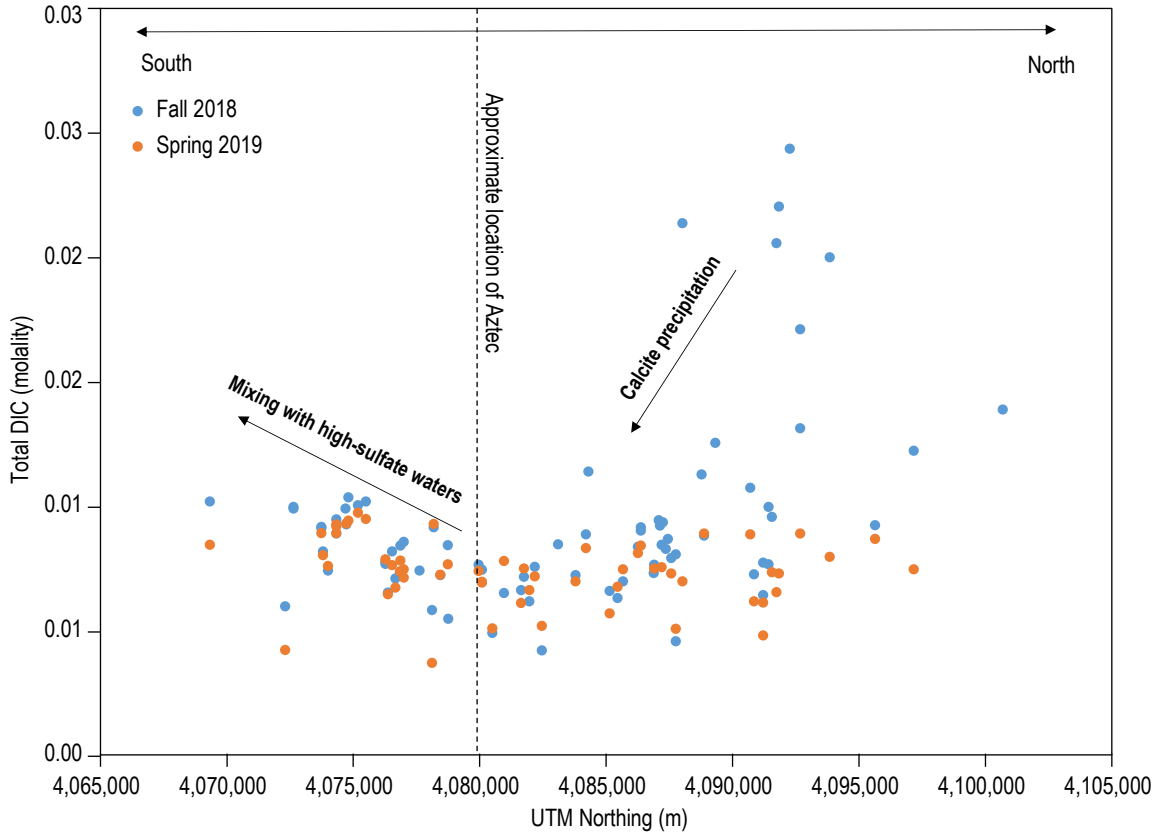

Figure 48. Modeled total DIC plotted as a function of UTM Northing coordinates.

minerals that underwent dissolution/oxidation along the flow path (Szynkiewicz et al, 2012). The range of observed values for $\delta^{34}S$ and $\delta^{18}O$ in dissolved sulfate for different types of rocks (Seal, 2006; Vitoria et al., 2004) can be used to identify the sulfate sources. However, before we determine the solute source based on the isotopic composition of sulfate in water from AR-0217, we will examine stoichiometric relationships in an effort to identify the mineral from which sulfur is derived. Figure 47 shows calcium/sulfate and calcium/bicarbonate ratios as a function of relative sulfate concentrations. Calcium concentrations used to calculate these ratios were corrected for cation exchange, using the sodium excess values and the observed calcium/magnesium ratios. The relative sulfate concentrations indicates the degree of mixing along the flow path. As sulfate becomes the dominant anion which is observed to occur along the general flow path to the southwest, calcium/sulfate ratios transition from 0.5 (indicative of the dissolution of calcite) to a ratio of one, indicating that gypsum is very likely the source of sulfate in regional groundwater that mixes with shallow groundwater, significantly impacting groundwater quality. The possible high-sulfate endmember, AR-0019 is characterized as a calcium-sulfate water type, which is indicative of gypsum dissolution.

Water from AR-0213 is chemically similar to water from the Nacimiento Formation in the San Juan Basin, south of the San Juan River, described by Phillips et al., (1986, 1989), including the anomalously light isotopic composition and old carbon-14 age. This water was characterized by high pH, alkalinity, sulfate, and sodium, and extremely low calcium and magnesium concentrations. While they considered that the sulfate source may be the oxidation of sulfide minerals, they concluded that it was much more likely that dissolution of gypsum and cation exchange were the important geochemical processes that affected the water chemistry, providing more evidence that gypsum is likely the source of sulfate that is being added to the shallow aquifer system particularly in the southern portion of the study area (south of Aztec).

Gypsum is a very common mineral that exists in evaporites from the evaporation of lakes and sea water, and it is also commonly deposited in veins in hydrothermal systems. The stable isotopic composition of sulfate in gypsum is usually much heavier than that observed for AR-0217. Hypogenic gypsum found in the Upper Animas water shed exhibits $\delta^{34}S$ values between fifteen and twenty per mil (Figure 46), and in general, gypsum in marine evaporites exhibit

$\delta^{34}S$ values between 10 and 35‰. Vitoria et al., 2004 shows the range of $\delta^{34}S$ values for terrestrial evaporates to be between -13 and 10 per mil, but it is very rare to find these more negative values for gypsum in the literature.

Sulfide minerals that are derived from biogenic reduction of sulfates can exhibit extremely light isotopic compositions due to kinetic isotopic fractionation associated with this process (Seal, 2006). Another source that should be considered is fluids associated with coal, oil, and gas, which often contain sulfides with very light isotopic compositions (Seal, 2006). Chafin (1994) found methane at concentrations that exceeded the reporting limit of 0.005 mg/L in 70 of 205 groundwater samples in the Animas River Valley in Colorado and New Mexico. Potential sources of dissolved methane included some biogenic gas from the Animas and Nacimiento Formations but mostly thermogenic gas from deep reservoirs such as the Dakota Sandstone and the Mesaverde Group. The upper Fruitland Formation and Kirtland Shale could also account for some of this observed methane in groundwater. Oxidation of these isotopically light sulfides would result in sulfate with similar light isotopic values, as this process produces negligible sulfur isotope fractionation.

Another complication is the lack of evidence of the occurrence of evaporites in the underlying rocks. Evaporites usually occur as discrete beds of varying thickness; we have not seen the mention of evaporites in the geologic descriptions for the Paleogene rocks and for most of the underlying Cretaceous rocks (Craigg, 2001). The one exception is Todilto Formation, which is over 2,000 meters below surface in the northern portion of the San Juan Basin (Figure 2) and contains a gypsum member. However, the gypsum member of the Todilto Formation is not observed in this area of the San Juan Basin. Also gypsum from the Todilto Formation exhibits $\delta^{34}S$ values ranging from fifteen to seventeen per mil (Kirkland et al., 1995) and is therefore not the source of sulfate in water from AR-0217. While we cannot definitively identify the source of gypsum that contributes sulfate to the high-sulfate endmember(s), we think gypsum distributed diffusively and in localized areas in Neogene rocks, such as the Nacimiento Formation is likely the sulfate source in question.

Stable isotopic compositions of DIC—Stable carbon isotopes in DIC are useful for tracing weathering reactions along a flow path and have also been used to confirm the presence of organic contaminants in a groundwater system (Bullen and Kendall, 1998). For a system where a strong acid, such as sulfuric acid, dissolves carbonate rock, the $\delta^{13}C$ value will be that of the carbonate rock. For a system where carbonic acid, derived from the dissolution of soil CO_2, dissolves carbonate rock, this value ($\delta^{13}C$) usually represents an intermediate value between the $\delta^{13}C$ value of the dissolved carbonate and that of soil CO_2. Marine carbonates usually exhibit $\delta^{13}C$ values of 0 ± 5‰, while terrestrial and hydrothermal carbonates can have much different values. The stable carbon isotopic composition of soil CO_2 depends on the vegetation type. For C3 plants, which include pine and deciduous trees, soil CO_2 exhibits $\delta^{13}C$ values ranging from -20‰ to -37‰. For C4 plants, such as corn, soil CO_2 shows $\delta^{13}C$ values ranging from -10 to -20‰.

Sulfate isotope data discussed above indicate that solute sources for the fresh water mixing endmember are rocks in the Upper Animas watershed. Propylitically altered rock, which underlies 90% of the Upper Animas watershed (Mast et al., 2007), contains a significant amount of calcite and is likely the source of measurable alkalinity in the Upper Animas River. While the $\delta^{13}C$ values for carbonate minerals and soil CO_2 in the Upper Animas watershed are not known, we can estimate these values based on these carbon isotope data and some assumptions. The inverse correlation between $\delta^{13}C$ (DIC) and bicarbonate concentrations seen in Figure 38 is probably mainly due to isotopic fractionation due to calcite precipitation, which is likely occurring based on calculated saturation indices with respect to calcite. The precipitation of calcite results in the enrichment of $\delta^{13}C$ in the solid carbonate phase and the depletion of $\delta^{13}C$ for DIC (Turner, 1982). Calculated total DIC concentrations (modeled in PHREEQC) show a rough spatial trend (Figure 48). The decrease in total DIC concentration from north to south (seen north of Aztec) is due to continuous calcite precipitation along the groundwater flow path. Therefore we will assume that the groundwater sample with heaviest isotopic composition for DIC represents that of groundwater in the Upper Animas watershed. Assuming $\delta^{13}C$ = 0‰ for the carbonate rocks in the Upper Animas watershed, the heaviest observed $\delta^{13}C$ value for DIC in groundwater of -9.8 ‰ would result in a $\delta^{13}C$ value for soil CO_2 of about -20‰, which is on the heavy end but still within the range for C3 plants.

While calcite precipitation appears to be the main control on DIC concentrations and $\delta^{13}C$ (DIC) north of Aztec, a slight increase in DIC south of Aztec (Figure 48) is due to mixing with the high-sulfate groundwaters, which is also observed in Figure 49, which shows $\delta^{34}S$ (sulfate) plotted against $\delta^{13}C$ (DIC). The lightest sulfate and DIC isotopic composition

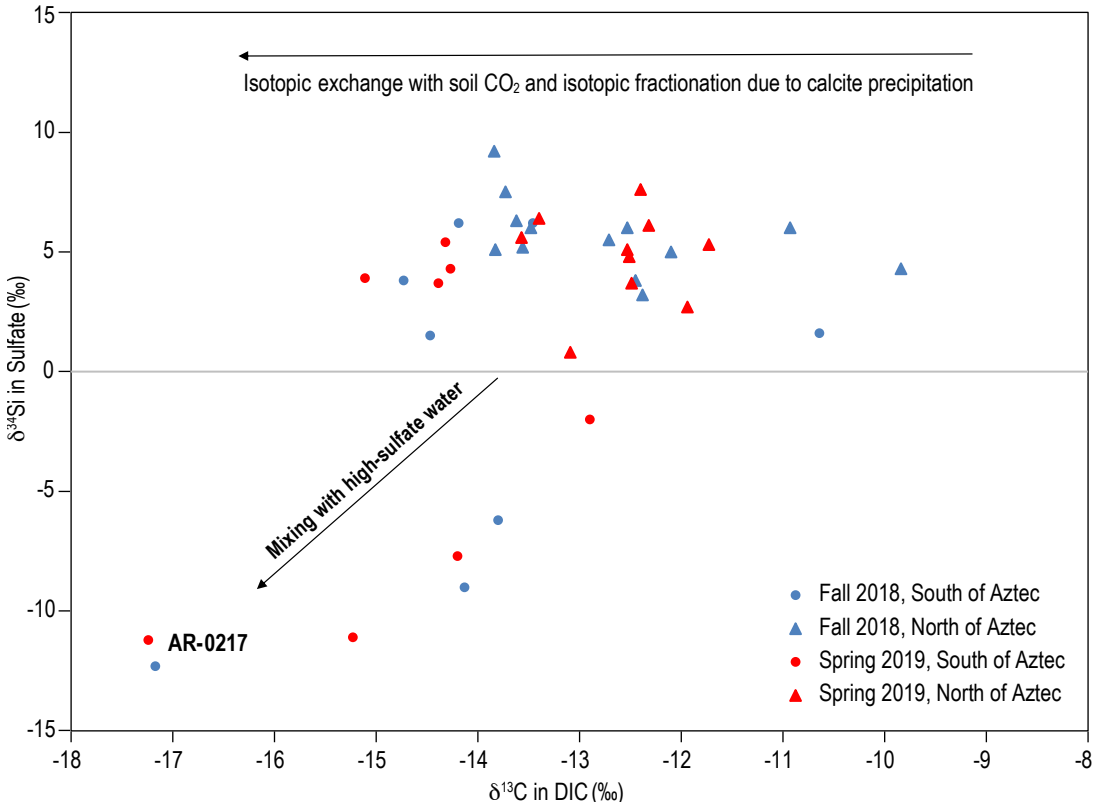

Figure 49. $\delta^{34}S$ (sulfate) as a function of $\delta^{13}C$ (DIC).

was observed in AR-0217, which appears to represent the high-sulfate mixing endmember. Assuming the high-sulfate endmember comes from depth, the $\delta^{13}C$ (DIC) value is likely representative of that for the solute source rock, and the measured $\delta^{13}C$ (DIC) values for AR-0217 do fall within the range that has been observed for freshwater or terrestrial carbonates (Vitoria et al., 2004). As was discussed above, fluids associated with oil, gas, and coal can also explain the light carbon isotopic composition for DIC (Chafin, 2004).

Summary of solute source determination —Geochemical data presented above, including general water chemistry, and stable isotope data for water (δD and $\delta^{18}O$), dissolved sulfate ($\delta^{34}S$ and $\delta^{18}O$), and DIC ($\delta^{13}C$) indicates that there are two main sources of dissolved constituents:

1) Propylitized bedrock and hydrothermal minerals in the Animas River headwaters
2) Gypsum from underlying strata

The sulfate isotope data presented in Figure 46 strongly suggests that the solute source for the fresh water endmember is propylitized bedrock and hydrothermal minerals in the Upper Animas watershed in Colorado. The interpretation of general chemistry data and sulfate and DIC isotope data for the identification of the solute source for the high-sulfate endmember is more complicated. Simple stoichiometric analysis strongly indicates that the solute source is the mineral gypsum, although significant amounts of gypsum are not observed in underlying strata. While more work needs to be done to identify where this gypsum is located, it is most likely that the high-sulfate water source(s) come from the underlying Nacimiento Formation and are upwelled into the shallow system as described by the conceptual model shown in Figure 9.

Hydrologic and geochemical processes associated with the upwelling of high-sulfate water

Water from several wells [AR-0213 (Newton et al., 2017), AR-0217, AR-0187, AR-0019] show high-sulfate concentrations that appear to be associated with a deep sulfate input that is especially apparent south of Aztec. However, other geochemical data, such as water type and the stable isotopic composition of the water, exhibit differences, suggesting a more complex system. These differences are likely due to variations in water sources (e.g., precipitation from different regions or elevations), flow path lengths or residence time, and spatial variances in lithology. For example, AR-0213, which exhibited the highest sulfate and

TDS concentrations (TDS 10,000 mg/L), has a stable isotopic composition that indicates the water source is high elevation precipitation that travels along a very deep regional flow path with a residence time of tens of thousands of years. Along this regional flow path, water-mineral interactions such as dissolution and cation exchange over this long time period results in the observed very brackish sodium-sulfate water. The well AR-0019 is located close to the edge of the valley and is approximately 68 feet deep, which is deeper than many alluvial wells in the study area. For the well AR-0019, the isotopic composition suggests it is river water (evaporation signature) that has traveled along an intermediate flow path, resulting in a slightly brackish (TDS = 2,150 mg/L) calcium-bicarbonate water. This water is likely not nearly as old as water from AR-0213, as a much smaller degree of cation exchange has taken place. The isotopic composition of AR-0217 suggests this is modern water, a mixture of local summer and winter precipitation which flows along a flow path that does not significantly interact with the shallow aquifer.

Water that appears to be most affected by the input of deep sulfate occurs south of Aztec and the mechanism by which the deep high-sulfate water discharges into the shallow system is consistent with the conceptual model presented in Figure 9. However this water may interact with the shallow system in different ways as suggested by data for AR-0187, which is located in the northern part of the study area near Cedar Hill where there is a large bend in the river. Water from AR-0187 shows evidence of mixing with high-sulfate water and a high degree of evaporation (Figure 34). It is seen in Figure 50 that AR-0187 is located close to the edge of the valley, next to steep Paleogene age cliffs. Interestingly, AR-0238, which is also located near this cliff not too far from AR-0187, shows very different water chemistry, more in line with the freshwater endmember. An irrigation ditch is located between AR-0238 and the cliff, which is likely supplying irrigation water to the alluvial aquifer, whereas the well AR-0187 is located between the cliff and an irrigation ditch. Whether regional high-sulfate groundwater is being upwelled along a fault or it is discharging from the adjacent cliff is unknown.

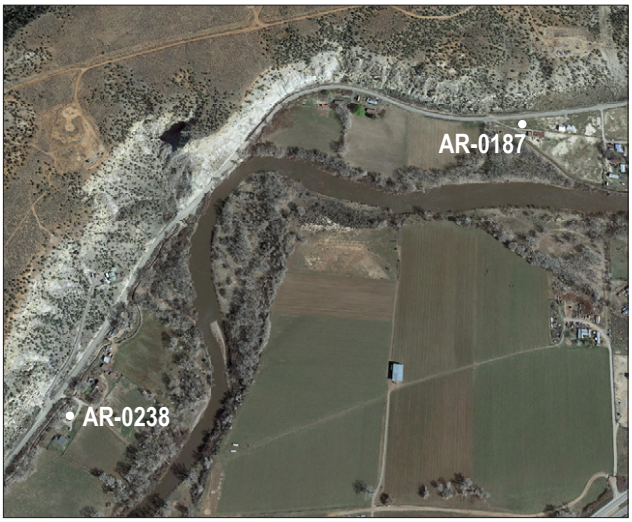

Figure 50. Google Earth image of well locations for AR-0187 and AR-0238.

The transition from calcium-bicarbonate water to a calcium-sulfate water with the calcium/sulfate ratio approaching unity (Figure 47) is likely due to the precipitation of calcite, driven by the common ion effect due to the mixing of the freshwater endmember with the high-sulfate water endmember(s). Evidence of the precipitation of calcite includes the inverse relationship between pH and alkalinity (Figure 21), the inverse correlation between $\delta^{13}C$ (DIC) and bicarbonate concentrations (due to isotopic fractionation associated with calcite precipitation, Figure 38), and the observed decrease in total DIC concentrations in the down-gradient direction (Figure 48). Figure 51 shows that with the exception of some water samples with lower relative sulfate concentrations, almost all water samples were saturated with respect to calcite, while almost all water samples were under saturated with respect to gypsum with the saturation index increasing with increasing sulfate concentrations. The observed relationship between the saturation indices for gypsum and calcite and relative sulfate concentrations seen in Figure 51 provides more evidence for this geochemical process. Jin et al., (2012) observed this process occurring in a small third-order stream in Wyoming. The discharge of small amounts of groundwater with high calcium and sulfate concentrations from the dissolution of gypsum, caused calcite precipitation in the stream due to the common ion effect. This process is likely occurring in the shallow groundwater system in the Animas Valley.

Assessment of redox conditions and manganese and iron sources

Based on the discussion above, major ion chemistry in the shallow aquifer in the Animas Valley in New Mexico is controlled by mixing of at least two endmembers and evaporation. The two major solute sources are propylitized bedrock and hydrothermal minerals in the Animas River headwaters and gypsum from underlying strata in the New Mexico reach of the Animas Valley. The mixing process results

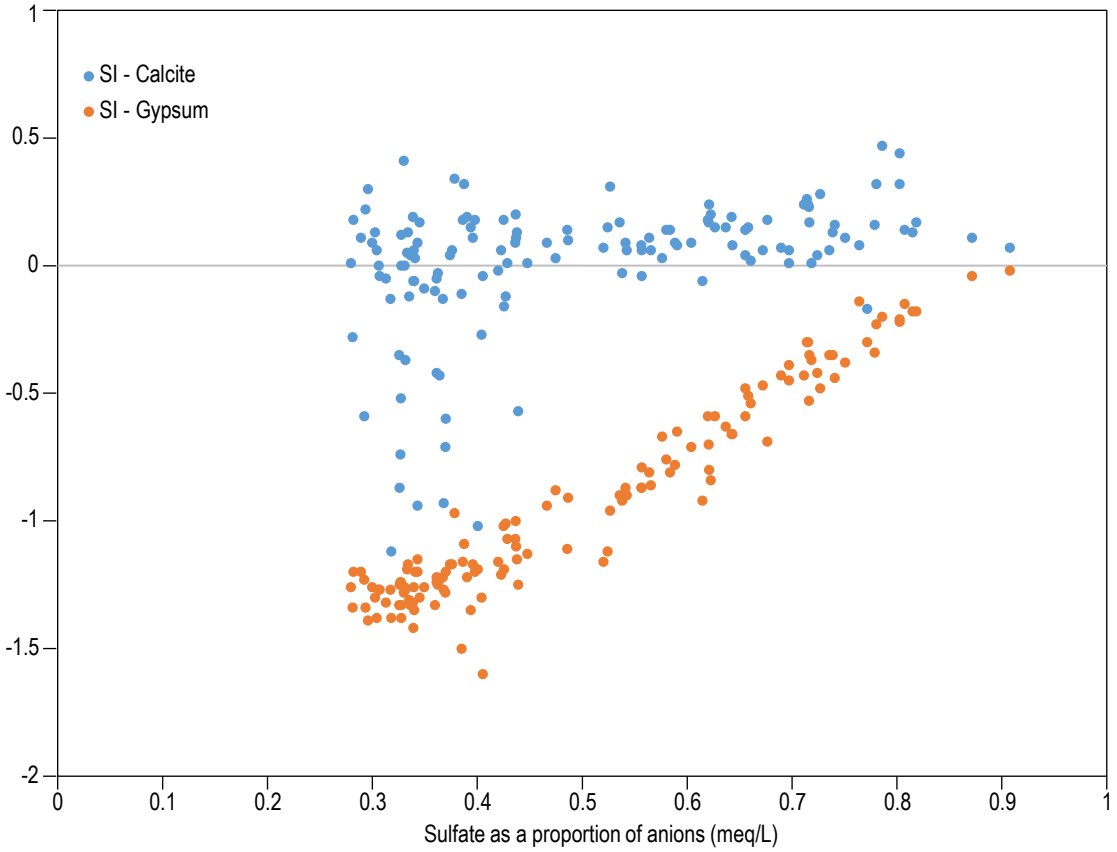

Figure 51. Saturation indices (Si) for calcite and gypsum as a function of sulfate concentration.

in a spatial trend where concentrations for several dissolved constituents, including TDS and sulfate, increase in the down-gradient direction (Figure 18) with concentrations being significantly greater to the south of Aztec. Newton et al., (2017) showed that besides TDS and sulfate, other constituents, such as strontium and barium, also increase in concentration in the down-gradient direction. This trend was not observed for other analytes, such as chloride, manganese, and iron (Figure 25 and Figure 26). Minor solutes such as these that are not controlled by the mixing processes described above, are likely controlled by more localized processes. Therefore, the sources of iron and manganese in the shallow aquifer are likely of local origin, deposited as alluvial sediments that make up the aquifer.

The measured Eh values and the presence of dissolved manganese in most wells indicates that dissolved oxygen is consumed quickly, resulting in manganese oxides and iron hydroxides being the main redox buffers. The Eh data presented above shows that redox processes are quite dynamic and respond to the different hydrologic regimes related to irrigation. In fall 2018, groundwater in the northern part of the study area showed lower pH and higher Eh values (Figure 29, Figure 30) due to the input of oxygenated river water via irrigation. These low pH and high Eh values were not observed in the spring of 2019. Figure 30 shows that higher dissolved iron and manganese concentrations are associated with lower Eh values. The fall 2018/spring 2019 ratio for Eh values, and manganese and iron concentrations were examined for wells that were sampled both in 2018 and 2019 (Figure 31). Ratios less than 1 indicate higher values in spring 2019 and ratios greater than 1 indicate higher values in the fall of 2018. In general manganese and iron concentrations were higher in spring 2019 and Eh values were higher in the fall of 2018. This inverse relationship between Eh values and iron and manganese concentrations is reflective of the effects of the input of irrigation water during irrigation season and its absence in winter and early spring months on redox conditions in the shallow aquifer. During the irrigation season, oxygenated water that recharges the shallow aquifer drives down the Eh, which results in iron and manganese in some areas to precipitate, causing dissolved concentrations to decrease. After irrigation ends, dissolved oxygen is quickly consumed by the degradation of organic matter, causing Eh values to drop and iron and manganese concentrations to increase.

Identification of areas of potential groundwater contamination

Newton et al., (2017) classified the sampled wells based on the measured dissolved oxygen (DO) concentrations and how those values changed seasonally. It was suggested that areas where DO concentrations remained below 3 mg/L likely received little recharge from irrigation water. Areas where DO remained greater than 3 mg/L or fluctuated over a range of DO values that sometimes exceeded 3 mg/L are likely areas where active recharge occurs during irrigation season.

Newton et al., (2017) categorized water produced by different wells based on repeated DO measurements, as many of the wells shown in Figure 7 were sampled as many as seven times over 18 months. Figure 52 shows the range of DO values (the difference between the two measurements for this study) as a function of the maximum value for wells that were sampled in both 2018 and 2019. Data points that plot near the 1:1 line indicates that the observed fluctuation in DO concentrations ranged from near zero to the observed maximum value. Newton et al., (2017) demonstrated for many wells that showed this type of DO fluctuation with time, where the concentration would decrease to almost zero and then increase significantly, that there was an inverse relationship between the seasonal change in dissolved oxygen and TDS concentrations. The dissolved oxygen would increase and the TDS would decrease due to the input of fresher (lower TDS), well oxygenated irrigation or river water. This trend was not was not as obvious for wells sampled for this study (data not shown). This is likely due to there only being two measurements for each well. While we hoped to capture the full DO fluctuation range by sampling at the end of irrigation season in 2018 and just before irrigation began in 2019, it appears that the timing of these changes in DO concentrations are affected by other factors in addition to the irrigation cycle. These factors may include the finer scale timing of irrigation releases in specific fields, vegetation type and density in different agricultural fields at different times, and antecedent soil moisture conditions.

Nevertheless we did observe significant fluctuations in DO concentrations as seen in Figure 52. Figure 53 shows well locations with the symbol size proportional to the DO range/DO maximum value (DO_{range}/DO_{max}) ratio. This ratio relates to the dynamics of the system with respect to DO fluctuations.

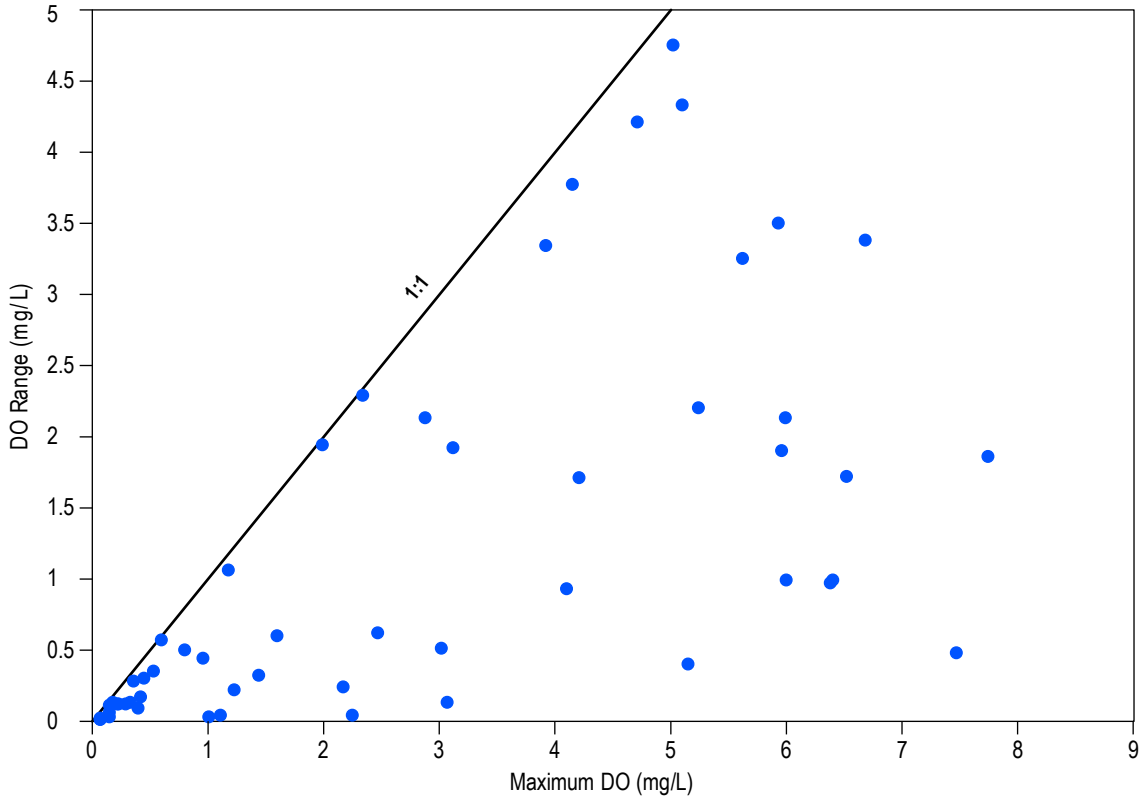

Figure 52. The range of dissolved oxygen (DO) data for each well that was measured twice plotted as a function of the maximum DO concentration. Points that plot near the 1:1 line indicate that the minimum DO concentration was close to zero.

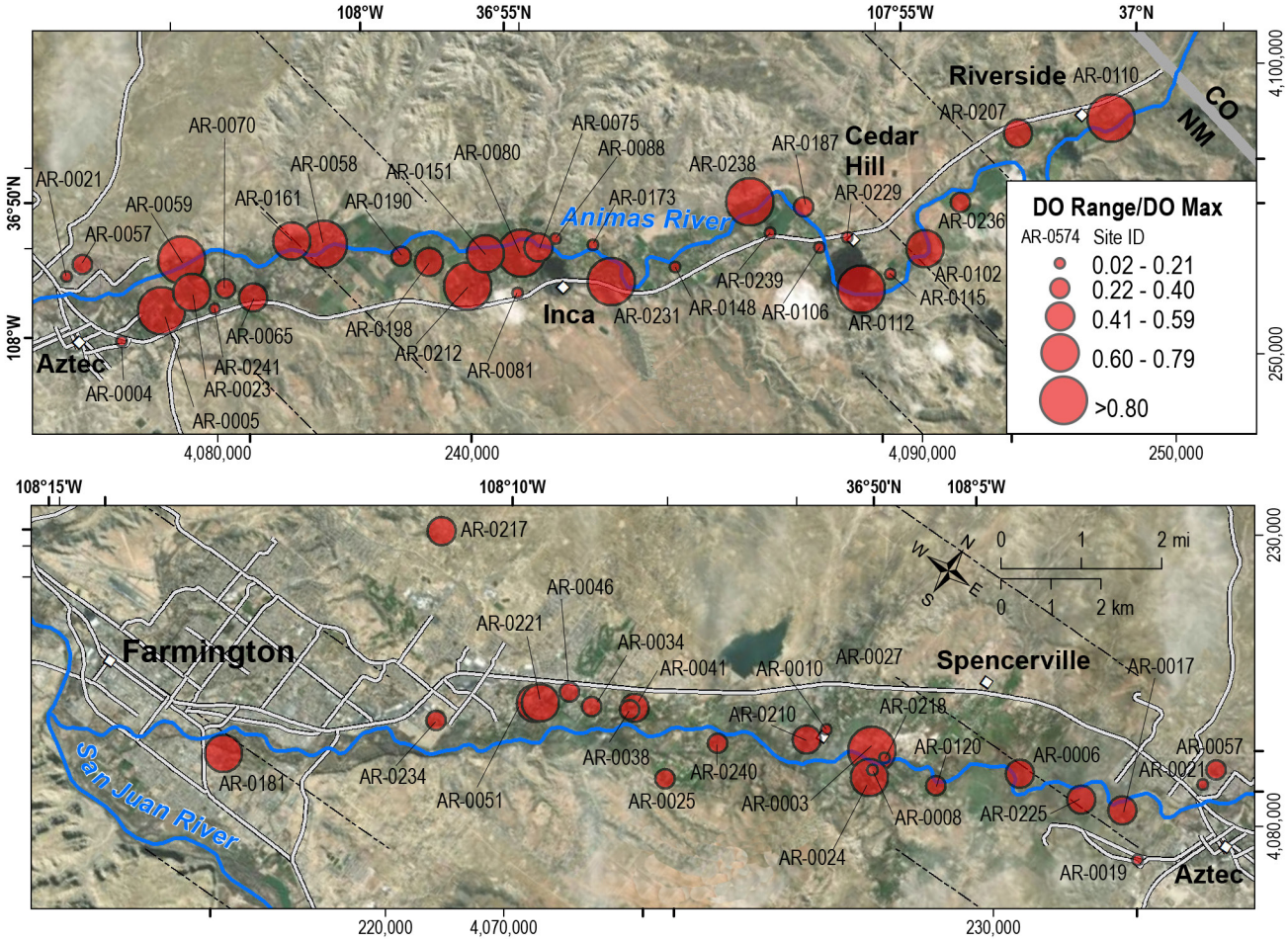

Figure 53. Map that shows ratio of the range DO measurements to the Maximum DO value for wells that were sampled in both 2018 and 2019. Larger values indicate a more dynamic system where oxygenated river or irrigation water recharges the aquifer, increasing DO, which decreases over time after irrigation season ends.

Higher ratios plot closer to the 1:1 line in Figure 52. Assuming that the observed DO fluctuation with time is due to the input of fresh oxygenated river or irrigation water at a specific time, resulting in higher DO concentrations, followed by a decrease in DO due to degradation of organic matter, a larger ratio may be indicative of an area where this process is occurring. Therefore DO_{range}/DO_{max} ratios may be used to identify areas of potential groundwater contamination due to the input of contaminated surface water. In Figure 53, most wells with a DO_{range}/DO_{max} ratios greater than 0.8 are located very close to the river or near agricultural areas. However, there are many wells with low ratios located in these same areas. Due to the limited number of samples for each well and complications discussed above, this map is likely inaccurate for the purpose of identifying areas of potential contamination, but it serves as an example of a simple method that can be used for this purpose. By monitoring wells in close proximity to the river, ditches, or agricultural fields, on a finer timescale (biweekly or monthly), areas of potential risk of contamination by the input of surface water can likely be identified. The advantage of this method is that DO can be easily measured in real time with electrode instruments that are available from many different vendors at a relatively affordable price. As a word of caution when using this method, instruments that measure dissolved oxygen are quite sensitive, and it is important to properly calibrate the instrument according to the owner's manual before taking the measurement.

VI. CONCLUSIONS

Water level data and geochemical results for this study were very similar to those of Newton et al., (2017). Water level data showed groundwater flowing to the southwest and towards the river (Figure 39 and Figure 40), resulting in the river gaining water from the aquifer over most of the entire reach in New Mexico. However there are some localized areas, particularly in the northern portion of the study area where water levels in some wells close to the river were observed to drop below river stage, indicating a reversal in the hydraulic gradient between the river and the aquifer. This observed gradient reversal appears to mostly occur during the winter and spring when water levels are observed to be their lowest. Historically low discharge rates in the Animas River in 2018 caused water levels in some wells close to the river to drop below water levels observed in past years and in 2019. However, water levels over most of the study area did not appear to be affected, mainly because groundwater levels in the Animas Valley are largely controlled by irrigation. Irrigation water recharges the shallow aquifer by infiltration through fields and irrigation canals, causing water levels to rise. Water then drains back into the river during the winter months, causing water levels to decrease.

Major ion chemistry showed similar spatial trends to those observed by Newton et al., (2017). Sulfate and TDS concentrations increase down-gradient (to the southwest). The conceptual model (Figure 9) that describes geologic controlled upwelling of high-sulfate regional groundwater was largely confirmed. However, this study highlighted some complexities. The stable isotopic compositions of sulfate and DIC suggest that the source of the sulfate being added to the system is likely terrestrial gypsum or anhydrite from underlying strata. However water chemistry data and the stable isotopic composition of water indicate that while there may be a single sulfate source, the water source and flow paths may vary significantly.

Stable isotope data for sulfate was compared to data presented by Nordstrom et al., (2007), which included stable isotopic compositions of springs, streams, and rocks in the Upper Animas watershed in Colorado. For groundwater that is chemically similar to river water, it appears that sulfate and likely most other dissolved constituents originate from volcanic rocks and alteration minerals in the Animas headwaters in the San Juan Mountains.

Many dissolved metals of concern (both natural and anthropogenic) are present in surface water in the Upper Animas River watershed, which ultimately defines groundwater chemistry in the northern part of the study area. Fortunately, geochemical conditions (pH and redox) result in the precipitation of most of these metals before entering the groundwater system in New Mexico. Again, we saw no evidence of groundwater contamination related to the Gold King Mine spill or legacy acid mine drainage in the San Juan Mountains. Dissolved manganese and iron that is observed to exceed secondary MCLs in some areas is likely due to manganese oxides and iron (hydr)oxides that were deposited as sediments that make up the shallow aquifer.

We originally intended to use DO-TDS relationships observed by Newton et al., (2017) to identify areas where the input of contaminated surface water (river and irrigation water) poses potential risk of contaminating the shallow aquifer. The observed increase in DO accompanied by the simultaneous decrease in TDS indicates the input of fresh oxygenated water from the river or irrigation system to the groundwater system. The subsequent increase in TDS and decrease in DO are due to the absence of the additional fresh water and the degradation of organic matter after the surface water is no longer recharging the aquifer in this area. This surface water input is mostly associated with irrigation water in ditches or agricultural fields, but it may occur in some areas near the river. Because we only sampled the wells two times (end of the irrigation season in 2018 and before the irrigation season in 2019), we did not observe the same DO-TDS relationships as Newton et al., (2017), who sampled many wells up to seven times over eighteen months. However, we demonstrated the concept of using multiple DO measurements in wells over time to identify these areas of concern. The DO_{range}/DO_{max} ratio can be a useful tool for assessing the TDS-DO interactions described above. Larger ratios may be indicative of an area where surface water is recharging the aquifer intermittently, mostly related to irrigation practices. By monitoring wells in close proximity to the river, ditches, or agricultural fields, on a biweekly or monthly timescale, areas of potential risk of contamination by the input of surface water can likely be identified.

NMBGMR preparing to collect a water sample from a domestic well in the Animas Valley, New Mexico.

REFERENCES

Bullen, T.D. and Kendall, C., 1998, Tracing of Weathering Reactions and Water Flowpaths: A Multi-isotope Approach, in Kendall, C. and McDonnell, J.J., ed., Isotope Tracers in Catchment Hydrology: Elsevier Science B.V., Amsterdam, pp. 611–646.

Center for Snow & Avalanche Studies (CSASW), 2018, WY 2018 Season Summary: http://www.codos.org/codosupdates/2018seasonsummary (accessed May 2020).

Craigg, S.D., 2001, Geologic framework of the San Juan structural basin of New Mexico, Colorado, Arizona, and Utah, with emphasis on Triassic through Tertiary rocks: U.S. Geological Survey Professional Paper 1420, 70 pp.

Chafin, D.T., 1994, Sources and Migration Pathways of Natural Gas in Near-Surface Ground Water Beneath the Animas River Valley, Colorado and New Mexico.

Cunningham, W.L., and Schalk, C.W., 2011, Groundwater technical proce¬dures of the U.S. Geological Survey: U.S. Geological Survey Techniques and Methods 1–A1, 151 p.

Fassett, J.E., 2010, Oil and gas resources of the San Juan Basin, New Mexico and Colorado, in Fassett, J.E., Zeigler, K.E., and Lueth, V.W., ed., Geology of the Four Corners Country: New Mexico Geological Society 61st Annual Fall Field Conference Guidebook, 246 p.

Jin, L., Siegel, D. I., Lautz, L. K., Mitchell, M. J., Dahms, D. E., and Mayer, B, 2010, Calcite precipitation driven by the common ion effect during ground-water-surface-water mixing: A potentially common process in streams with geologic settings containing gypsum: Bulletin of the Geological Society of America, 122(7-8), 1027-1038. https://doi.org/10.1130/B30011.1

Kelley, S., Engler, T., Cather, M., Pokorky, C., Yang, C., Mamer, E., Hoffman, G., Wilch, J., Johnson, P., and Zeigler, K., 2014, Hydrologic Assessment of Oil and Gas Resources in the San Juan Basin, New Mexico: New Mexico Bureau of Geology and Mineral Resources Open-file Report 566, 64 p.

Kirkland, D.W., Denison, R.E., and Evans, R., 1995, Middle Jurassic Todilto Formation of northern New Mexico and southwestern Colorado: Marine or nonmarine?: New Mexico Bureau of Geology and Mineral Resources Bullit6en 147, 40p.

Mast, M.A., Verplanck, P.L., Wright, W.G., and Bove, D.J., Characterization of Background Water Quality, in Church, S.E., von Guerard, P., and Finger, S.E., ed., Integrated Investigations of Environmental Effects of Historical Mining in the Animas River Watershed, San Juan County, Colorado: USGS Profession Paper 1651, Chapter E7, p. 351–383.

Newton, B.T., Mamer, E., and Timmons, S., 2017, Hydrogeology and Geochemistry of the Animas River Alluvial Aquifer after the Gold King Mine Spill, San Juan County, New Mexico: New Mexico Bureau of Geology and Mineral Resources Open-file Report 592, 64 p.

Nordstrom, D.K., Wright, W.G., Mast, M.A., Bove, D.J., and Rye, R.O., 2007, Aqueous – Sulfate Stable Isotopes – A Study of Mining-Affected and Undisturbed Acidic Drainage, in Church, S.E., von Guerard, P., and Finger, S.E., ed., Integrated Investigations of Environmental Effects of Historical Mining in the Animas River Watershed, San Juan County, Colorado: USGS Profession Paper 1651, Chapter E8, p. 391 – 413.

Parkhurst, D.L., 1995, User's guide to PHREEQC—A computer program for speciation, reaction-path, advective-transport, and inverse geochemical calculations: U.S. Geological Survey Water-Resources Investigations Report 95-4227, 143 p.

Phillips, F.M., Peeters, L.A., and Tansey, M.K., 1986, Paleoclimatic Inferences from an Isotopic Investigation of Groundwater in the Central San Juan Basin, New Mexico: Quaternary Research, no. 26, p.179–193.

Phillips, F.M., Tansey, M.K., and Peeters, L.A., 1989, An Isotopic Investigation of Groundwater in the Central San Juan Basin, New Mexico: Carbon 14 Dating as a Basis for Numerical Flow Modeling, Water Resources Research, v. 25, no. 10, p. 2259–2273.

Robson, S.G., Wright, W.G., Ground- Water Resources of the Florida Mesa Area, La Plata County, Colorado: U.S. Geological Survey Water-Resources Investigations Report 95–4190, 30 p.

Szynkiewicz, A., Newton, B.T., Timmons, S.S., and Borrok, D.M., 2012, The sources and budget for dissolved sulfate in a fractured carbonate aquifer, southern Sacramento Mountains, New Mexico, USA: Applied Geochemistry, v. 27, pp. 1451–1462.

Vitoria, L., Otero, N., Soler, A., and Canals, A., 2004, Fertilizer Characterization: Isotopic Data (N, S, O, C, and Sr): Environ. Sci. Technol., v. 38, pp. 3254–3262.

Pazzaglia, F.J., and Hawley, J.W., 2004, Neogene (rift flank) and Quaternary geology and geomorphology, in Mack, G. H., and Giles, K. A., eds., The Geology of New Mexico: New Mexico Geologic Society, p. 407–438.

Peery, R, and Kelsch, J., 2010, Well report for New Mexico American Water Company deep exploratory well, Clovis, New Mexico: unpublished report for New Mexico American Water Company by John Shomaker and Associates, Inc., 250 p.

Rawling, G.C., 2016, A hydrogeologic investigation of Curry and Roosevelt Counties, New Mexico: New Mexico Bureau of Geology and Mineral Resources Open-file Report 580, 54 p.

Scanlon, B.R., Healy, R.W., and Cook, P. G., 2002, Choosing appropriate techniques for quantifying groundwater recharge: Hydrogeology Journal, v. 10, p. 18–39.

Theis, C.V., 1937, Amount of ground-water recharge in the southern High Plains: Transactions American Geophysical Union, v. 18, pp. 564–568.

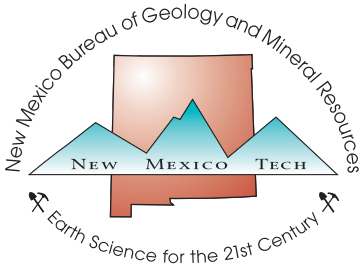

New Mexico Bureau of Geology and Mineral Resources

A Research Division of New Mexico Institute of Mining and Technology

Socorro, NM 87801
(575) 835 5490
www.geoinfo.nmt.edu